NASA TECHNICAL NOTE

NASA TN D-4193

c. 1

NASA TN D-4193

TURBULENT-BOUNDARY-LAYER CHARACTERISTICS OF POINTED SLENDER BODIES OF REVOLUTION AT SUPERSONIC SPEEDS

by Jerry M. Allen and William J. Monta

Langley Research Center
Langley Station, Hampton, Va.

NATIONAL AERONAUTICS AND SPACE ADMINISTRATION • WASHINGTON, D. C. • OCTOBER 1967

TURBULENT-BOUNDARY-LAYER CHARACTERISTICS OF POINTED SLENDER BODIES OF REVOLUTION AT SUPERSONIC SPEEDS

By Jerry M. Allen and William J. Monta

Langley Research Center
Langley Station, Hampton, Va.

NATIONAL AERONAUTICS AND SPACE ADMINISTRATION

For sale by the Clearinghouse for Federal Scientific and Technical Information
Springfield, Virginia 22151 – CFSTI price $3.00

TURBULENT-BOUNDARY-LAYER CHARACTERISTICS OF POINTED SLENDER BODIES OF REVOLUTION AT SUPERSONIC SPEEDS

By Jerry M. Allen and William J. Monta
Langley Research Center

SUMMARY

An experimental investigation has been performed at free-stream Mach numbers of 1.61 and 2.20 over a free-stream Reynolds number range from 1.2×10^6 to 27×10^6 to determine the turbulent-boundary-layer characteristics of several pointed bodies of revolution, which included two slender cones, three parabolic-arc bodies with conical noses, two parabolic-arc bodies with no boattailing, and one parabolic-arc body with boattailing. Boundary layers on these bodies were surveyed at several longitudinal stations by means of static and pitot pressure probes. Zero angle of attack was maintained throughout the tests, which were conducted under conditions of zero heat transfer.

The boundary-layer characteristics included in this study are the local and average skin-friction coefficients, the integral thicknesses, the boundary-layer total thicknesses, the shape factors, and the velocity profiles.

Predictions of flat-plate and axisymmetric flow theories are compared with the experimental data. The effects on the integral thicknesses of variations in static pressure and inviscid pitot pressure through the boundary-layer thickness are investigated and discussed.

Experimental integral thicknesses and local skin-friction coefficients showed, in general, good agreement with those calculated from axisymmetric flow theory. Shape factors were approximately equal to flat-plate flow values. A slight increase in velocity profile index with free-stream Mach number was noticed. It was found that not accounting for the variation in inviscid pitot pressure through the boundary-layer thickness resulted in errors in momentum thickness of as much as 5 percent and in displacement thickness of as much as 3.5 percent.

INTRODUCTION

The turbulent boundary layer on flat plates in compressible flow has been the subject of many experimental and theoretical investigations during the past two decades. However, much less attention has been given to the axisymmetric turbulent boundary layer, and most of this work, until recently, has been confined to the cone. Because of the relatively uncomplicated flow around a cone and the physical similarities to flat-plate flow (for example, zero pressure gradient at supersonic speeds), several simple transformations have been derived which relate the turbulent-boundary-layer characteristics on a cone to those on a flat plate (refs. 1 to 5).

Several theoretical papers (for example, refs. 6 to 9) show that the body shape in axisymmetric flow has a strong influence on boundary-layer development and that the simple transformations derived for conical flow are not applicable when the body shape differs from that of a cone. Several experiments have been performed on nonconical bodies of revolution (refs. 10 to 12). The body shapes tested, however, were of a specialized nature, having been designed to produce a desired pressure gradient or flow convergence rather than to be representative of a slender supersonic body profile.

This study was undertaken to investigate experimentally the effect of several pointed slender body shapes on the turbulent-boundary-layer characteristics in axisymmetric flow. The body shapes used in this investigation are (1) two slender cones, the data from which serve as a basis of comparison with the other experimental data and the predictions of conical theory, (2) three parabolic-arc bodies with conical noses, (3) two parabolic-arc bodies with no boattailing, and (4) one parabolic-arc body with boattailing.

The turbulent boundary layers on these models were surveyed at several longitudinal stations by means of static and pitot pressure probes. Theoretical predictions of flat-plate theory and the conical transformations of flat-plate theory are used throughout this report as a basis of comparison with the experimental data. In addition, the effects of body shape on momentum thickness and local skin friction, as predicted by modified versions of existing axisymmetric flow theories, are compared with the experimental data.

The boundary-layer characteristics included in this study are local and average skin-friction coefficients, integral thicknesses, boundary-layer total thicknesses, shape factors, and velocity profiles. The effects on the integral thicknesses of variations of static pressure and inviscid pitot pressure through the boundary-layer thickness are investigated and discussed.

SYMBOLS

a	speed of sound
c,k,m	constants
C_f	local skin-friction coefficient based on free-stream conditions, $\frac{\tau_w}{q_\infty}$

C_F	average skin-friction coefficient based on free-stream conditions, $\frac{D_F}{q_\infty S}$
C_p	static-pressure coefficient, $\frac{p - p_\infty}{q_\infty}$
D	drag
D_F	friction drag
H	ratio of displacement thickness to momentum thickness, $\frac{\delta^*}{\theta}$
l	body length
M	Mach number
n	velocity profile index, $\frac{u}{u_\delta} = \left(k\frac{y}{\delta}\right)^{1/n}$
p	static pressure
p_t	total pressure
q	dynamic pressure, $\frac{\gamma}{2}pM^2$
r	body radius
R_x	free-stream Reynolds number, $\frac{\rho_\infty u_\infty x}{\mu_\infty}$
R_θ	free-stream Reynolds number based on momentum thickness, $\frac{\rho_\infty u_\infty \theta}{\mu_\infty}$
S	surface wetted area
T	absolute static temperature
T_t	absolute total temperature
u	velocity in x-direction
x	distance in axial direction, measured from nose of body
x_{tr}	distance in axial direction to transition strip

y	distance in radial direction, measured from body surface
γ	ratio of specific heats
δ	boundary-layer total thickness
δ^*	boundary-layer displacement thickness (see eq. (A2))
δ_u	boundary-layer velocity thickness (see eq. (A3))
θ	boundary-layer momentum thickness (see eq. (A1))
μ	absolute viscosity
ν	kinematic viscosity, $\frac{\mu}{\rho}$
ρ	mass density
σ	semivertex angle of body nose
τ	shearing stress

Subscripts:

c	cone
i	incompressible
inv	inviscid
max	maximum
t	total
∞	free-stream condition
δ	edge of boundary layer
w	wall

1	conditions upstream of normal shock
2	conditions downstream of normal shock

A bar over a symbol refers to flat-plate conditions.

A prime to a symbol indicates parameter evaluated at reference temperature.

APPARATUS AND TESTS

Wind Tunnel

The present investigation was conducted in the Langley 4- by 4-foot supersonic pressure tunnel, which is described in reference 13. This facility is a rectangular, closed-throat, single-return wind tunnel with provisions for control of pressure, temperature, and humidity of the enclosed air. The normal operating stagnation temperature is about 43° C.

Models

Eight bodies of revolution served as test models in this investigation. (See fig. 1.)

Model 1, the RM-10, was constructed of steel and duralumin; the other models were made of stainless steel. Surface roughness was estimated to be about 0.2 to 0.4 root-mean-square micron for all models. Specifications for these models are listed in table I.

The theoretical pressure distribution for each model, calculated by the method of characteristics, and the model profiles with the locations of the survey stations are shown in figure 2. A static pressure orifice was located at the approximate position of each survey station.

All models were mounted from the rear on a fixed sting at a nominal angle of attack of zero. The angle of attack was measured after the models were installed in the test section and was found to be, for all models, less than 0.2°.

Instrumentation

Boundary-layer surveys were made with total and static pressure probes mounted on a single support as shown in figure 3. The total pressure probe was made of 1.40-millimeter (O.D.) stainless-steel tubing flattened and honed at the tip to give an opening approximately 0.07 millimeter high. Since the model cross sections were circular and the pitot probe tip was flat, full contact between the two across the probe tip could not be made. The following sketch shows the approximate relationship between the probe tip and the model station with minimum body radius:

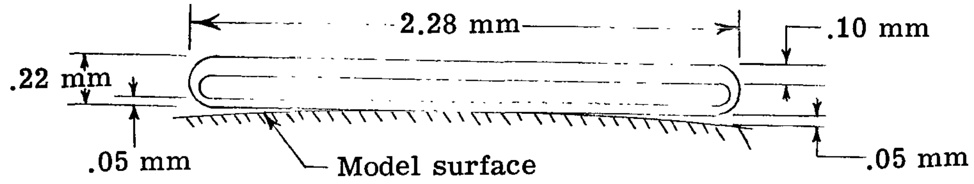

The static pressure probe was made of 1.40-millimeter (O.D.) stainless-steel tubing; it had a conical tip which was closed and pointed. Static pressure orifices consisted of four 0.51-millimeter-diameter holes drilled symmetrically around the tubing 20.23 millimeters from the probe tip.

The boundary-layer probe was mounted on an actuator system which had three-dimensional movement capability. The probe settings could be controlled to within 0.25 millimeter in the axial (x) and lateral directions and to within 0.08 millimeter in the radial (y) direction.

Total and static probe pressures were sensed by differential pressure transducers and their outputs were recorded on punch cards. Free-stream static pressure was used as the reference pressure for the differential transducers so that the lowest range transducer could be used for maximum accuracy. Tunnel stagnation and free-stream static (reference) pressures were measured by precision automatic indicating mercury manometers.

Boundary-layer surveys were made normal to the model center line, which is not normal to the local surface. The error due to this technique, however, is small, and no attempt was made to apply corrections to the data.

Test Conditions and Procedures

The turbulent boundary layers on each model were surveyed at $\frac{x}{l} \approx 0.56$ and 0.92. Additional surveys were made at $\frac{x}{l} \approx 0.79$ and 0.95 on model 1 to obtain measurements in the adverse pressure gradients of this region. Data were taken on all models at Mach numbers of 1.61 and 2.20 and stagnation pressures of 0.34, 1.01, and 1.70 atmospheres (1 atm = 101,325 N/m^2). Additional surveys were made at 0.68 and 1.36 atmospheres on model 1. These tests covered a free-stream Reynolds number range from 3.61×10^6 to 22.3×10^6 per meter and a Reynolds number range, based on x at the measuring station, from 1.2×10^6 to 27×10^6. The stagnation temperature was held constant for a given profile and varied from about 38° to 49° C throughout the test program, which was conducted under equilibrium conditions of negligible heat transfer.

At each test condition, the probe was moved away from the model far enough to prevent shock impingement on it from the probe so that model static pressures could be recorded. The total pressure probe was then moved over the station to be surveyed and brought into contact with the model surface as determined by electrical contact. The pitot traverse was performed by moving the probe away from the model in small increments and recording the data. The height of the impact probe above the test surface was determined from the surface contact point combined with the position transducer calibration.

Following the pitot pressure survey at each station, a similar procedure was used in performing the static pressure survey over the same location, except that no contact was made between the static probe and test surface. The height of the static probe above the model surface was determined from the impact probe calibration plus the measured difference in height between the pitot and static probes.

A fully turbulent boundary layer was assured on each model by cementing particles of number 30 sand roughness (0.65 mm diameter) near the nose. (See table II for location of transition strip x_{tr}.) Schlieren photographs of each model verified that the boundary layer was indeed turbulent. Because of the length of time required to complete a profile, it was not possible to survey all the model stations at each pressure. A summary of the stations and pressures at which surveys were made is given in table II.

REVIEW OF THEORETICAL METHODS

In order to have a basis of comparison with the experimental data, corresponding theoretical values were needed for the turbulent boundary layer in flat-plate and axisymmetric flow. This section presents a brief review of the methods used in this paper to calculate these quantities.

Momentum Thickness

Englert's method for calculating boundary-layer momentum thickness θ was chosen from among the several available methods (refs. 6 to 9) because of its mathematical simplicity. This method tends to underpredict flat-plate momentum thickness. This deficiency, however, can be largely overcome by using it to predict the ratio of axisymmetric to flat-plate momentum thickness $\theta/\overline{\theta}$ and then applying this ratio to a reliable flat-plate method to find the modified theoretical values, as is done herein.

Englert's momentum thickness equation, which is an extension of Truckenbrodt's (ref. 14) incompressible flow equation to compressible flow by a Stewartson type of transformation, can be written as

$$\theta = \frac{\left(1 + 0.2M_\delta^2\right)^3}{M_\delta^3 r}\left[\frac{0.0076\left(\frac{\nu_t}{a_t}\right)^{0.167}}{\left(1 + 0.2M_\delta^2\right)^{-0.119}}\int_0^x \frac{M_\delta^{3.333} r^{1.167}}{\left(1 + 0.2M_\delta^2\right)^4}\,dx\right]^{0.857} \tag{1}$$

where γ has been assumed to be 1.4.

This equation is applicable only where the fully developed turbulent boundary layer is very thin relative to the body radius and where there is no static pressure or total temperature gradients across the boundary layer. In addition, the conventional assumption is made of no variation in the inviscid flow field through the boundary-layer thickness. (See appendix A for a more detailed discussion of this subject.)

For the Mach numbers and body shapes in this investigation, virtually no accuracy is lost in evaluating θ (less than ±1 percent) when free-stream conditions are assumed to exist over the length of the body. Hence,

$$\theta = \frac{\left(1 + 0.2M_\infty^2\right)^{-0.326}}{rM_\infty^{0.143}}\left[0.0076\left(\frac{\nu_t}{a_t}\right)^{0.167}\int_0^x r^{1.167}dx\right]^{0.857} \tag{2}$$

Dividing this general equation by the corresponding equation for flat-plate flow (i.e., r = Constant) gives, for the same free-stream flow conditions,

$$\frac{\theta}{\overline{\theta}} = \frac{\left(\int_0^x r^{1.167}dx\right)^{0.857}}{rx^{0.857}} \tag{3}$$

For the special case of the cone, inserting $r = mx$ into equation (3) yields

$$\frac{\theta_c}{\overline{\theta}} = 0.515 \tag{4}$$

Substituting the flat-plate flow momentum equation

$$\overline{\theta} = \frac{x}{2}\overline{C_F} \tag{5}$$

into equation (4) gives

$$\theta_c = 0.2575x\overline{C_F} \tag{6}$$

Flat-plate flow average skin-friction coefficients $\overline{C_F}$ were estimated by the reference temperature method of Sommer and Short (ref. 15), which has been shown by Peterson (ref. 16) to be a very good flat-plate theory for the range of Mach numbers and Reynolds numbers in this investigation.

Displacement Thickness

In order to calculate theoretical boundary-layer displacement thickness δ^*, or boundary-layer total thickness δ, in either flat-plate or axisymmetric flow, some assumption must be made for the boundary-layer velocity profile. Throughout this report, a 1/7-power profile law is assumed, where required, in calculating theoretical quantities.

For flat-plate flow the displacement thickness can be calculated from flat-plate skin friction by

$$\overline{\delta^*} = \left(\frac{\overline{\delta^*}}{\overline{\theta}}\right)\overline{\theta} = \left(\frac{\overline{\delta^*}}{\overline{\theta}}\right)\frac{x}{2}\overline{C_F} \tag{7}$$

where the values of $\overline{\delta^*}/\overline{\theta}$ are calculated and tabulated by Tucker (ref. 17) as functions of the Mach number at the edge of the boundary layer M_δ and the velocity-profile index n.

Similarly in axisymmetric flow

$$\delta^* = \left(\frac{\delta^*}{\theta}\right)\left(\frac{\theta}{\overline{\theta}}\right)\overline{\theta} \tag{8}$$

Inserting equations (3) and (5) into equation (8) yields

$$\delta^* = \left(\frac{\delta^*}{\theta}\right)\frac{\left(\int_0^x r^{1.167}dx\right)^{0.857}}{2r}x^{0.143}\overline{C_F} \tag{9}$$

For the same velocity profile, the values of δ^*/θ on a body of revolution are slightly higher due to body radius than the corresponding flat-plate values. By using the calculation procedure of reference 18, it was found that the values of δ^*/θ are a maximum of 4 percent higher than the corresponding flat-plate values, based on the largest experimental value of δ/r. Because this effect is small, flat-plate values are used in this report.

Equation (9) then becomes

$$\delta^* = \left(\frac{\overline{\delta^*}}{\overline{\theta}}\right)\frac{\left(\int_0^x r^{1.167}dx\right)^{0.857}}{2r}x^{0.143}\overline{C_F} \tag{10}$$

For the slender cone, inserting $r = kx$ into equation (10) yields

$$\delta_c^* = \left(\frac{\overline{\delta^*}}{\overline{\theta}}\right)0.2575x\overline{C_F} \tag{11}$$

Boundary-Layer Total Thickness

Flat-plate boundary-layer total thickness can be calculated from the flat-plate skin friction by

$$\bar{\delta} = \left(\frac{\bar{\delta}}{\bar{\theta}}\right)\bar{\theta} = \left(\frac{\bar{\delta}}{\bar{\theta}}\right)\frac{x}{2}\overline{C_F} \tag{12}$$

where the values of $\left(\bar{\delta}/\bar{\theta}\right)$ are calculated and tabulated by Tucker (ref. 17) as functions of M_δ and n.

Similarly in conical flow

$$\delta_c = \left(\frac{\delta_c}{\theta_c}\right)\theta_c \tag{13}$$

which yields, after introducing equation (6),

$$\delta_c = \left(\frac{\delta_c}{\theta_c}\right)0.2575x\overline{C_F} \tag{14}$$

For the same velocity profile ($n = 7$ in this paper) the values of δ_c/θ_c are somewhat lower than the corresponding flat-plate values. The magnitude of this difference depends on the ratio of boundary-layer total thickness to body radius δ_c/r. It was estimated from the calculation procedure of reference 18 that, for the values of δ_c/r encountered in this investigation $\left(0.232 < \frac{\delta_c}{r} < 0.353\right)$, δ_c/θ_c is approximately 6.8 to 9.5 percent lower than $\bar{\delta}/\bar{\theta}$. This range of corrections resulted in the δ_c theory, calculated from equation (14), being a narrow band instead of a single curve.

Local Skin Friction

Reshotko and Tucker (ref. 6) give an equation for local skin-friction coefficient over an arbitrary body in compressible flow. Their coefficient based on q_δ can be converted to

$$C_f = 0.246e^{-1.561H_i}\left(\frac{u_\delta \theta}{\nu'}\right)^{-0.268}\left(\frac{T_\delta}{T'}\right)^{1.268}\left(\frac{q_\delta}{q_\infty}\right) \tag{15}$$

where C_f is based on q_∞. Equation (15) is essentially a transformation of the Ludwieg-Tillmann incompressible flow equation (ref. 19) to compressible flow by the reference temperature concept. Dividing this general equation by the corresponding flat-plate equation and using Sommer and Short's reference temperature yields, for the same free-stream flow conditions,

$$\frac{C_f}{\overline{C_f}} = e^{1.561\left(\overline{H_i} - H_i\right)}\left(\frac{\overline{\theta}}{\theta}\right)^{0.268}\left(\frac{1 + 0.1151M_\infty^2}{1 + 0.1151M_\delta^2}\right)^{0.732}\left(\frac{1 + 0.2M_\infty^2}{1 + 0.2M_\delta^2}\right)^{2.964}\left(\frac{M_\delta}{M_\infty}\right)^{1.732} \tag{16}$$

Equation (16) was simplified for use in this paper by assuming that $H_i = \overline{H_i}$ for all the flow conditions encountered in this investigation. Sample skin-friction calculations, in which H_i was evaluated by the method of Englert (ref. 9), were made for model 1 and revealed that the errors involved in this assumption are less than 1 percent over the last three-fourths of the body length. Near the nose the error rose to about 5 percent. This assumption introduced into equation (16) yields

$$\frac{C_f}{\overline{C_f}} = \left(\frac{\overline{\theta}}{\theta}\right)^{0.268}\left(\frac{1 + 0.1151M_\infty^2}{1 + 0.1151M_\delta^2}\right)^{0.732}\left(\frac{1 + 0.2M_\infty^2}{1 + 0.2M_\delta^2}\right)^{2.964}\left(\frac{M_\delta}{M_\infty}\right)^{1.732} \tag{17}$$

If the momentum-thickness ratio given by equation (3) is used in equation (17), the local skin-friction ratio over an arbitrary body in terms of the body profile is therefore

$$\frac{C_f}{\overline{C_f}} = \frac{r^{0.268}x^{0.230}}{\left(\int_0^x r^{1.167}dx\right)^{0.230}}\left(\frac{1 + 0.1151M_\infty^2}{1 + 0.1151M_\delta^2}\right)^{0.732}\left(\frac{1 + 0.2M_\infty^2}{1 + 0.2M_\delta^2}\right)^{2.964}\left(\frac{M_\delta}{M_\infty}\right)^{1.732} \tag{18}$$

Inserting $r = mx$ into equation (18) gives the conical flow equation

$$\frac{C_{f,c}}{\overline{C_f}} = 1.194\left(\frac{1 + 0.1151M_\infty^2}{1 + 0.1151M_\delta^2}\right)^{0.732}\left(\frac{1 + 0.2M_\infty^2}{1 + 0.2M_\delta^2}\right)^{2.964}\left(\frac{M_\delta}{M_\infty}\right)^{1.732} \tag{19}$$

For the special case of the slender cone, inserting $M_\delta = M_\infty$ into equation (19) yields

$$\frac{C_{f,c}}{\overline{C_f}} = 1.194 \tag{20}$$

This equation agrees well with expressions which have been derived by several investigators. (See refs. 1 to 3.) Because the differences in the theories were of the same order as the scatter in the cone data, no attempt was made to determine the relative accuracies of these theories.

Average Skin Friction

Several expressions have been derived by various authors which relate the average turbulent skin friction on a slender cone to that on a flat plate of equal length. (See refs. 1, 4, and 5.) From these theories the average turbulent skin friction is found to be approximately 4 percent higher on a slender cone than on the flat plate. Hence, the following expression is used in this report:

$$\frac{C_{F,c}}{C_F} = 1.04 \tag{21}$$

DATA REDUCTION

Velocity Profiles

Data from the total and static pressure boundary-layer profiles were combined by using the Rayleigh pitot formula

$$\frac{p_{t,2}}{p_1} = \left(\frac{\gamma + 1}{2}M_1{}^2\right)^{\frac{\gamma}{\gamma-1}} \Bigg/ \left(\frac{2\gamma}{\gamma + 1}M_1{}^2 - \frac{\gamma - 1}{\gamma + 1}\right)^{\frac{1}{\gamma-1}} \tag{22}$$

to yield the Mach number profiles. The tables of reference 20 were used in the computations. The Mach number profiles combined with the energy equation in the form

$$\frac{T_t}{T} = 1 + \frac{\gamma - 1}{2}M^2 \tag{23}$$

were then used to calculate the velocity profiles from the following equation (with constant total temperature assumed across the boundary layer):

$$\frac{u}{u_\delta} = \frac{Ma}{M_\delta a_\delta} = \frac{M}{M_\delta}\sqrt{\frac{T}{T_\delta}} = \frac{M}{M_\delta}\sqrt{\frac{1 + \frac{\gamma - 1}{2}M_\delta{}^2}{1 + \frac{\gamma - 1}{2}M^2}} \tag{24}$$

Since a flattened impact probe was used to minimize the probe displacement effects, no corrections for these effects were applied to the velocity-profile data. Sample calculations using the criterion of reference 21 reveal that the maximum correction that would have been required for the data in this paper is 0.03 millimeter, which is negligible.

The largest Knudsen number encountered in this investigation, based on probe height and gas mean free path, was calculated to be approximately 0.01. This value indicates that the limits of continuum flow have not been exceeded even for data obtained very close to the model surface at the minimum stagnation pressures.

Integral Thicknesses

Equations for the calculation of the boundary-layer integral thicknesses are derived in appendix A of this paper. They differ slightly from those normally used in that variations of static pressure and inviscid pitot pressure through the boundary-layer thickness are taken into account. Accuracy gained by reducing data in this manner, rather than in the conventional manner, is discussed in the section entitled "Results and Discussion."

Boundary-Layer Total Thickness

The experimental bounday-layer total thickness δ of each profile was assumed to be the intersection of the pitot pressure profile and the inviscid pitot pressure profile. (See sketch 1 in appendix A.) In practice, this thickness was taken to be the distance above the test surface of the first experimental impact pressure on the linear portion of the pitot pressure profile.

Local Skin Friction

Local skin-friction ratios were calculated from the experimental momentum thicknesses and Mach numbers by using equation (17) combined with equation (5) to yield

$$\frac{C_f}{\overline{C_f}} = \left(\frac{x}{2}\frac{\overline{C_F}}{\theta}\right)^{0.268}\left(\frac{1 + 0.1151M_\infty{}^2}{1 + 0.1151M_\delta{}^2}\right)^{0.732}\left(\frac{1 + 0.2M_\infty{}^2}{1 + 0.2M_\delta{}^2}\right)^{2.964}\left(\frac{M_\delta}{M_\infty}\right)^{1.732} \tag{25}$$

Average Skin Friction

The equation used to compute the average skin-friction coefficients from the experimental data is derived in appendix B (eq. (B11)) to be

$$C_F = \frac{q_\delta}{q_\infty}\frac{4\pi r\theta}{S}$$

This equation is relatively simple to use since it requires experimental measurements only at the model station where C_F is to be evaluated. It is an approximation of the usual method of calculating C_F which consists of deriving τ_w from an elemental control volume and then integrating τ_w over the body surface to obtain the friction drag. The usual method, however, is difficult to use in pressure gradient flow because it requires integration of the pressure gradient over the body surface. The differences between these methods are treated more fully in the section entitled "Results and Discussion."

RESULTS AND DISCUSSION

The presentation of results begins with the velocity profiles and proceeds to the gross quantities which are presented in the order that they are treated in the section "Data Reduction." For convenience, the gross quantities are listed in table III in addition to being presented in subsequent figures.

Velocity Profiles

Experimental velocity profiles in the form of y/θ as a function of u/u_δ are shown in figures 4 and 5. The momentum thickness was chosen for the nondimensionalizing parameter because it is a more accurately measured quantity than is the boundary-layer total thickness. The profiles do not show, in general, any appreciable increase in fullness with increasing stagnation pressure; this indicates that the velocity profile index n should remain fairly constant with Reynolds number. The experimental value of n for each profile was determined by finding the slope of the best straight-line fit to the data when plotted in log-log form. Sample velocity profiles plotted in this manner and the power profile line drawn through the data are given in figure 6. These sample plots cover the range of pressure gradients encountered in this investigation.

This figure shows that the data points very near the wall deviate from the power profile which best fits the data in the central part of the boundary layer. Also, the power profile which best approximates the data does not intersect $\frac{u}{u_\delta} = 1$ at the edge of the experimental boundary layer but at a somewhat lower value of y/θ. For this reason, the power profile can be used to predict the integral thicknesses with a good degree of accuracy, but it tends to underpredict the boundary-layer thicknesses.

The values of n obtained in this manner are shown in figure 7 as a function of Reynolds number based on momentum thickness R_θ, rather than Reynolds number based on length R_x, in order to facilitate comparison with the "equivalent" flat-plate values of reference 22. "Equivalent" flat-plate conditions are considered to be those which have equal values of R_θ. As expected from figures 4 and 5, the values of n are relatively constant with Reynolds number. They do, however, show a slight increase with free-stream Mach number. Figure 7 indicates that the experimental profiles do not differ greatly from profiles calculated by using a 1/7-power law, which was assumed in several of the theories used in this paper.

Momentum Thickness

The theoretical momentum thickness distributions are calculated by equation (3) and shown in figure 8. Note that the cone curve is constant and that the parabolic-arc-body curves (models 1, 6, and 7) approach the cone curve as the nose of the body is approached. The effect of the boattailed afterbody on model 1 is a very rapid increase in momentum thickness in this region.

When the flat-plate momentum thicknesses $\overline{\theta}$ in equation (3) are estimated by Sommer and Short's reference temperature method (ref. 15), the resulting momentum thicknesses can be compared with the experimental data in figures 9 to 15. In these figures, ticks are used to differentiate between the various stagnation pressure levels. The cone data, taken as a whole, average quite well around the theory curve (fig. 9). The data from model 1 (fig. 10) are, in general, in good agreement with theory and verify the rapid increase in θ on the boattail predicted by theory.

The data from the remaining models (figs. 11 to 15) are found to be in fairly good agreement with theory, with the exception of model 3. It should be noted that this model has a fineness ratio of 6.1, whereas all other models have fineness ratios of about 12.2. Because of the assumptions in the derivation, equation (3) would be expected to be less accurate for the "thicker" body.

Displacement Thickness

Theoretical displacement thicknesses calculated by equation (10) are compared with the experimental data in figures 16 to 22. The trends of the displacement thickness results are the same as those of the momentum thickness results. This good agreement between prediction and experiment for both momentum thickness and displacement thickness indicates that the assumptions of $\frac{\delta^*}{\theta} \approx \frac{\overline{\delta^*}}{\overline{\theta}}$ and $n \approx \frac{1}{7}$ were satisfactory in predicting displacement thickness.

Boundary-Layer Total Thickness

The boundary-layer total thickness data are presented in figure 23, in which the flat-plate and cone curves are included for comparison. This figure shows poor agreement between the cone data and theory. There appears to be two reasons for this disagreement. First, the thickness of a boundary layer is, by nature, hard to measure accurately. Hence, boundary-layer thickness data will contain more experimental errors than, say, the integral thickness data. This error tends to be random in nature. Second, the theoretical curves were calculated with the assumption of a power profile for the boundary-layer velocity distribution. A power profile is designed to give good estimates of the integral thicknesses by matching the data in the central part of the boundary layer without regard for the edge of the boundary layer (fig. 6). Hence, the power profile law abruptly ends at $\frac{u}{u_\delta} = 1$, whereas the experimental data approach $\frac{u}{u_\delta} = 1$ in a more asymptotic fashion. For this reason the power profile tends to underpredict the true boundary-layer thickness so that the theoretical curves of figure 23 are, in effect, too low.

Shape Parameters

A comparison of experimental δ^*/θ values with flat-plate theoretical values, as obtained from reference 17, is presented in figure 24. Note that the values of δ^*/θ correspond to a range of n which is in good agreement with those experimentally measured and presented in figure 7. There is a general increase in n from $M_\infty = 1.61$ to $M_\infty = 2.20$. Note that this trend was also present in the velocity-profile-index measurements of figure 7.

It is sometimes more useful to use the velocity thickness δ_u rather than the displacement thickness δ^* as a correlating parameter. A comparison of figures 24 and 25 shows that δ_u/θ is less affected by compressibility and is more sensitive to changes in velocity profile index than is δ^*/θ. It would be more accurate, for example, to use δ_u/θ in determining n from the integral thicknesses. Note that the experimental velocity-profile-index agreement between figures 24 and 25 is quite good, with both figures showing a slight increase in n with free-stream Mach number.

A comparison of figure 24 with figures 9 to 22, indicates that, although the body shape has a strong influence on the momentum and displacement thickness growth on the test models, δ^*/θ shows no strong influence of body shape. The ratios are not, in fact, greatly different from the flat-plate flow values. This agreement is not entirely unexpected since δ^*/θ is primarily a function of the shape of the velocity profile, and it has been shown in figure 7 that the experimental velocity profiles are approximately equal to those on an "equivalent" flat plate.

Local Skin Friction

Theoretical local skin-friction-coefficient ratios $C_f/\overline{C_f}$ calculated from the body profile through equation (18) are shown in figure 26. These calculations indicate local skin-friction ratios on some models which are higher near the nose than slender-cone values. This difference occurs because the parabolic-arc and cone—parabolic-arc models are not "slender" near the nose, so that their skin-friction ratios would not be expected to approach those of slender cones. However, each ratio would approach the value for a cone which had a slope equal to the slope of the body at the nose.

Flat-plate local skin-friction coefficients $\overline{C_f}$ were estimated by the Sommer and Short reference temperature method (ref. 15). Sample calculations (at $M_\infty = 2.20$

and $p_t = 1.01$ atm) of $\overline{C_f}$ from equation (15) indicated a difference of only 2 percent from Sommer and Short's values over the length of the longest body in this investigation.

The experimental data were obtained from equation (25), where the values of $\overline{C_f}$ were calculated by the reference temperature method of reference 15. The resulting data are compared with the theoretical curves in figures 27 to 34. Figure 27 presents a summary of the experimental data, with the theoretical flat-plate and cone curves included for comparison. This figure is too congested to show the individual trends of each model; therefore, the data have been replotted in figures 28 to 34 to indicate the individual trends and to facilitate comparison with the theoretical curves. Since the RM-10 (model 1) had the largest nose slope ($\approx 7.5^{\circ}$), the $\sigma = 7.5^{\circ}$ cone curve is included in figures 29 to 34 to show the asymptotic limit that the parabolic-arc data should approach near the nose.

Figure 28 gives a summary of the cone data (models 2 and 5). Very good agreement is seen between experiment and theory at both Mach numbers. The local skin-friction-coefficient distribution on model 1 is presented in figure 29. Good agreement between theory and experiment is indicated, including the rapid decrease in C_f on the boattailed afterbody. The data from the remaining models (figs. 30 to 34) show, in general, good agreement between calculation and experiment.

Average Skin Friction

Experimental average skin-friction coefficients, calculated from the experimental momentum thicknesses with the use of equation (B11), are presented in figure 35. The flat-plate and slender-cone theory curves are included for comparison. The data show more scatter than the local skin-friction data, but the trends of the two are similar. The decrease in average skin friction on the boattail afterbody of model 1, which must accompany the decrease in local skin friction, is present in the data. The data from the remaining models are, in general, above the data from model 1 but below the cone data (models 2 and 5). This trend, also, is compatible with the local skin-friction data. For the cone, the average skin-friction data do not show the good agreement with theory as do the local skin-friction data. One reason for this is that average skin friction was calculated from experimental momentum thicknesses raised to the first power, whereas local skin friction was calculated from the same momentum thicknesses to the 0.268 power. This procedure would tend to suppress any disagreement between theory and experiment for the local skin-friction results. One interesting point to note is that the rapid decrease in shearing stress on the aft part of a boattailed body of revolution could result in average skin-friction coefficients over the length of the body which are lower than flat-plate values.

Sample average skin-friction coefficients on three models (models 1, 2, and 5) were calculated by the conventional method to compare with those calculated by the method used in this paper. The conventional method of calculating C_F is by integrating Von Karman's momentum equation to yield

$$C_F = \frac{4\pi}{S}\left\{\frac{r\rho_\delta u_\delta^2}{\rho_\infty u_\infty^2}\int_0^\delta \frac{\rho u}{\rho_\delta u_\delta}\left(1 - \frac{u}{u_\delta}\right)\left(\frac{r + y}{r}\right)dy\right.$$

$$\left. + \int_0^x \frac{r\rho_\delta u_\delta}{\rho_\infty u_\infty^2}\left[\int_0^\delta\left(1 - \frac{\rho u}{\rho_\delta u_\delta}\right)\left(\frac{r + y}{r}\right)dy\right]\frac{\partial u_\delta}{\partial x}\,dx\right\} \tag{26}$$

This equation is easily applied to the cones (models 2 and 5), since the pressure (or velocity) gradient term is zero for these models. The sample calculations for the parabolic-arc bodies, however, were confined to model 1, since only on this model were a sufficient number of stations surveyed so that reasonable estimates of the pressure gradient term could be made. All quantities in the integrand of the pressure gradient term, except $\partial u_\delta/\partial x$, were evaluated from the experimental data. The quantity $\partial u_\delta/\partial x$ was calculated at each experimental station from characteristics theory. The resulting integrands were graphically integrated to obtain the pressure gradient term.

The results, presented in figure 36, confirm that the two methods of calculating C_F give excellent agreement in conical flow, as would be expected. The disagreement for model 1 is as much as 5 percent. It is possible that the disagreement for model 3 could be greater than this value, since this model has larger pressure gradients than model 1.

Figure 37 shows the reason for the disagreement between the two methods of calculating C_F for the pressure gradient bodies. In this figure the model 1 data of figure 36 have been replotted in a manner to reveal the contributions of each of the terms in equation (26). The pressure gradient term in this equation is seen to "correct" the first term in the direction of higher skin friction. The calculations of equation (B11) which, in effect, also corrects the first term in equation (26), are similarly in the direction of higher skin friction. The magnitudes of these corrections, however, are not as large as those of the pressure gradient term of equation (26).

The disagreement between the two methods, therefore, arises from (1) the overestimation of the pressure gradient term in equation (26), and/or (2) the linear approximation for the inviscid pitot pressure profile which underestimates the effects of the inviscid flow field in equation (B11). However, equation (B11) is an improvement over the conventional zero-pressure-gradient skin-friction equation (the first term in eq. (26)).

Effects of Variation of Static Pressure and Inviscid Flow Properties Through the Boundary-Layer Thickness

As described in appendix A of this paper, the static and pitot pressure profiles were recorded outside the boundary layer so that the Mach number profiles under essentially inviscid flow conditions could be obtained and extrapolated to the model surface. Using these profiles to calculate the integral thicknesses by equations (A4), (A5), and (A6) resulted in data which are different in two respects from those which are normally computed. First, the static-pressure variation through the boundary-layer thickness was included in the data. Second, corrections were made for the inviscid pitot-pressure variations through the boundary-layer thickness.

Figure 38 presents typical experimental pressure-coefficient and inviscid Mach number profiles and the corresponding profiles (solid curves) calculated by the method of characteristics. The trend of the experimental and theoretical profiles in the boundary layer is the same, and the disagreement between the two profiles, in terms of Mach number and absolute pressure, is less than 2 percent. The calculations by the method of characteristics also indicate that the linearity approximation for the profiles appears to be adequate in the boundary layer.

Static pressure orifices were at the approximate locations of the survey stations on each model. Comparisons of the model static pressures, the probe static pressures extrapolated to the model surface, and the theoretical pressures calculated by the method of characteristics reveal, in general, differences in the three sets of data which are less than ±2 percent.

Experimental integral thicknesses were calculated a second time, with constant static and inviscid pitot pressures through the boundary-layer thickness assumed. These data were then compared with the original computations to get the effects of the nonuniform inviscid flow field. The results indicate that the static pressure and the pitot pressure varied as much as 2.6 percent and 1 percent, respectively, through the boundary-layer thickness. It was found that maximum errors of only 0.6 percent in θ and 0.3 percent in δ^* would have been introduced by assuming constant static pressure through the boundary-layer thickness. Hence, neglecting $\partial p/\partial y$ through the boundary-layer thickness, which is the usual practice, would have given good results in this study. Accounting for the inviscid pitot pressure variation through the boundary-layer thickness resulted in corrections of as much as 5 percent in momentum thickness and 3.5 percent in displacement thickness.

CONCLUSIONS

An experimental study has been performed to determine the turbulent-boundary-layer characteristics of several bodies of revolution at 0° angle of attack in supersonic flow. Based on the results of this investigation, the following conclusions are believed to be justified:

1. Body profile shape has a strong influence on turbulent-boundary-layer integral thicknesses and skin friction in axisymmetric flow. These body-shape effects can be estimated with a fairly good degree of accuracy on slender bodies by combining existing axisymmetric flow theories with an accurate flat-plate theory.

2. Although the body shapes in this study had a strong influence on the growth of displacement and momentum thicknesses, the thickness ratio, commonly called the shape factor, remained approximately equal to the flat-plate shape factor.

3. No systematic variation of velocity profile index with Reynolds number was found; however, a slight increase with free-stream Mach number was noticed.

4. The static pressure varied as much as 2.6 percent through the boundary-layer thicknesses in this investigation, but accounting for this variation resulted in a negligible increase in accuracy in the integral thicknesses. The inviscid pitot pressure varied a maximum of 1 percent through the boundary-layer thickness, but accounting for this variation resulted in corrections in momentum thickness of as much as 5 percent and in displacement thickness of as much as 3.5 percent.

Langley Research Center,
National Aeronautics and Space Administration,
Langley Station, Hampton, Va., February 20, 1967,
126-13-02-12-23.

APPENDIX A

INTEGRAL-THICKNESS DATA REDUCTION TECHNIQUE

Since solutions of the inviscid flow equations for the parabolic-arc bodies used in this investigation reveal that the inviscid flow properties are not constant in the radial direction, it was decided not to use the conventionally defined boundary-layer integral equations which, in effect, assume that inviscid flow properties are constant through the boundary-layer thickness and equal to those at the edge of the boundary layer. Instead, equations similar to those of references 11, 12, and 23 were used as the general expressions for the integral parameters in compressible flow over slender axisymmetric bodies where the inviscid flow properties are nonuniform. These equations are as follows:

Momentum thickness

$$\theta = \int_0^{\delta} \frac{\rho u}{\rho_\delta u_\delta}\left(\frac{u_{inv} - u}{u_\delta}\right)\left(\frac{r + y}{r}\right)dy \tag{A1}$$

Displacement thickness

$$\delta^* = \int_0^{\delta}\left(\frac{\rho_{inv}u_{inv} - \rho u}{\rho_\delta u_\delta}\right)\left(\frac{r + y}{r}\right)dy \tag{A2}$$

Velocity thickness

$$\delta_u = \int_0^{\delta}\left(\frac{u_{inv} - u}{u_\delta}\right)\left(\frac{r + y}{r}\right)dy \tag{A3}$$

Note that for constant inviscid conditions, these equations reduce to their more familiar forms. These equations differ from those of the aforementioned references in the following respects: (1) Reference 11 omits the radius term in the foregoing equations and thereby assumes two-dimensional flow. (2) Reference 12 uses wall conditions as a reference instead of the boundary-layer edge conditions used in equations (A1) to (A3). (3) Reference 23 derives the equations for a viscous wake instead of a boundary layer.

Approximations to the true inviscid flow conditions were made experimentally by measuring pitot pressure profiles external to the boundary layer, where viscous forces are negligible, and linearly extrapolating these profiles through the boundary layer to the model surface. The profiles thus determined are termed "inviscid" in this report. In addition, linear approximations to the static pressure profiles were obtained by experimentally measuring static pressures in the radial direction and fitting the best straight line through the data. Typical static, pitot, and inviscid pitot pressure profiles are shown in sketch 1.

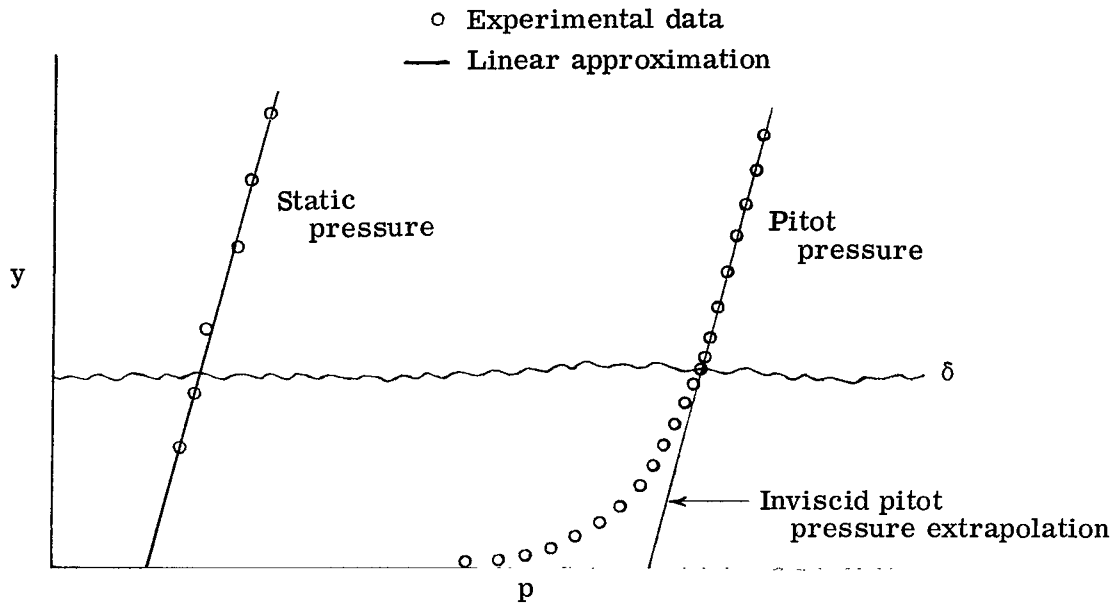

Sketch 1

The static and pitot pressure profiles were combined by using the Rayleigh pitot formula, equation (22), to form the Mach number profiles. Similarly, the static and inviscid pitot pressure profiles were combined to form the inviscid Mach number profiles. These two profiles are illustrated in sketch 2.

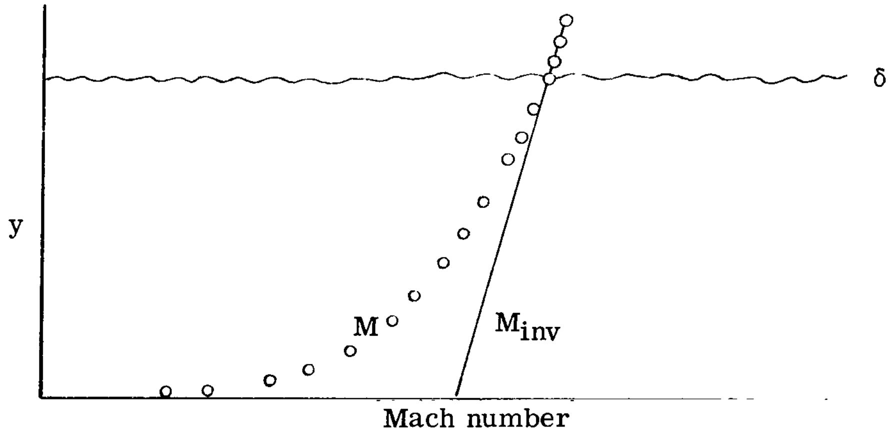

Sketch 2

The difference between these two profiles is the measure of the viscous effect of the boundary layer and is taken into account by using the integral parameters in the form of equations (A1), (A2), and (A3). These equations, when written in terms of pressure and Mach number, become

$$\theta = \int_0^\delta \frac{p}{p_\delta} \frac{M}{M_\delta} \sqrt{\frac{1 + \frac{\gamma - 1}{2} M^2}{1 + \frac{\gamma - 1}{2} M_\delta^2}} \left(\frac{M_{inv}}{M_\delta} \sqrt{\frac{1 + \frac{\gamma - 1}{2} M_\delta^2}{1 + \frac{\gamma - 1}{2} M_{inv}^2}} - \frac{M}{M_\delta} \sqrt{\frac{1 + \frac{\gamma - 1}{2} M_\delta^2}{1 + \frac{\gamma - 1}{2} M^2}} \right) \left(\frac{r + y}{r} \right) dy \qquad (A4)$$

$$\delta^* = \int_0^\delta \frac{p}{p_\delta} \left(\frac{M_{inv}}{M_\delta} \sqrt{\frac{1 + \frac{\gamma - 1}{2} M_{inv}^2}{1 + \frac{\gamma - 1}{2} M_\delta^2}} - \frac{M}{M_\delta} \sqrt{\frac{1 + \frac{\gamma - 1}{2} M^2}{1 + \frac{\gamma - 1}{2} M_\delta^2}} \right) \left(\frac{r + y}{r} \right) dy \qquad (A5)$$

and

$$\delta_u = \int_0^\delta \left(\frac{M_{inv}}{M_\delta} \sqrt{\frac{1 + \frac{\gamma - 1}{2} M_\delta^2}{1 + \frac{\gamma - 1}{2} M_{inv}^2}} - \frac{M}{M_\delta} \sqrt{\frac{1 + \frac{\gamma - 1}{2} M_\delta^2}{1 + \frac{\gamma - 1}{2} M^2}} \right) \left(\frac{r + y}{r} \right) dy \qquad (A6)$$

The integrands of these equations were evaluated at each point sampled in the boundary-layer pitot pressure survey. The integrations were performed numerically by the trapezoidal rule.

The integral thicknesses calculated by equations (A4), (A5), and (A6) are a more accurate representation of the boundary-layer effects than are the conventionally defined thicknesses, since the conventional definitions make no attempt to exclude the effects of changes in the inviscid flow field through the boundary-layer thickness.

APPENDIX B

AVERAGE-SKIN-FRICTION EQUATION

An approximate expression relating the average skin friction on a body of revolution in supersonic flow to the unconventionally defined momentum thickness θ defined by equation (A1) is derived in this appendix. The flow field is shown in the following sketch:

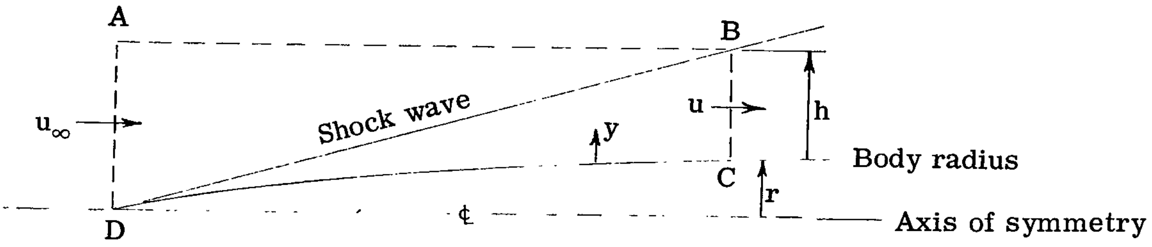

From the theorem of conservation of momentum, the net flux of momentum of the fluid moving through the axisymmetric control volume defined by surface ABCD is equal to the total force acting on the control volume; this is illustrated in the following sketches:

Momentum flux in x-direction

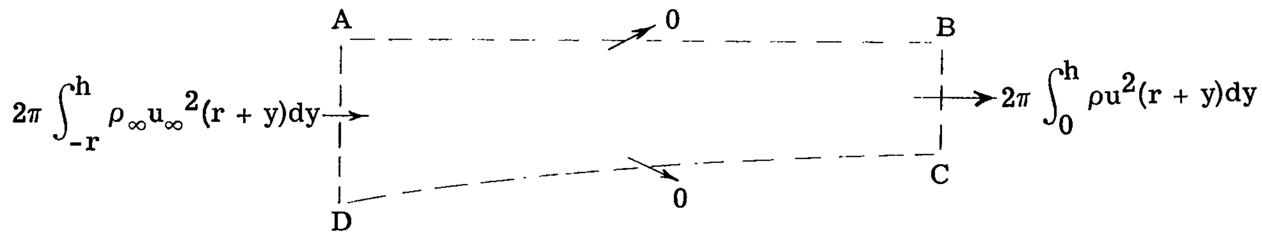

Total forces in x-direction

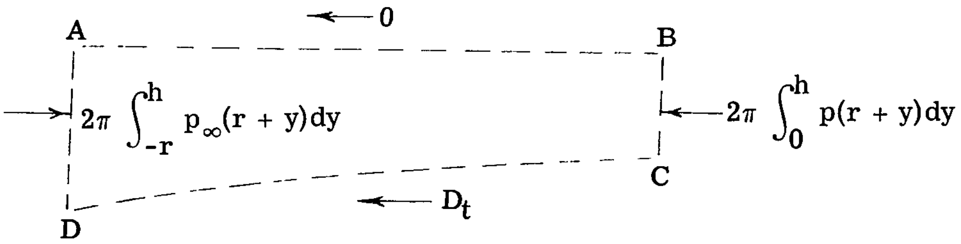

Equating the forces and momentum flux results in

$$D_t = 2\pi \left[\int_{-r}^{h} p_\infty (r + y) dy - \int_{0}^{h} p(r + y) dy + \int_{-r}^{h} \rho_\infty u_\infty^2 (r + y) dy - \int_{0}^{h} \rho u^2 (r + y) dy \right] \qquad \text{(B1)}$$

where h is the shock height. The total drag in an inviscid flow field can be seen from equation (B1) to be

$$D_{inv} = 2\pi\left[\int_{-r}^{h_{inv}} p_\infty(r + y)dy - \int_0^{h_{inv}} p_{inv}(r + y)dy + \int_{-r}^{h_{inv}} \rho_\infty u_\infty^2(r + y)dy - \int_0^{h_{inv}} \rho_{inv}u_{inv}^2(r + y)dy\right] \qquad (B2)$$

Assuming that the radial pressure distribution and the shape of the shock wave are not changed by the presence of the boundary layer $\left(\text{i.e., } p = p_{inv} \text{ and } h = h_{inv}\right)$ results in

$$D_F = D_t - D_{inv} = 2\pi\left[\int_0^h \rho_{inv}u_{inv}^2(r + y)dy - \int_0^h \rho u^2(r + y)dy\right] \qquad (B3)$$

But, continuity requires that

$$\int_0^h \rho u(r + y)dy = \int_0^h \rho_{inv}u_{inv}(r + y)dy \qquad (B4)$$

or

$$u_{inv}\int_0^h \rho u(r + y)dy = u_{inv}\int_0^h \rho_{inv}u_{inv}(r + y)dy \qquad (B5)$$

If the radial inviscid velocity gradient is assumed to be small,

$$\int_0^h \rho u u_{inv}(r + y)dy \approx \int_0^h \rho_{inv}u_{inv}^2(r + y)dy \qquad (B6)$$

Inserting equation (B6) into equation (B3) yields

$$D_F = 2\pi\int_0^h \rho u(u_{inv} - u)(r + y)dy \qquad (B7)$$

which can also be written

$$D_F = 2\pi\left[\int_0^\delta \rho u(u_{inv} - u)(r + y)dy + \int_\delta^h \rho u(u_{inv} - u)(r + y)dy\right] \qquad (B8)$$

But, at $y \geqq \delta$, $u = u_{inv}$ so that the second term in equation (B8) is zero. Hence,

$$D_F = 2\pi\int_0^\delta \rho u(u_{inv} - u)(r + y)dy \qquad (B9)$$

In coefficient form, equation (B9) is

$$C_F = \left(\frac{q_\delta}{q_\infty}\right)\frac{D_F}{q_\delta S} = \left(\frac{q_\delta}{q_\infty}\right)\frac{4\pi r}{S}\int_0^\delta \frac{\rho u}{\rho_\delta u_\delta}\left(\frac{u_{inv} - u}{u_\delta}\right)\left(\frac{r + y}{r}\right)dy \tag{B10}$$

The integral in equation (B10) is the general expression for momentum thickness as defined by equation (A1). Hence,

$$C_F = \left(\frac{q_\delta}{q_\infty}\right)\frac{4\pi r\theta}{S} \tag{B11}$$

It should be noted that the conventional method of calculating average skin friction (relating wall shearing stress to the flow parameters by an elemental control-volume analysis and then performing an integration over the body surface), although more exact, is more difficult to use in pressure gradient flows because it requires an integration of the pressure gradient over the body surface. The approximate method described in this appendix is much simpler to use since it requires measurements only at the body stations where C_F is required.

REFERENCES

1. Gazley, C., Jr.: Theoretical Evaluation of the Turbulent Skin-Friction and Heat Transfer on a Cone in Supersonic Flight. Rept. No. R49A0524, Gen. Elec. Co., Nov. 1949.
2. Bradfield, Walter S.: An Experimental Investigation of the Turbulent Boundary Layer in Supersonic Flow Around Unyawed Cones With Small Heat Transfer and Correlations With Two Dimensional Data. Res. Rept. No. 1, Convair Sci. Res. Lab., Mar. 15, 1958.
3. Van Driest, E. R.: Turbulent Boundary Layer on a Cone in a Supersonic Flow at Zero Angle of Attack. J. Aeron. Sci., vol. 19, no. 1, Jan. 1952, pp. 55-57, 72.
4. Bertram, Mitchel H.: Calculations of Compressible Average Turbulent Skin Friction. NASA TR R-123, 1962.
5. Brown, Clinton E.: Aerodynamics of Bodies at High Speeds. Aerodynamic Components of Aircraft at High Speeds. Vol. VII of High Speed Aerodynamics and Jet Propulsion, sec. B, A. F. Donovan and H. R. Lawrence, eds., Princeton Univ. Press, 1957, pp. 244-280.
6. Reshotko, Eli; and Tucker, Maurice: Approximate Calculation of the Compressible Turbulent Boundary Layer With Heat Transfer and Arbitrary Pressure Gradient. NACA TN 4154, 1957.
7. Wazzan, Ahmed R.; and Ball, W. H.: Body Shape Effects on Skin Friction in Supersonic Flow. AIAA J. (Tech. Notes), vol. 3, no. 9, Sept. 1965, pp. 1770-1772.
8. Sasman, Philip K.; and Cresci, Robert J.: Compressible Turbulent Boundary Layer With Pressure Gradient and Heat Transfer. AIAA J., vol. 4, no. 1, Jan. 1966, pp. 19-25.
9. Englert, Gerald W.: Estimation of Compressible Boundary-Layer Growth Over Insulated Surfaces With Pressure Gradient. NACA TN 4022, 1957.
10. Winter, K. G.; Smith, K. G.; and Rotta, J. C.: Turbulent Boundary-Layer Studies on a Waisted Body of Revolution in Subsonic and Supersonic Flow. Recent Developments in Boundary Layer Research, Pt. II, AGARDograph 97, May 1965, pp. 933-961.
11. Clutter, Darwin W.; and Kaups, Kalle: Wind-Tunnel Investigation of Turbulent Boundary Layers on Axially Symmetric Bodies at Supersonic Speeds. Rept. No. LB31425, (Contract NOw 61-0404-T), Douglas Aircraft Co., Inc., Feb. 6, 1964.
12. McLafferty, George H.; and Barber, Robert E.: The Effect of Adverse Pressure Gradients on the Characteristics of Turbulent Boundary Layers in Supersonic Streams. J. Aerospace Sci., vol. 29, no. 1, Jan. 1962, pp. 1-10, 18.

13. Schaefer, William T., Jr.: Characteristics of Major Active Wind Tunnels at the Langley Research Center. NASA TM X-1130, 1965.

14. Truckenbrodt, E.: A Method of Quadrature for Calculation of the Laminar and Turbulent Boundary Layer in Case of Plane and Rotationally Symmetrical Flow. NACA TM 1379, 1955.

15. Sommer, Simon C.; and Short, Barbara J.: Free-Flight Measurements of Turbulent-Boundary-Layer Skin Friction in the Presence of Severe Aerodynamic Heating at Mach Numbers From 2.8 to 7.0. NACA TN 3391, 1955.

16. Peterson, John B., Jr.: A Comparison of Experimental and Theoretical Results for the Compressible Turbulent-Boundary-Layer Skin Friction With Zero Pressure Gradient. NASA TN D-1795, 1963.

17. Tucker, Maurice: Approximate Calculation of Turbulent Boundary-Layer Development in Compressible Flow. NACA TN 2337, 1951.

18. Adcock, Jerry B.; Peterson, John B., Jr.; and McRee, Donald I.: Experimental Investigation of a Turbulent Boundary Layer at Mach 6, High Reynolds Numbers, and Zero Heat Transfer. NASA TN D-2907, 1965.

19. Ludwieg, H.; and Tillmann, W.: Investigations of the Wall-Shearing Stress in Turbulent Boundary Layers. NACA TM 1285, 1950.

20. Ames Research Staff: Equations, Tables, and Charts for Compressible Flow. NACA Rept. 1135, 1953. (Supersedes NACA TN 1428.)

21. Volluz, R. J.: Handbook of Supersonic Aerodynamics. Section 20 – Wind Tunnel Instrumentation and Operation. NAVORD Rept. 1488 (Vol. 6), Bur. Naval Weapons, Jan. 1961.

22. Kulfan, Robert M.: Turbulent Boundary Layer Flow Past a Smooth Adiabatic Flat Plate. Doc. No. D6-7161, Boeing Airplane Co., May 16, 1961.

23. Sorrells, Russell B., III; Jackson, Mary W.; and Czarnecki, K. R.: Measurement by Wake Momentum Surveys at Mach 1.61 and 2.01 of Turbulent Boundary-Layer Skin Friction on Five Swept Wings. NASA TN D-3764, 1966.

TABLE I.- SPECIFICATIONS OF MODELS

Model	Description	Length, cm	Fineness ratio	Body profile equation (r and x in cm)	
5	Cone	63.6	12.2	$r = 0.041x$	$0 < x < 63.6$
2	Cone	127	12.4	$r = 0.0402x$	$0 < x < 127$
8	Cone—parabolic-arc	63.6	12.2	$r = 0.0768x$ $r = -0.1244 + 0.0976x - 0.000875x^2$	$0 < x < 11.83$ $11.83 < x < 63.6$
4	Cone—parabolic-arc	127	12.2	$r = 0.0769x$ $r = -0.231 + 0.0974x - 0.000436x^2$	$0 < x < 23.7$ $23.7 < x < 127$
3	Cone—parabolic-arc	63.6	6.1	$r = 0.128x$ $r = -0.442 + 0.178x - 0.0014x^2$	$0 < x < 17.78$ $17.78 < x < 63.6$
6	Parabolic arc	63.6	12.2	$r = 0.082x - 0.000646x^2$	$0 < x < 63.6$
7	Parabolic arc	127	12.2	$r = 0.082x - 0.000323x^2$	$0 < x < 127$
1	Parabolic arc (NACA RM-10)	127	12.2	$r = 0.1333x - 0.000854x^2$	$0 < x < 127$

TABLE II.- SUMMARY OF TEST CONDITIONS

Model	x_{tr}, cm	Station	x, cm	Profile number									
				$M_\infty = 1.61$ at p_t, atm, of –					$M_\infty = 2.20$ at p_t, atm, of –				
				0.34	0.68	1.01	1.36	1.70	0.34	0.68	1.01	1.36	1.70
1	1.27	1	70.4	2		1			46		45		44
		2	100.5	5		4	3		49		48		47
		3	116.1	10	9	8	7	6	54	53	52	51	50
		4	121.4	15	14	13	12	11		58	57	56	55
2	2.54	1	74.5						61		60		59
		2	115.3	18		17		16	64		63		62
3	1.27	1	35.7	20		19			66				65
		2	54.5	23		22		21					
		2	58.7						69		68		67
4	1.90	1	71.4	25				24	71				70
		2	117.3	28		27		26	74		73		72
5	2.54	1	35.7	29					77		76		75
		2	58.7	32		31		30	80		79		78
6	1.90	1	35.7						83		82		81
		2	58.7	35		34		33	86		85		84
7	1.90	1	71.4						88				87
		2	117.3	38		37		36	91		90		89
8	1.90	1	35.7	40				39	92				
		2	58.7	43		42		41	95		94		93

TABLE III.- SUMMARY OF RESULTS

$M_\infty = 1.61$

Profile	Model	Station	p_t, atm	R_x	θ, mm	δ^*, mm	δ_u, mm	δ, mm	C_f	C_F	n
1	1	1	1.01	9.614×10^6	0.597	1.532	0.971	8.500	0.002245	0.002643	6.1
2	1	1	.34	3.220	.705	1.802	1.149	9.150	.002698	.003141	6.1
3	1	2	1.36	17.800	.943	2.432	1.519	12.170	.001907	.002324	7.1
4	1	2	1.01	13.760	.939	2.383	1.478	12.120	.002016	.002305	7.1
5	1	2	.34	4.592	1.184	3.017	1.892	14.180	.002376	.002909	6.9
6	1	3	1.70	26.179	1.214	3.055	1.852	15.030	.001710	.002108	6.4
7	1	3	1.36	21.171	1.269	3.215	1.964	15.630	.001764	.002206	6.4
8	1	3	1.01	15.897	1.336	3.404	2.105	16.120	.001848	.002322	6.5
9	1	3	.68	10.623	1.382	3.509	2.168	17.190	.001987	.002414	6.4
10	1	3	.34	5.312	1.470	3.712	2.304	16.250	.002254	.002556	6.3
11	1	4	1.70	27.286	1.400	3.544	2.153	17.580	.001653	.002123	7.0
12	1	4	1.36	22.130	1.436	3.631	2.226	17.610	.001713	.002168	6.8
13	1	4	1.01	16.578	1.466	3.732	2.311	17.640	.001811	.002217	6.7
14	1	4	.68	11.105	1.567	3.986	2.463	17.750	.001935	.002369	6.6
15	1	4	.34	5.552	1.734	4.409	2.740	18.820	.002172	.002641	6.5
16	2	2	1.70	25.705	.680	1.630	1.012	10.980	.002057	.002310	7.3
17	2	2	1.01	15.754	.750	1.796	1.126	10.900	.002227	.002530	6.8
18	2	2	.34	5.277	.869	2.105	1.343	10.710	.002673	.002917	6.6
19	3	1	1.01	4.890	.314	.771	.515	4.390	.002647	.003027	5.8
20	3	1	.34	1.634	.381	.939	.639	5.440	.003197	.003648	5.8
21	3	2	1.70	12.278	.470	1.176	.762	7.110	.002169	.002573	5.7
22	3	2	1.01	7.467	.505	1.251	.826	6.950	.002375	.002674	5.7
23	3	2	.34	2.495	.622	1.578	1.069	7.560	.002839	.003259	5.2
24	4	1	1.70	15.911	.559	1.573	1.016	8.960	.002113	.002969	6.1
25	4	1	.34	3.266	.720	1.766	1.178	8.650	.002884	.003279	6.0
26	4	2	1.70	26.489	.942	2.224	1.412	12.870	.001897	.002135	6.8
27	4	2	1.01	16.060	.961	2.305	1.446	13.380	.002080	.002274	6.8
28	4	2	.34	5.366	1.177	2.916	1.876	13.670	.002456	.002788	5.7
29	5	1	.34	1.669	.317	.781	.495	4.510	.003255	.003546	6.6
30	5	2	1.70	13.285	.339	.833	.521	5.900	.002358	.002296	6.4
31	5	2	1.01	8.013	.388	.956	.604	6.020	.002525	.002619	6.7
32	5	2	.34	2.741	.444	1.091	.690	5.820	.003040	.002976	6.7
33	6	2	1.70	13.131	.462	1.145	.703	7.470	.002154	.002421	7.3
34	6	2	1.01	8.013	.467	1.144	.701	7.160	.002377	.002448	7.2
35	6	2	.34	2.665	.573	1.413	.867	7.230	.002817	.003038	7.1
36	7	2	1.70	26.103	.837	2.067	1.262	12.990	.001920	.002219	7.6
37	7	2	1.01	16.060	.906	2.253	1.389	13.710	.002077	.002403	7.1
38	7	2	.34	5.366	1.068	2.660	1.655	13.350	.002471	.002832	6.8
39	8	1	1.70	7.987	.295	.734	.471	4.920	.002386	.002850	6.1
40	8	1	.34	1.621	.385	.963	.639	4.370	.003151	.003697	5.9
41	8	2	1.70	13.170	.507	1.261	.794	7.500	.002115	.002468	6.3
42	8	2	1.01	8.013	.526	1.292	.820	7.470	.002334	.002515	6.1
43	8	2	.34	2.684	.646	1.601	1.037	7.570	.002775	.003097	6.0

TABLE III.- SUMMARY OF RESULTS – Concluded

$M_\infty = 2.20$

Profile	Model	Station	p_t, atm	R_x	θ, mm	δ^*, mm	δ_u, mm	δ, mm	C_f	C_F	n
44	1	1	1.70	12.052×10^6	0.500	1.756	0.867	8.590	0.001897	0.002192	7.1
45	1	1	1.01	7.636	.502	1.748	.849	7.870	.002043	.002207	7.2
46	1	1	.34	2.553	.703	2.460	1.273	11.480	.002466	.003084	6.1
47	1	2	1.70	17.307	.851	3.014	1.459	13.460	.001642	.002052	7.0
48	1	2	1.01	10.903	.882	3.119	1.530	12.170	.001803	.002119	6.8
49	1	2	.34	3.678	1.146	3.969	2.029	15.660	.002190	.002768	6.5
50	1	3	1.70	19.956	1.069	3.836	1.814	16.450	.001520	.001802	7.3
51	1	3	1.36	16.466	1.094	3.899	1.860	15.320	.001585	.001834	7.1
52	1	3	1.01	12.596	1.185	4.252	2.042	19.310	.001630	.002009	7.0
53	1	3	.68	8.385	1.289	4.632	2.214	18.660	.001738	.002175	6.9
54	1	3	.34	4.249	1.611	5.580	2.780	21.350	.002000	.002736	6.8
55	1	4	1.70	21.218	1.201	4.251	1.993	22.110	.001484	.001737	7.1
56	1	4	1.36	17.173	1.251	4.449	2.111	21.350	.001542	.001838	7.4
57	1	4	1.01	13.127	1.353	4.841	2.297	29.110	.001584	.002008	7.1
58	1	4	.68	8.765	1.453	5.115	2.510	19.250	.001737	.002120	6.9
59	2	1	1.70	13.052	.455	1.531	.749	9.610	.002006	.002467	7.5
60	2	1	1.01	8.060	.476	1.595	.784	10.230	.002199	.002586	7.5
61	2	1	.34	2.800	.568	1.903	.972	10.380	.002691	.003072	7.5
62	2	2	1.70	20.315	.617	2.061	.996	12.180	.001908	.002168	7.8
63	2	2	1.01	12.438	.655	2.172	1.055	13.660	.002088	.002296	7.5
64	2	2	.34	4.297	.758	2.490	1.245	12.620	.002550	.002621	7.2
65	3	1	1.70	6.138	.245	.837	.435	5.320	.002331	.002650	7.2
66	3	1	.34	1.319	.298	.982	.515	5.240	.003249	.003205	8.0
67	3	2	1.70	10.160	.470	1.616	.864	7.690	.002042	.002516	6.2
68	3	2	1.01	6.326	.515	1.820	.952	10.050	.001949	.002803	6.3
69	3	2	.34	2.166	.562	1.934	1.023	8.330	.002676	.003000	6.4
70	4	1	1.70	12.365	.464	1.591	.788	9.410	.001975	.002328	7.5
71	4	1	.34	2.636	.591	2.004	1.036	8.500	.002658	.002970	7.4
72	4	2	1.70	20.430	.805	2.807	1.355	13.740	.001701	.001997	7.6
73	4	2	1.01	12.649	.862	3.008	1.471	13.860	.001844	.002153	7.4
74	4	2	.34	4.370	.979	3.304	1.695	13.730	.002355	.002407	6.8
75	5	1	1.70	6.313	.234	.822	.409	4.100	.002223	.002643	7.5
76	5	1	1.01	3.851	.253	.865	.431	4.850	.002473	.002895	7.4
77	5	1	.34	1.284	.288	1.000	.508	4.840	.003054	.003332	7.4
78	5	2	1.70	10.409	.317	1.064	.513	8.480	.002167	.002167	7.5
79	5	2	1.01	6.326	.371	1.266	.630	7.960	.002302	.002545	7.5
80	5	2	.34	2.109	.430	1.474	.738	6.900	.002807	.002975	8.0
81	6	1	1.70	6.232	.243	.842	.418	4.450	.002233	.002450	7.4
82	6	1	1.01	3.746	.286	.999	.507	4.980	.002391	.002890	7.2
83	6	1	.34	1.284	.318	1.114	.560	5.840	.002991	.003233	8.1
84	6	2	1.70	10.237	.409	1.423	.694	7.540	.001970	.002135	6.8
85	6	2	1.01	6.326	.471	1.653	.816	9.460	.002089	.002492	6.6
86	6	2	.34	2.109	.525	1.840	.897	8.620	.002552	.002787	7.1
87	7	1	1.70	12.435	.479	1.668	.826	8.350	.001933	.002430	6.7
88	7	1	.34	2.660	.579	1.896	.945	10.470	.002682	.003033	7.6
89	7	2	1.70	20.392	.746	2.608	1.238	13.940	.001725	.001976	7.3
90	7	2	1.01	12.649	.817	2.846	1.367	13.330	.001864	.002187	7.4
91	7	2	.34	4.370	.945	3.148	1.532	14.470	.002348	.002610	7.5
92	8	1	.34	1.283	.308	1.082	.550	5.390	.003045	.003110	7.2
93	8	2	1.70	10.467	.461	1.643	.822	8.180	.001886	.002275	6.6
94	8	2	1.01	6.326	.502	1.780	.892	9.070	.002056	.002499	6.6
95	8	2	.34	2.109	.569	2.041	1.020	8.260	.002491	.002847	7.1

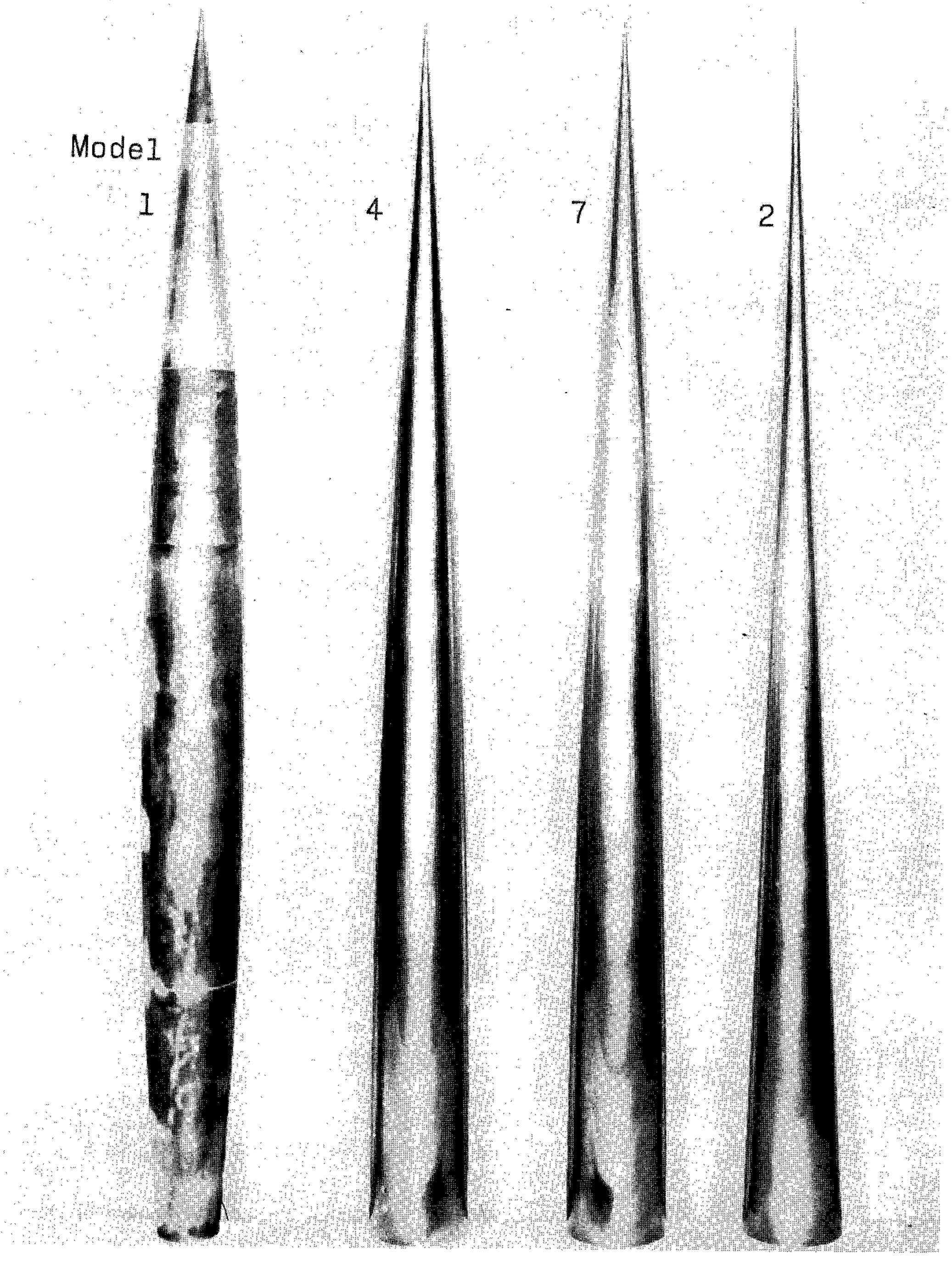

(a) 127-cm-long models. L-65-6987.1

Figure 1.- Photograph of models.

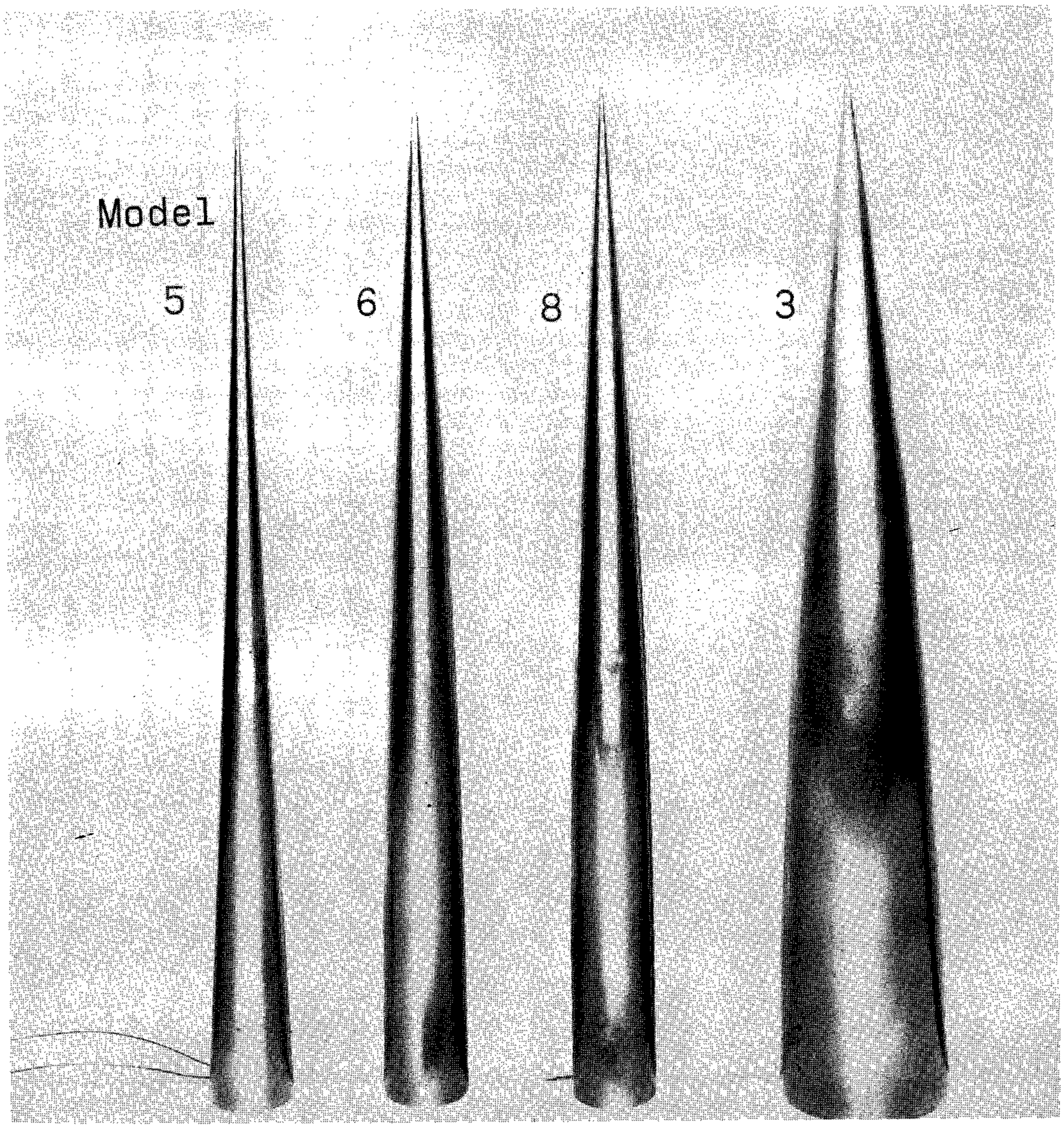

(b) 63.3-cm-long models.

L-65-6988.1

Figure 1.- Concluded.

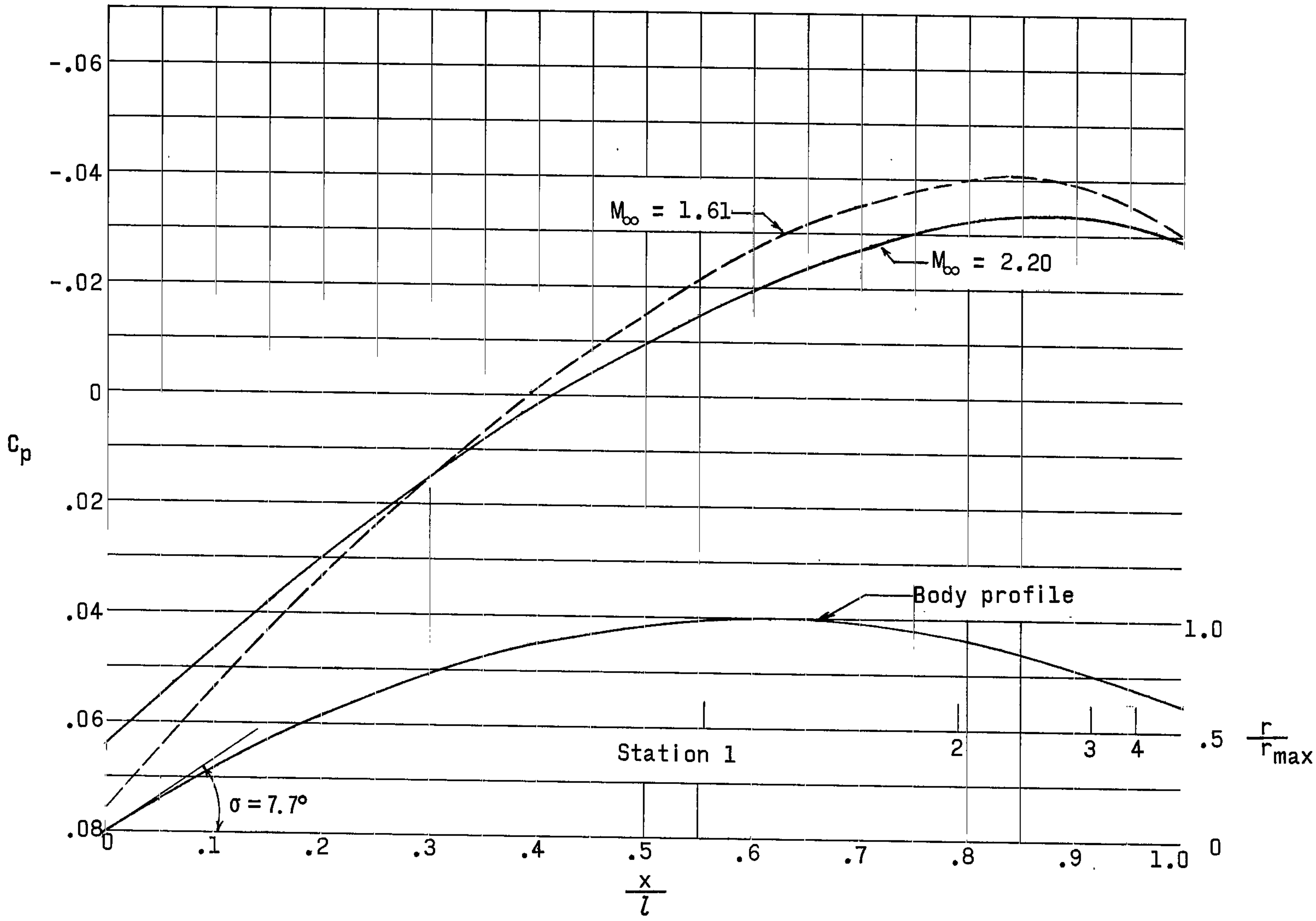

(a) Model 1 (RM-10).

Figure 2.- Model profiles and theoretical pressure distributions.

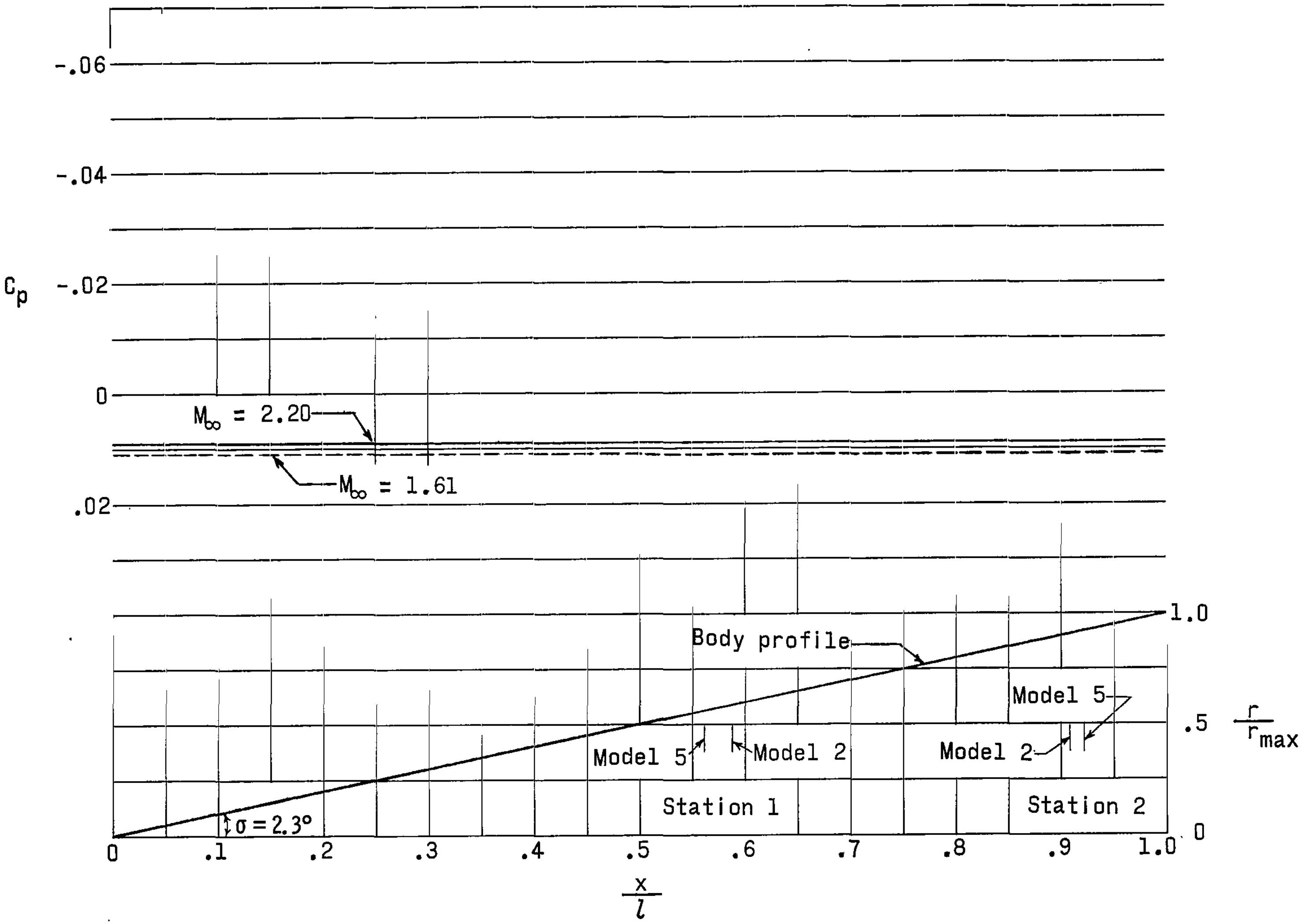

(b) Models 2 and 5 (slender cones).

Figure 2.- Continued.

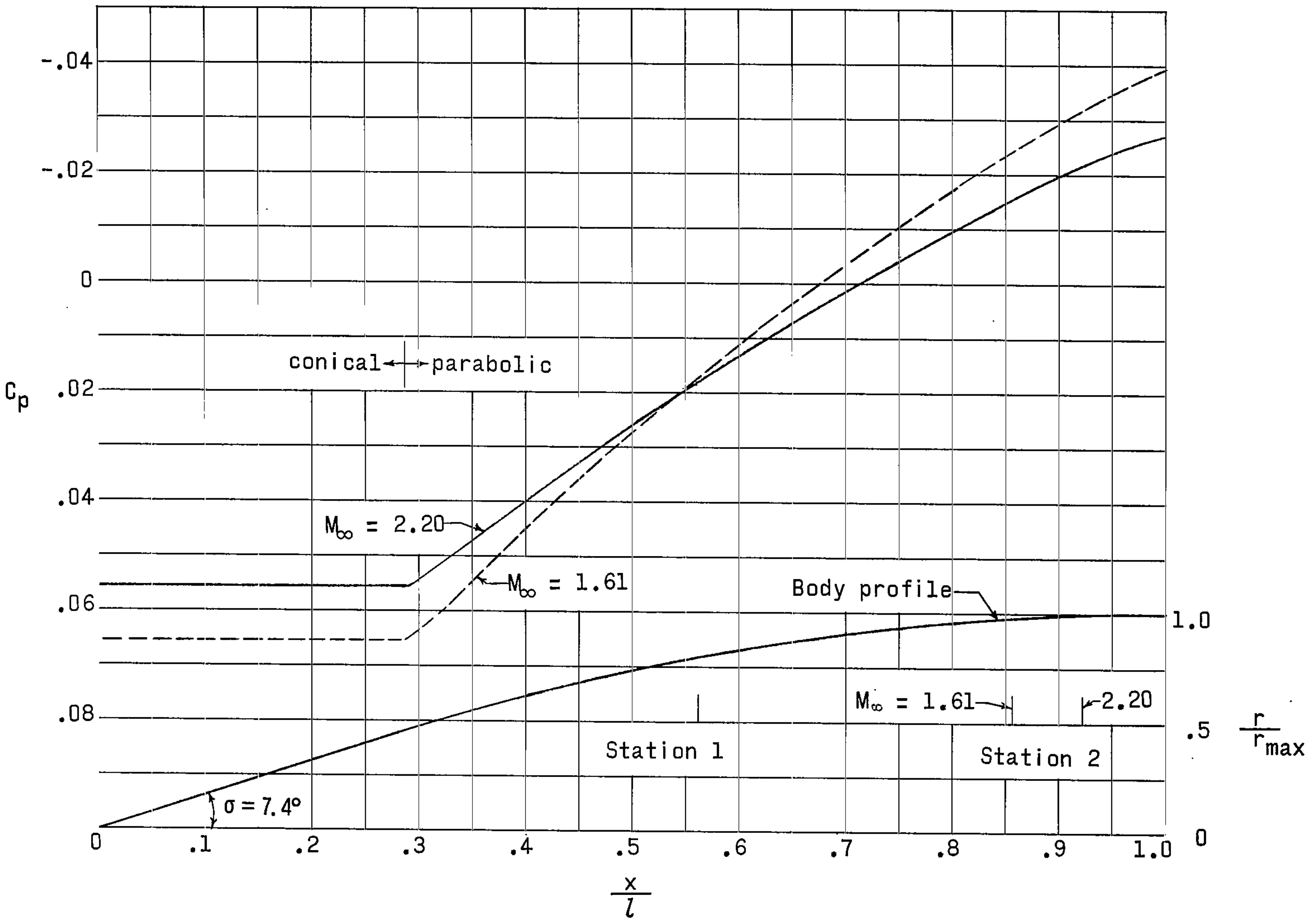

(c) Model 3 (cone-parabolic arc).

Figure 2.- Continued.

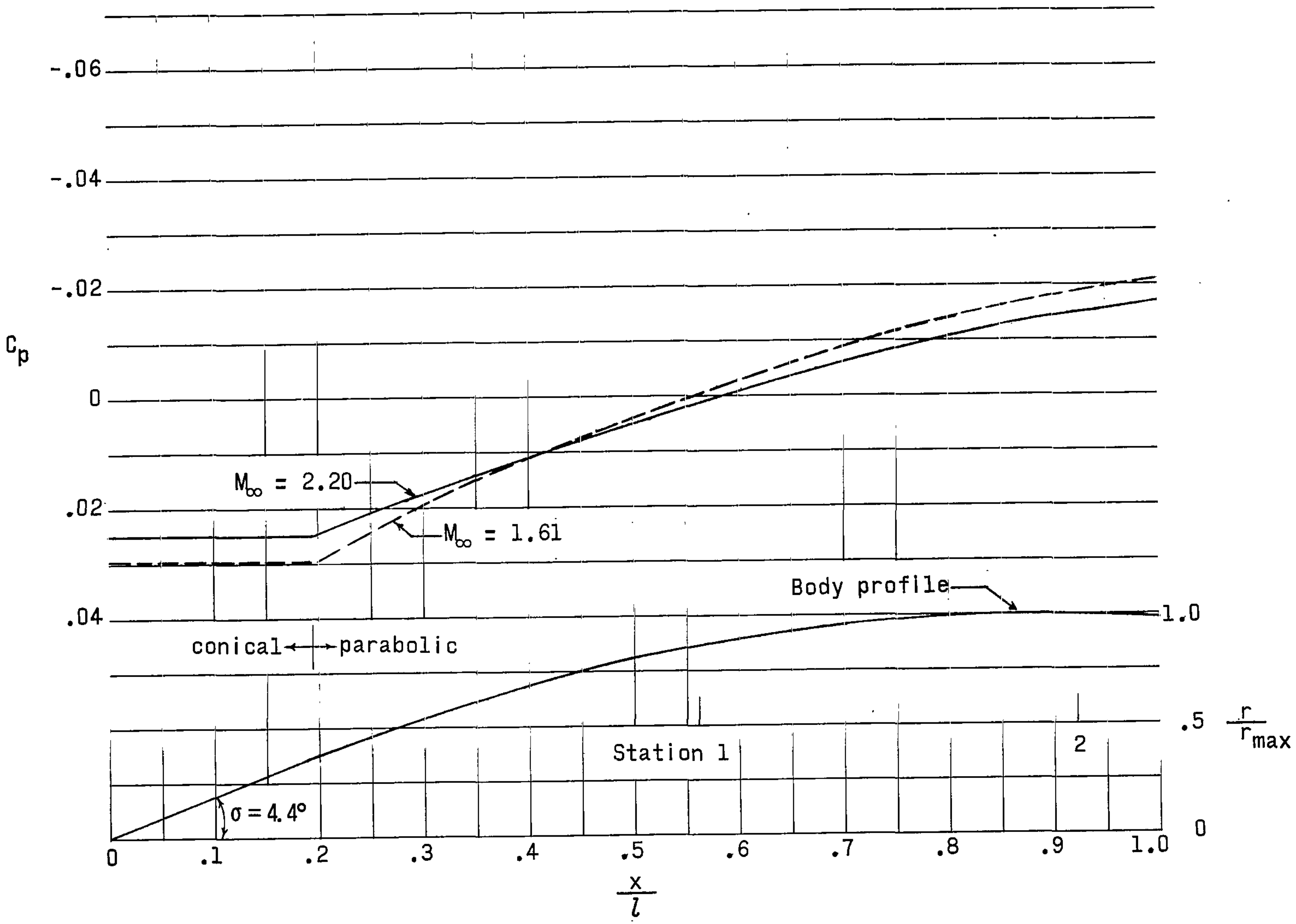

(d) Models 4 and 8 (cone-parabolic arc).

Figure 2.- Continued.

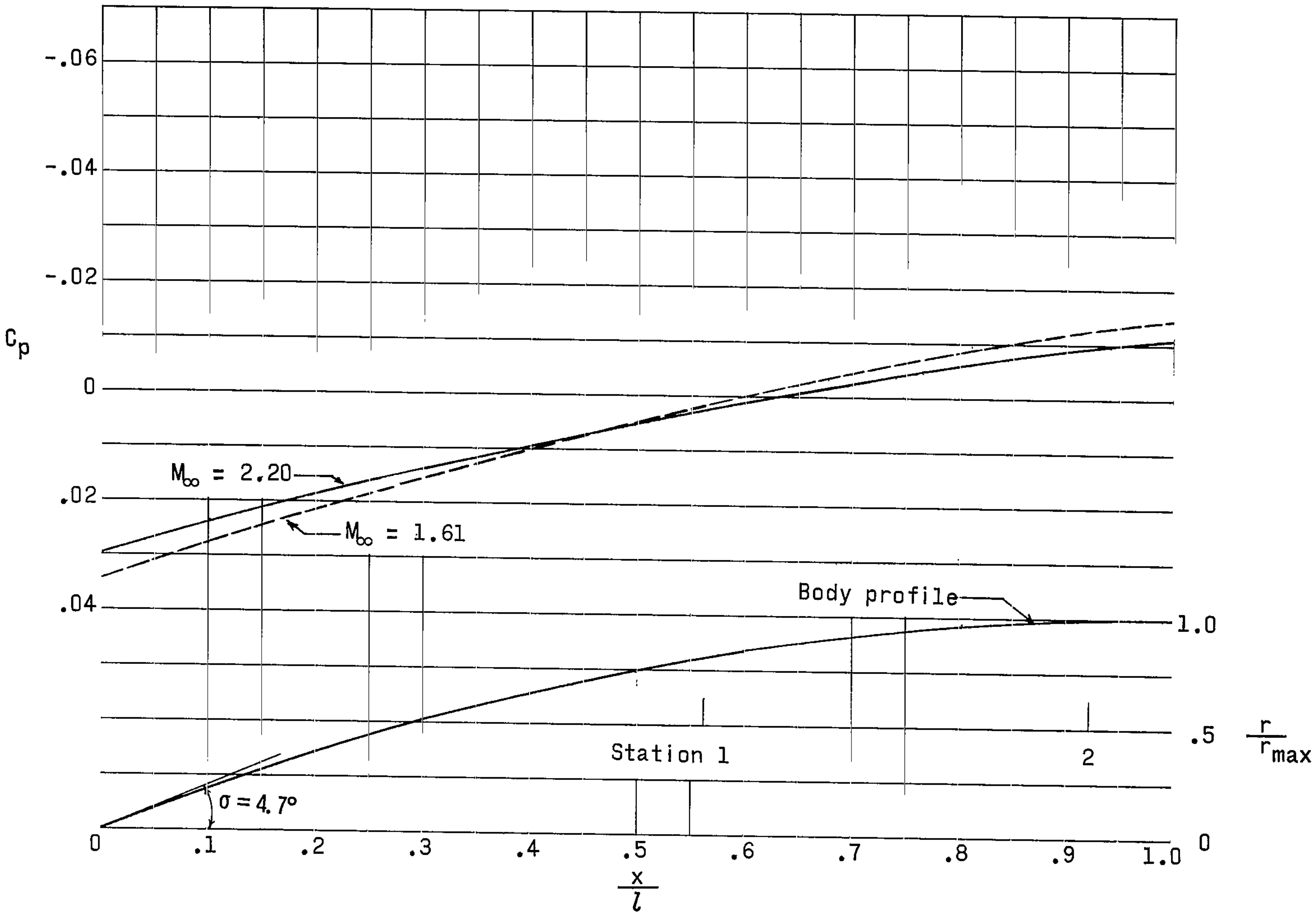

(e) Models 6 and 7 (parabolic arc).

Figure 2.- Concluded.

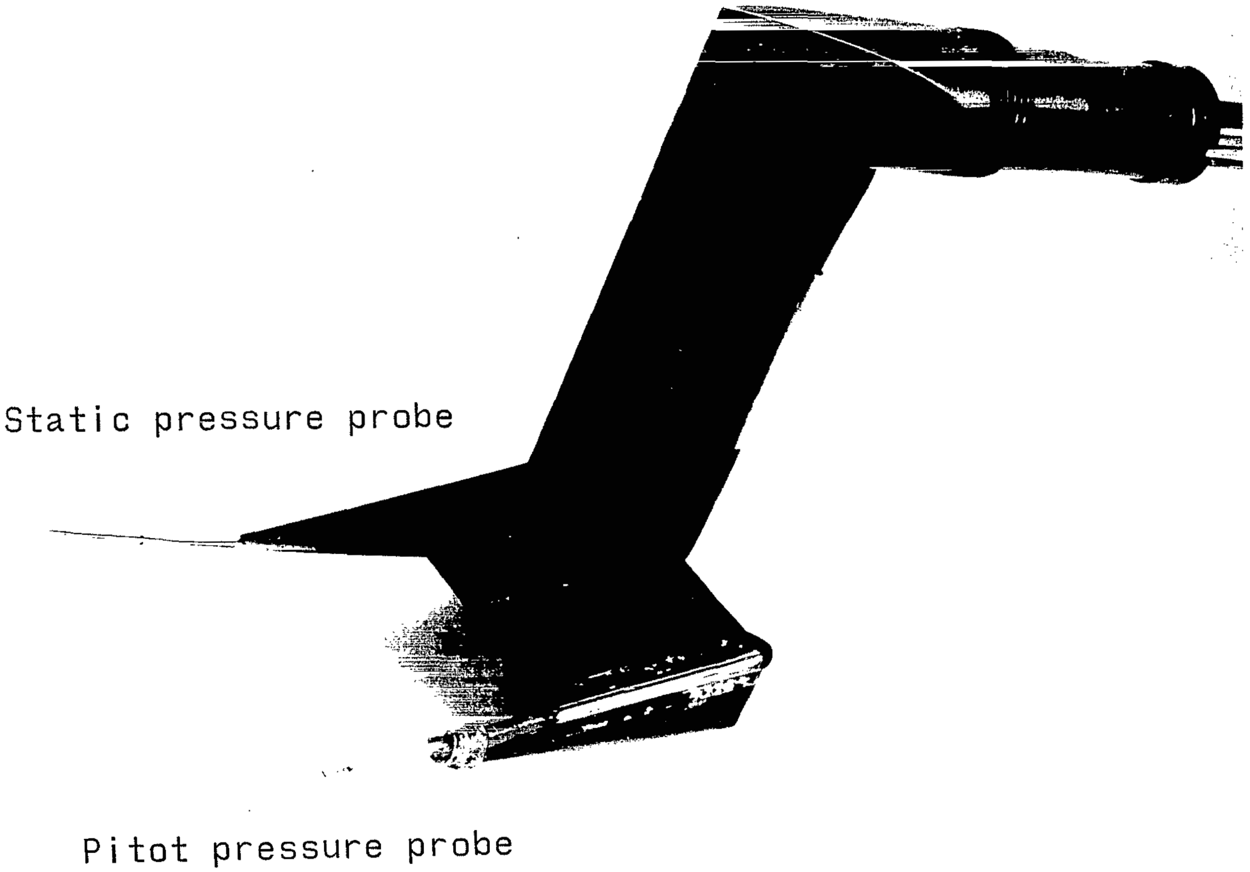

Figure 3.- Boundary-layer probes.

L-65-6986.1

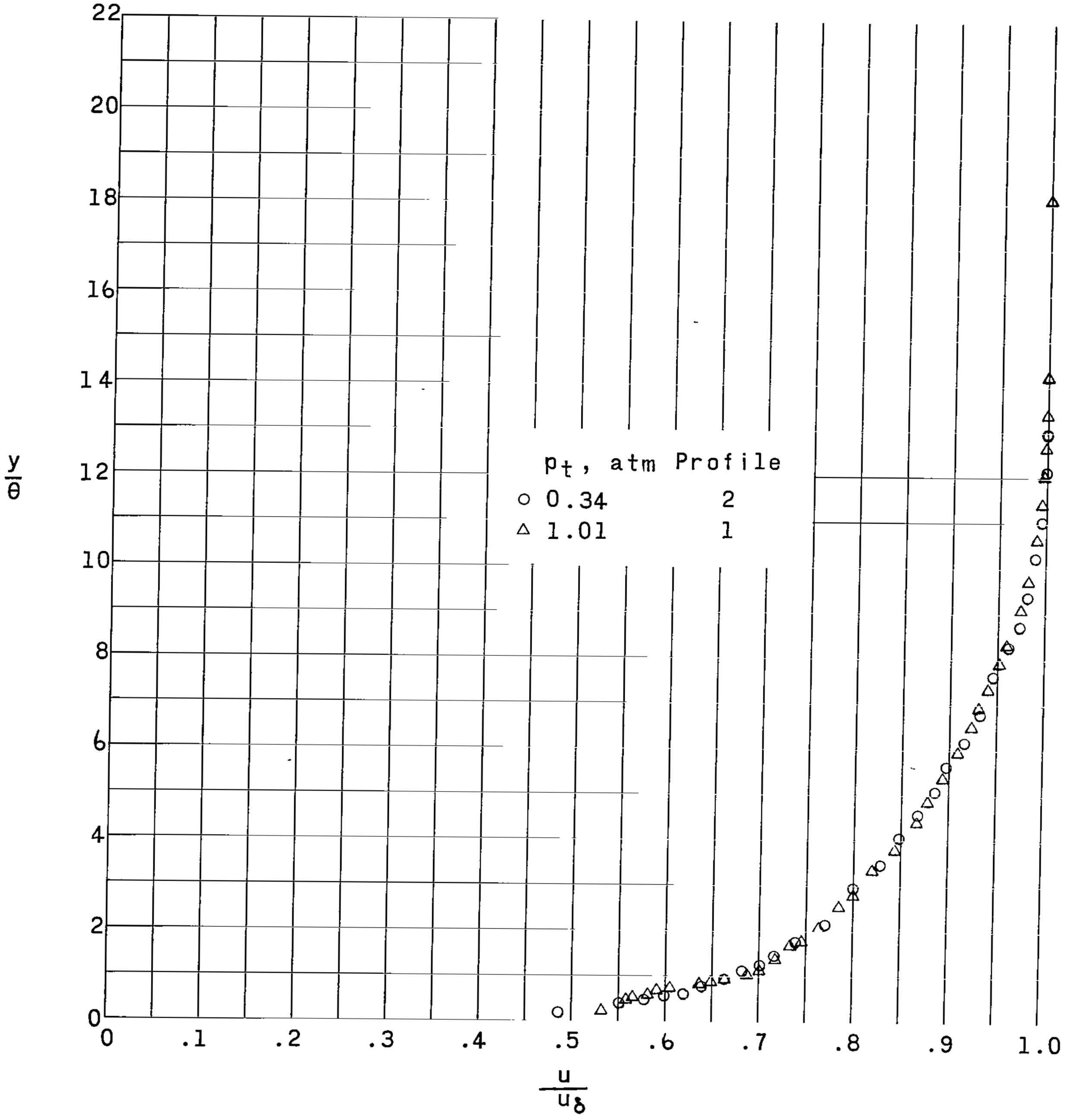

(a) Model 1, station 1.

Figure 4.- Velocity profiles at a free-stream Mach number of 1.61.

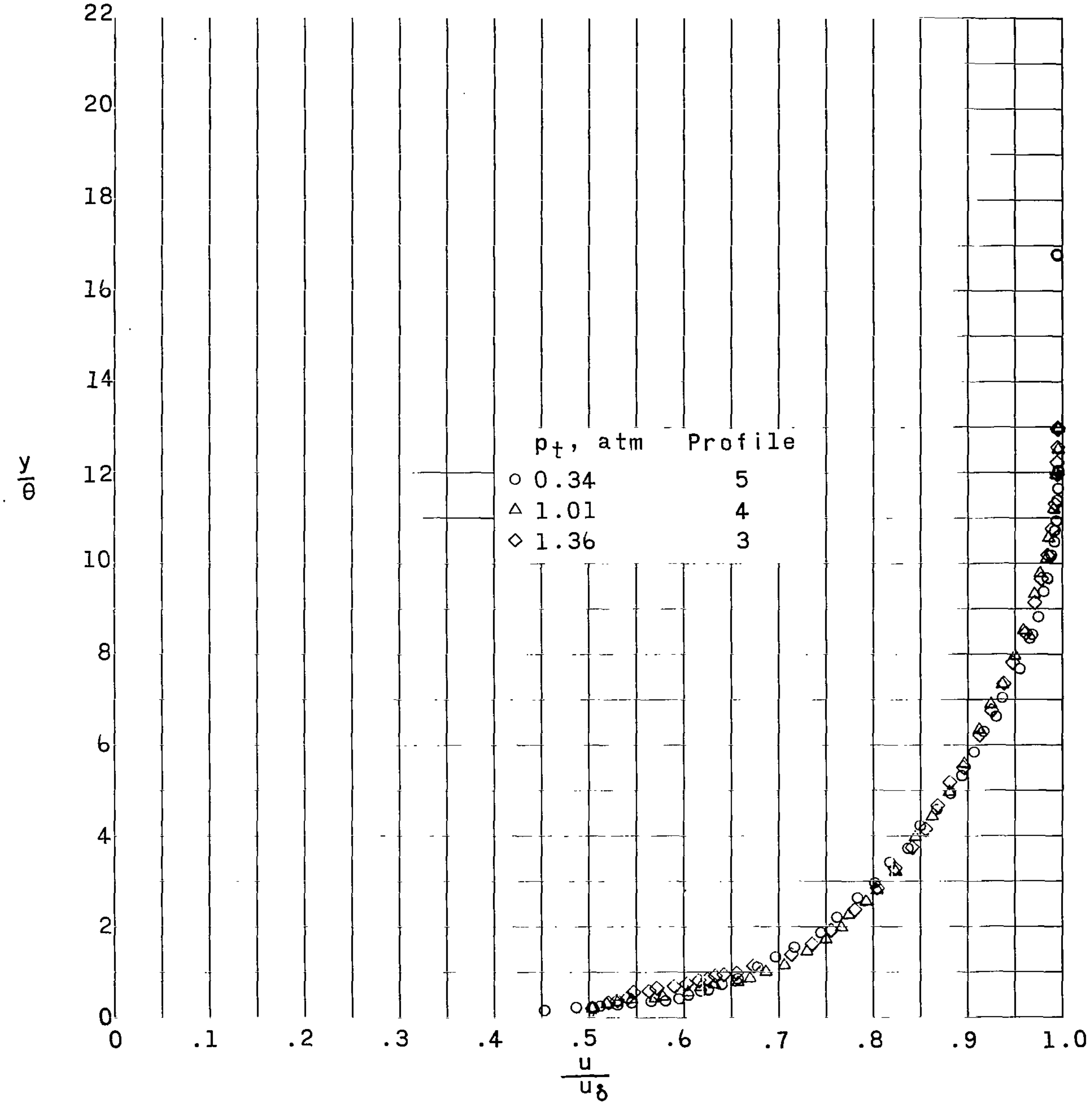

(b) Model 1, station 2.

Figure 4.- Continued.

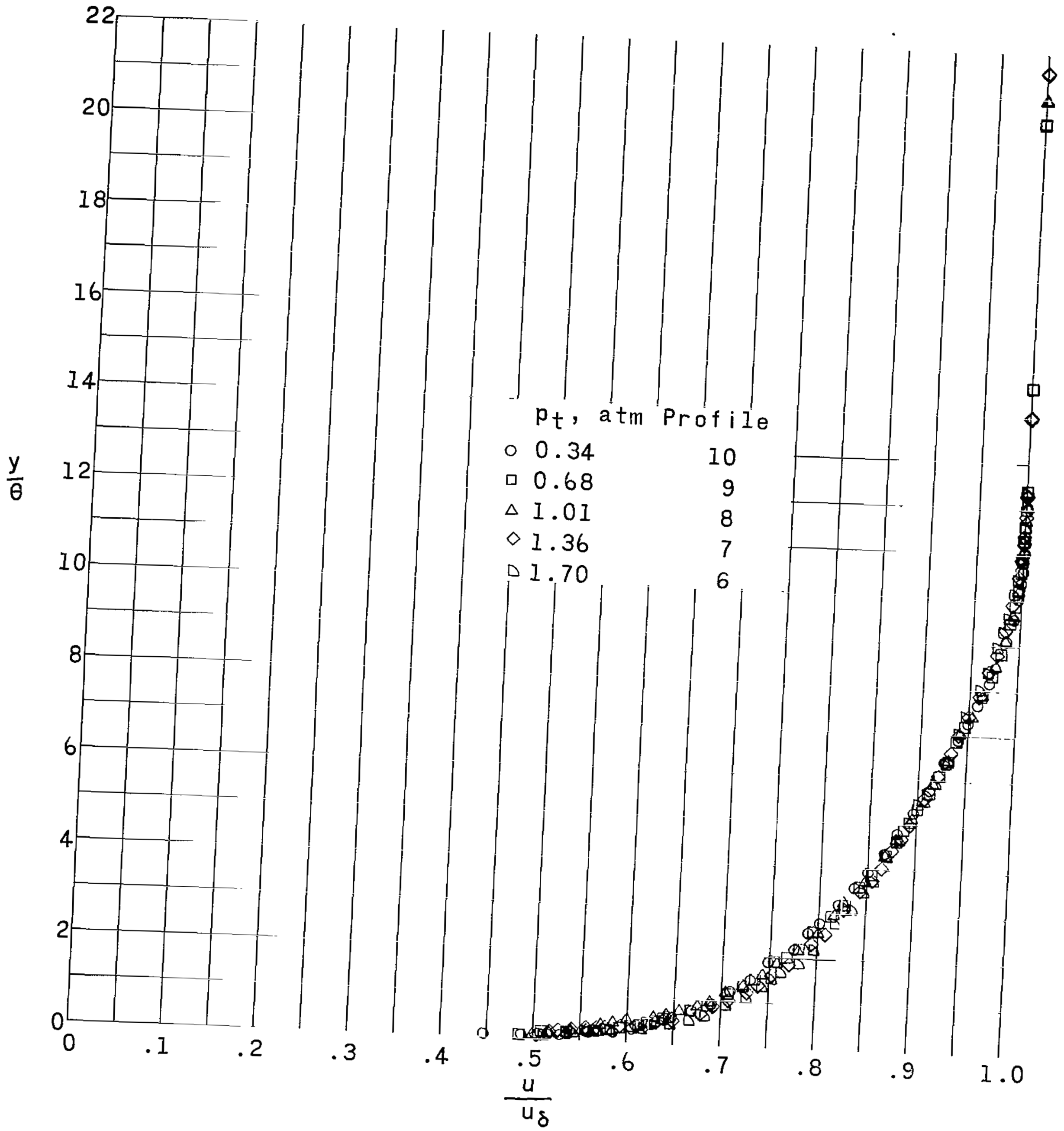

(c) Model 1, station 3.

Figure 4.- Continued.

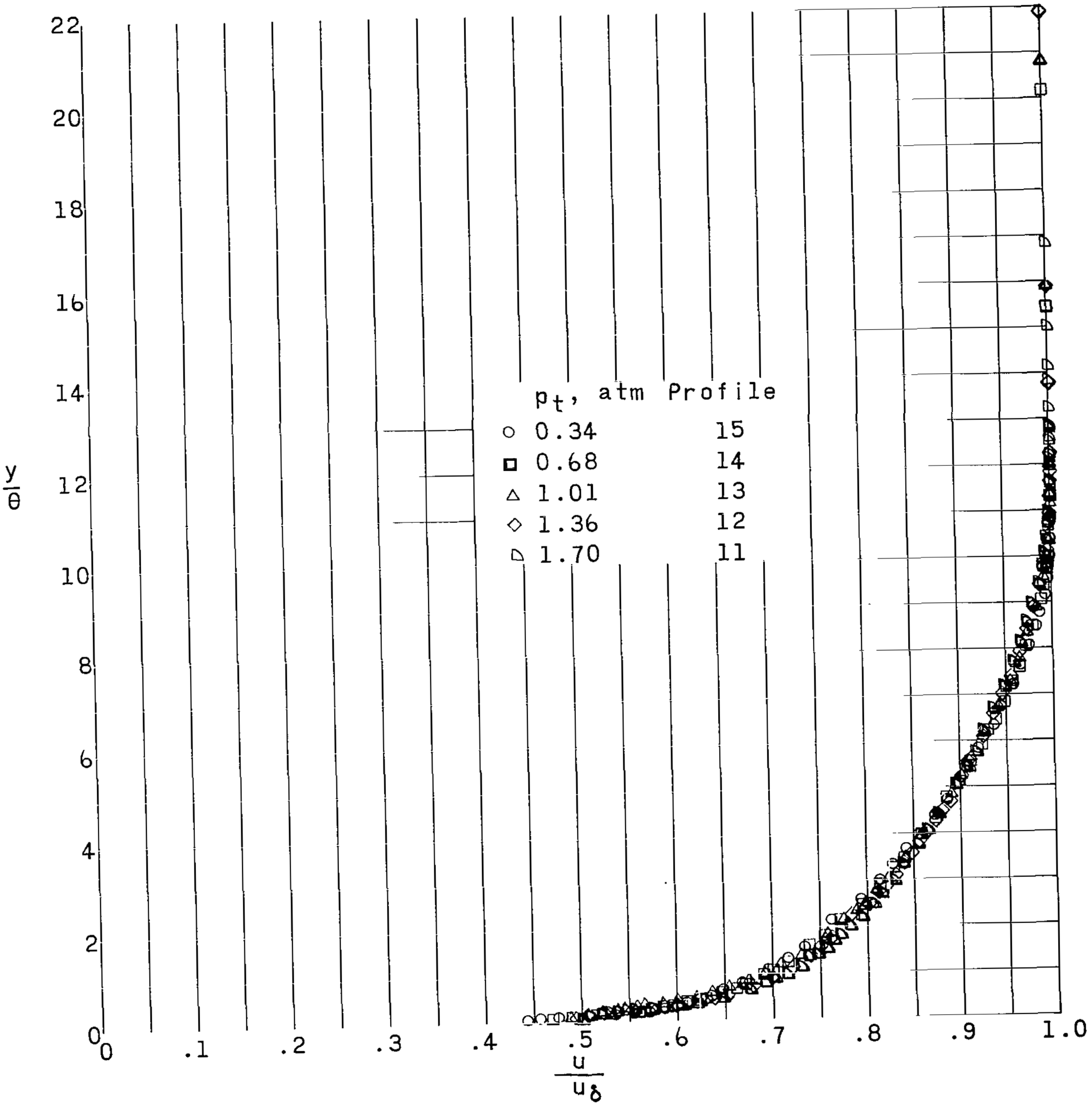

(d) Model 1, station 4.

Figure 4.- Continued.

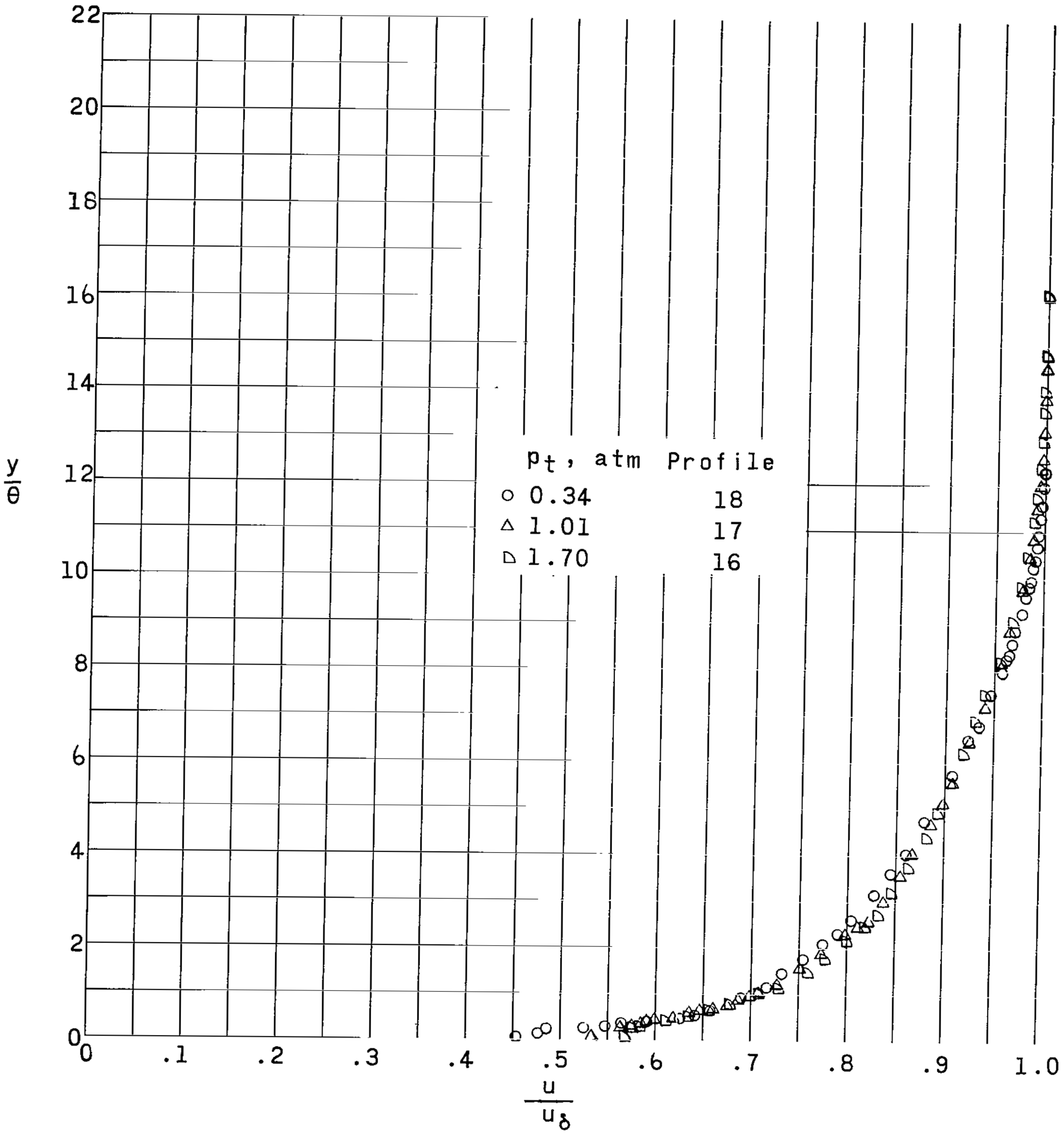

(e) Model 2, station 2.

Figure 4.- Continued.

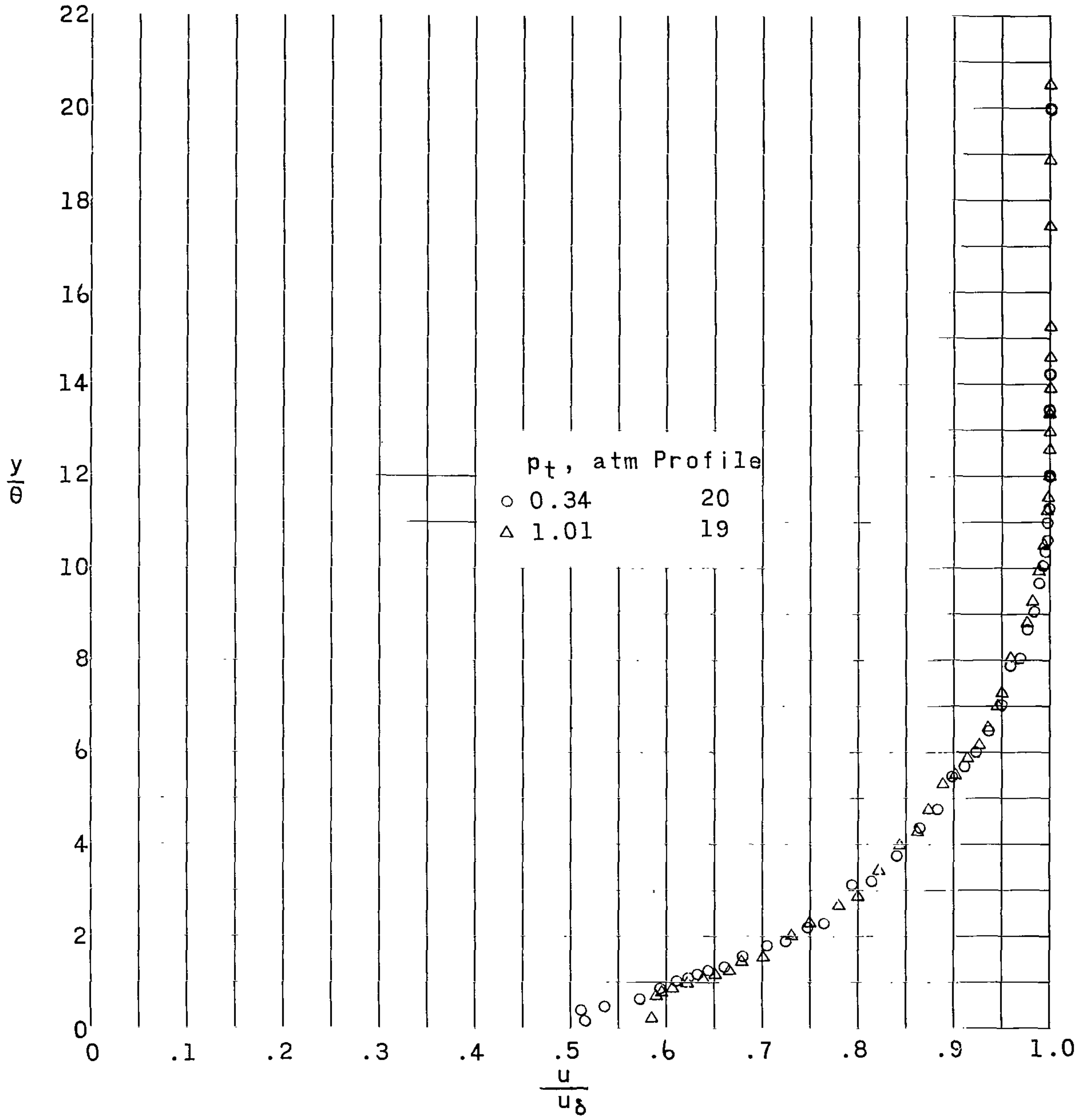

(f) Model 3, station 1.

Figure 4.- Continued.

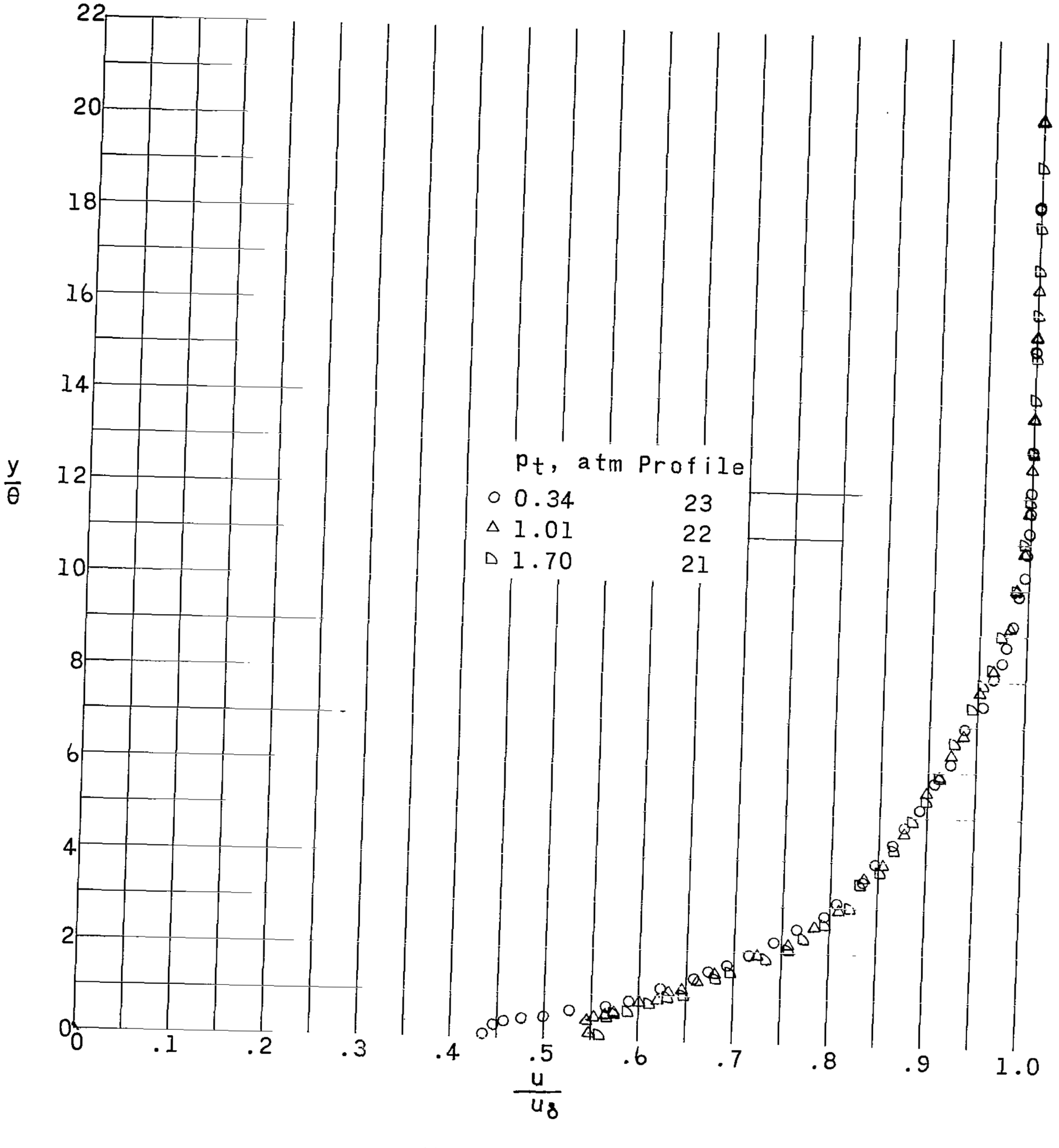

(g) Model 3, station 2.

Figure 4.- Continued.

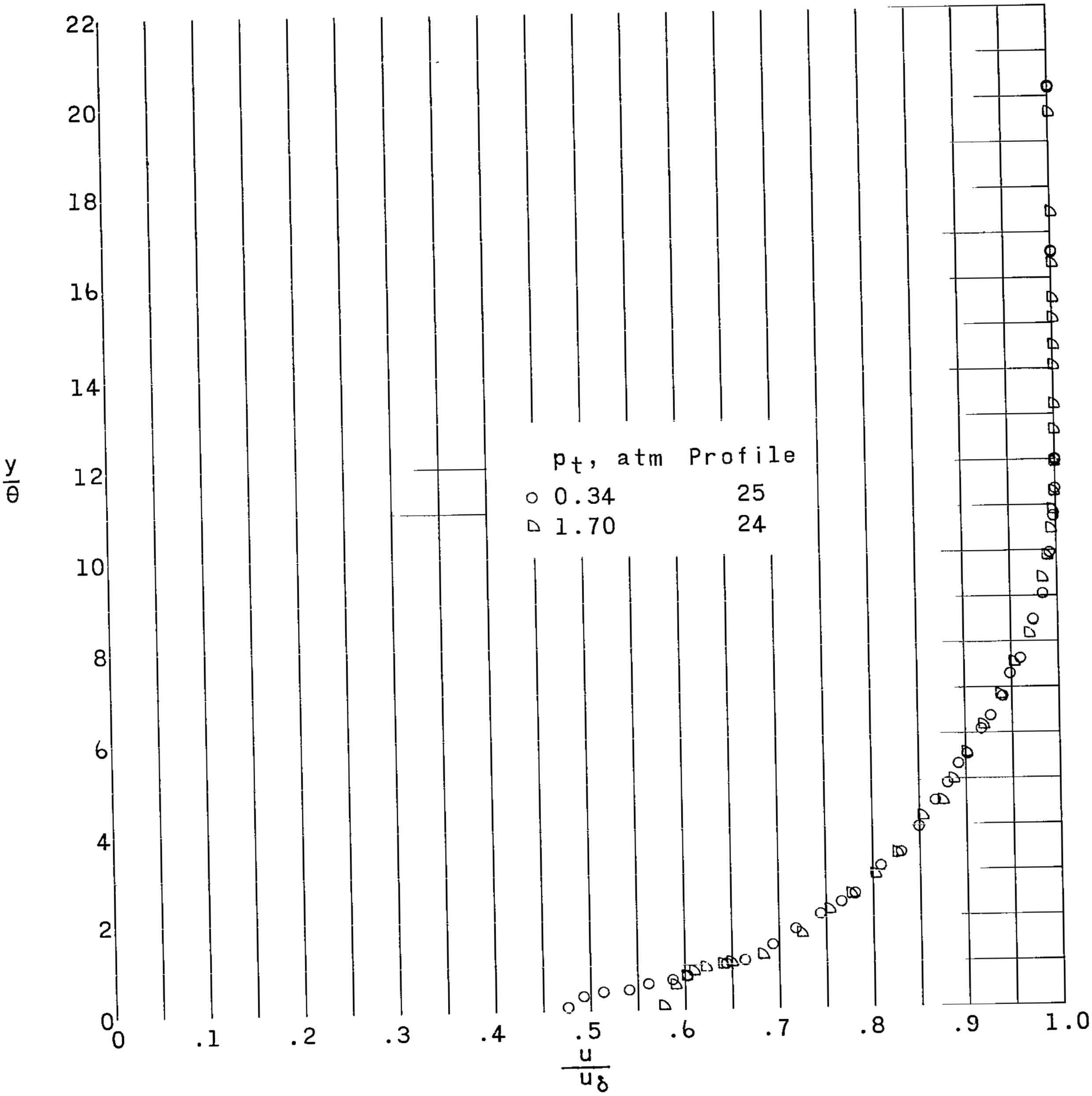

(h) Model 4, station 1.

Figure 4.- Continued.

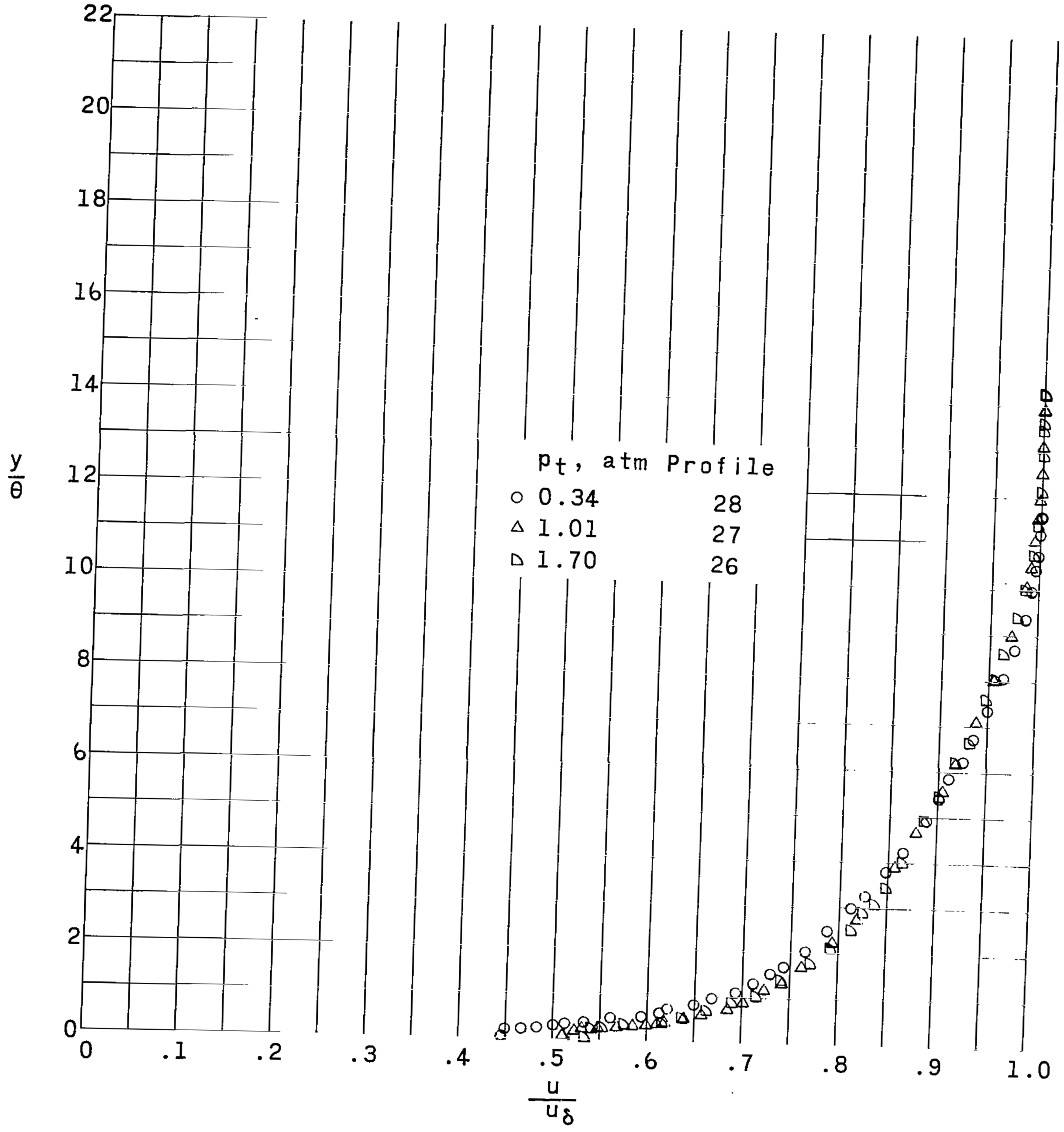

(i) Model 4, station 2.

Figure 4.- Continued.

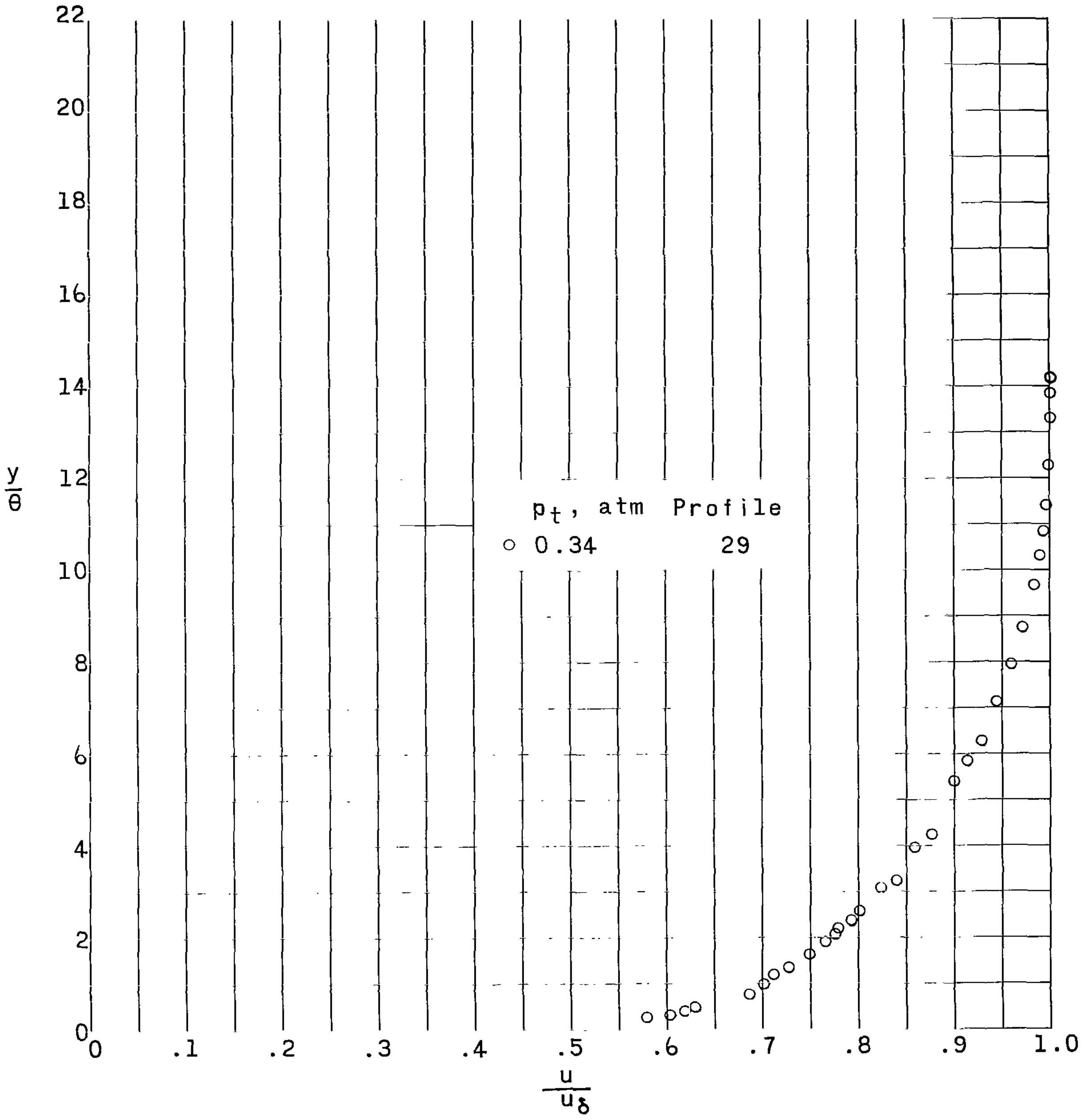

(j) Model 5, station 1.

Figure 4.- Continued.

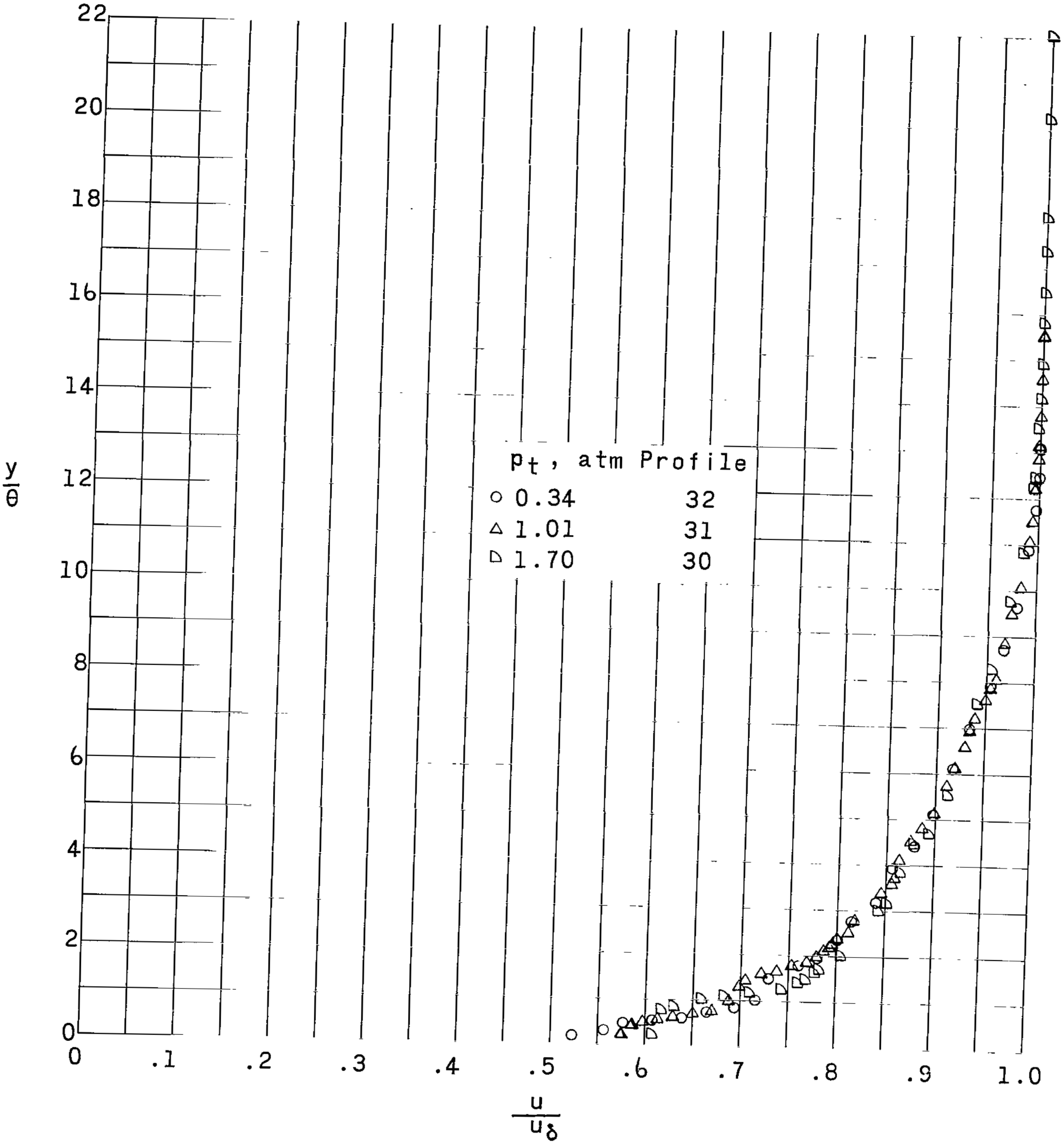

(k) Model 5, station 2.

Figure 4.- Continued.

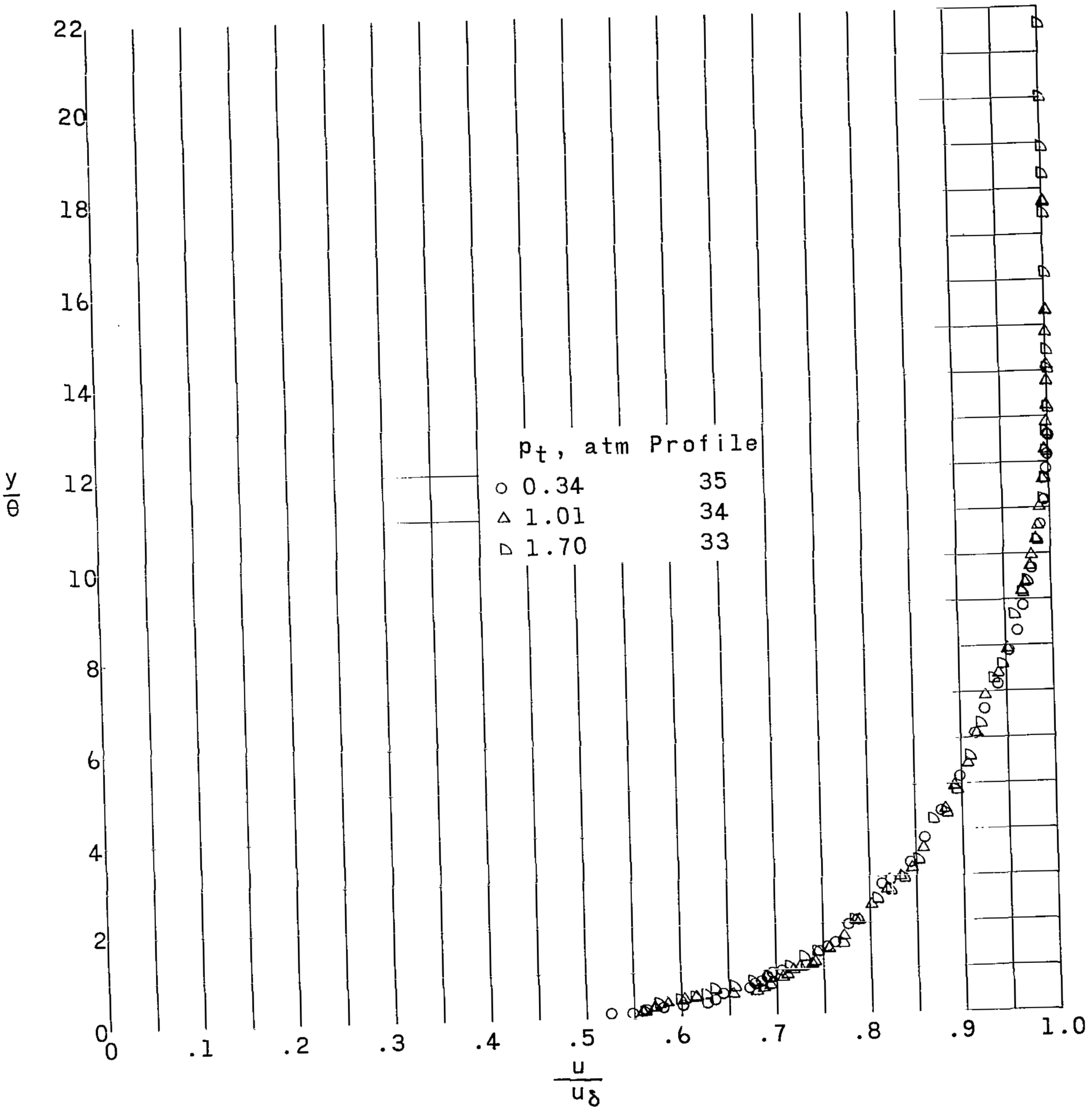

(l) Model 6, station 2.

Figure 4.- Continued.

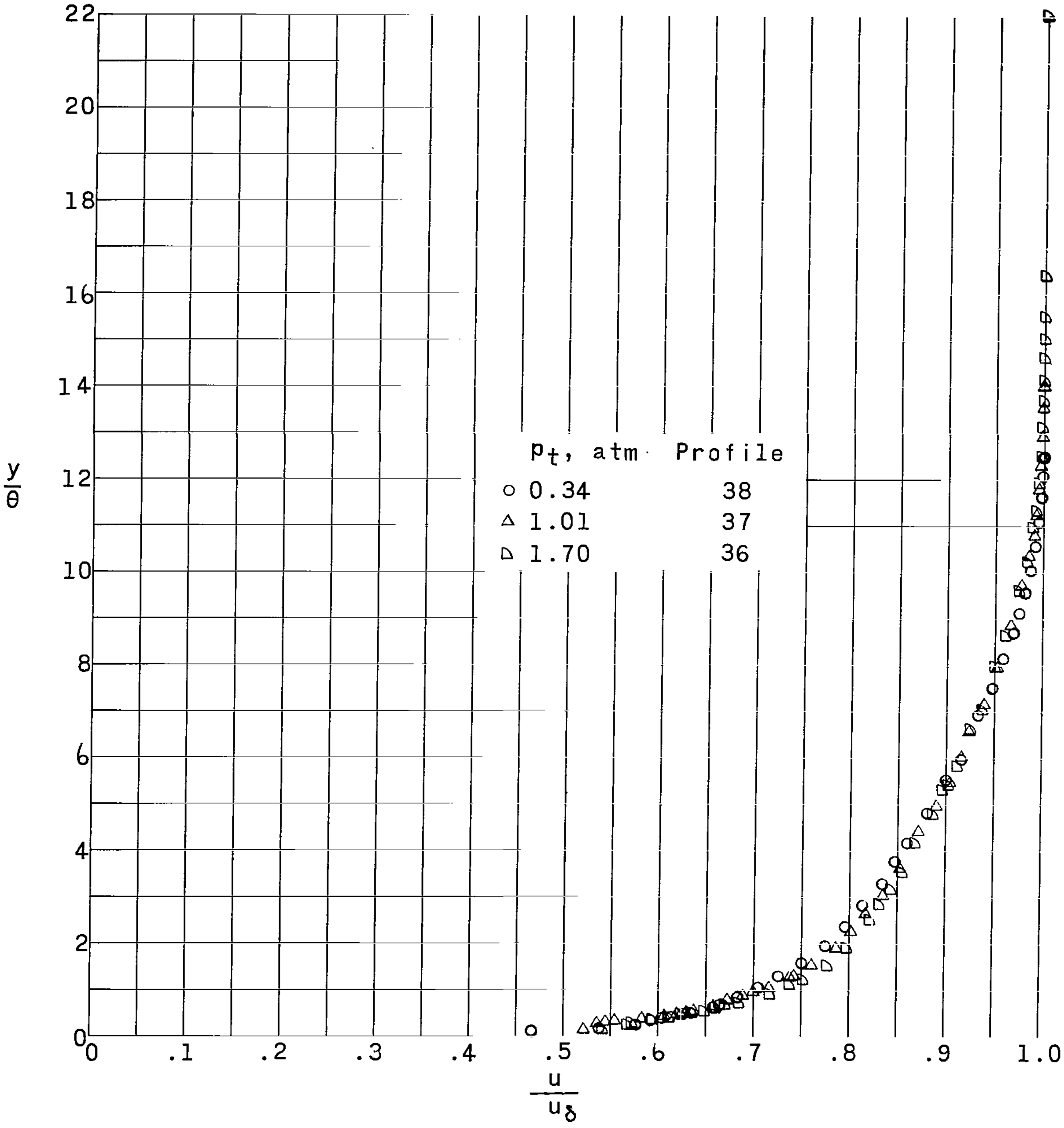

(m) Model 7, station 2.

Figure 4.- Continued.

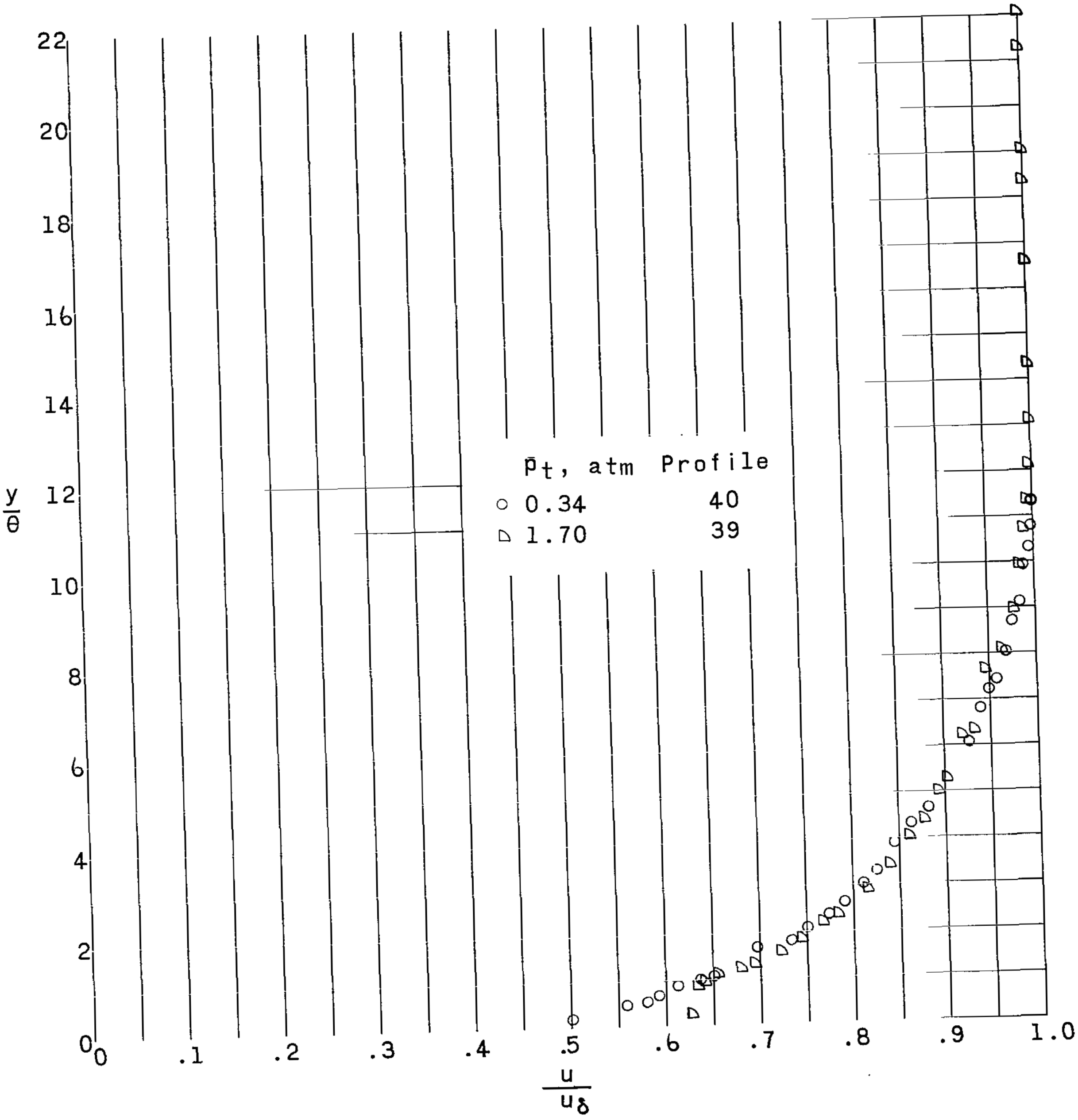

(n) Model 8, station 1.

Figure 4.- Continued.

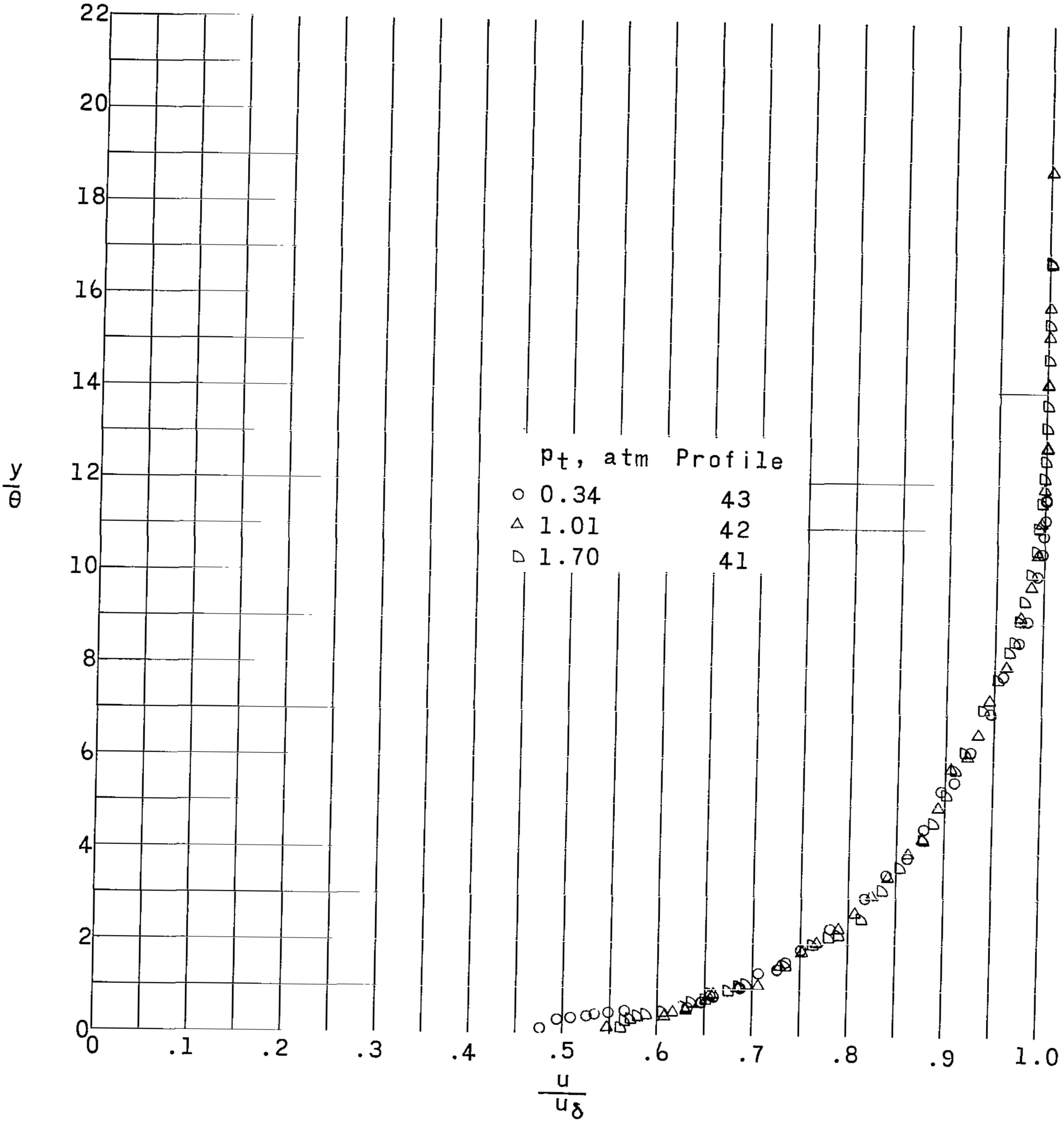

(o) Model 8, station 2.

Figure 4.- Concluded.

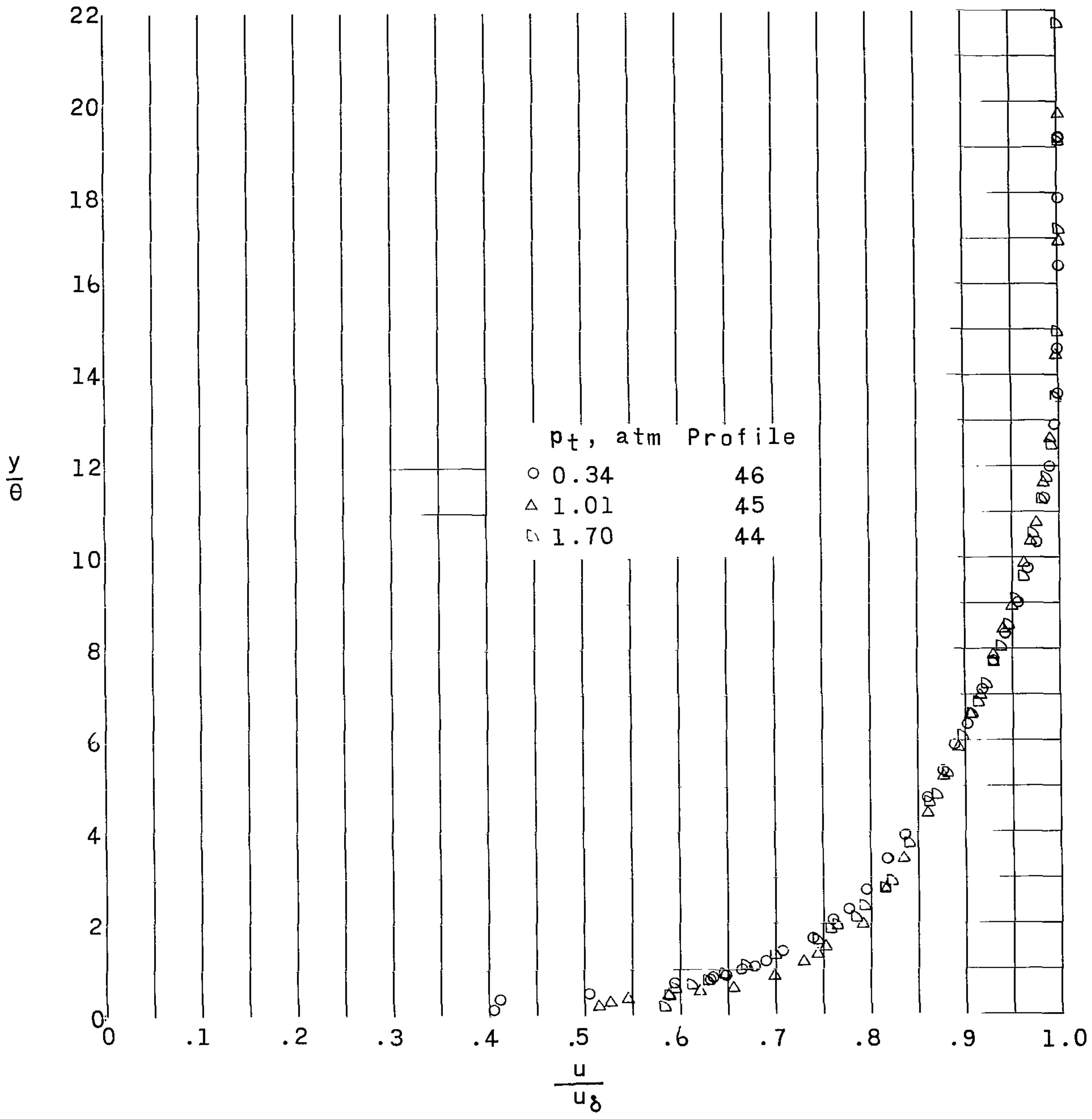

(a) Model 1, station 1.

Figure 5.- Velocity profiles at a free-stream Mach number of 2.20.

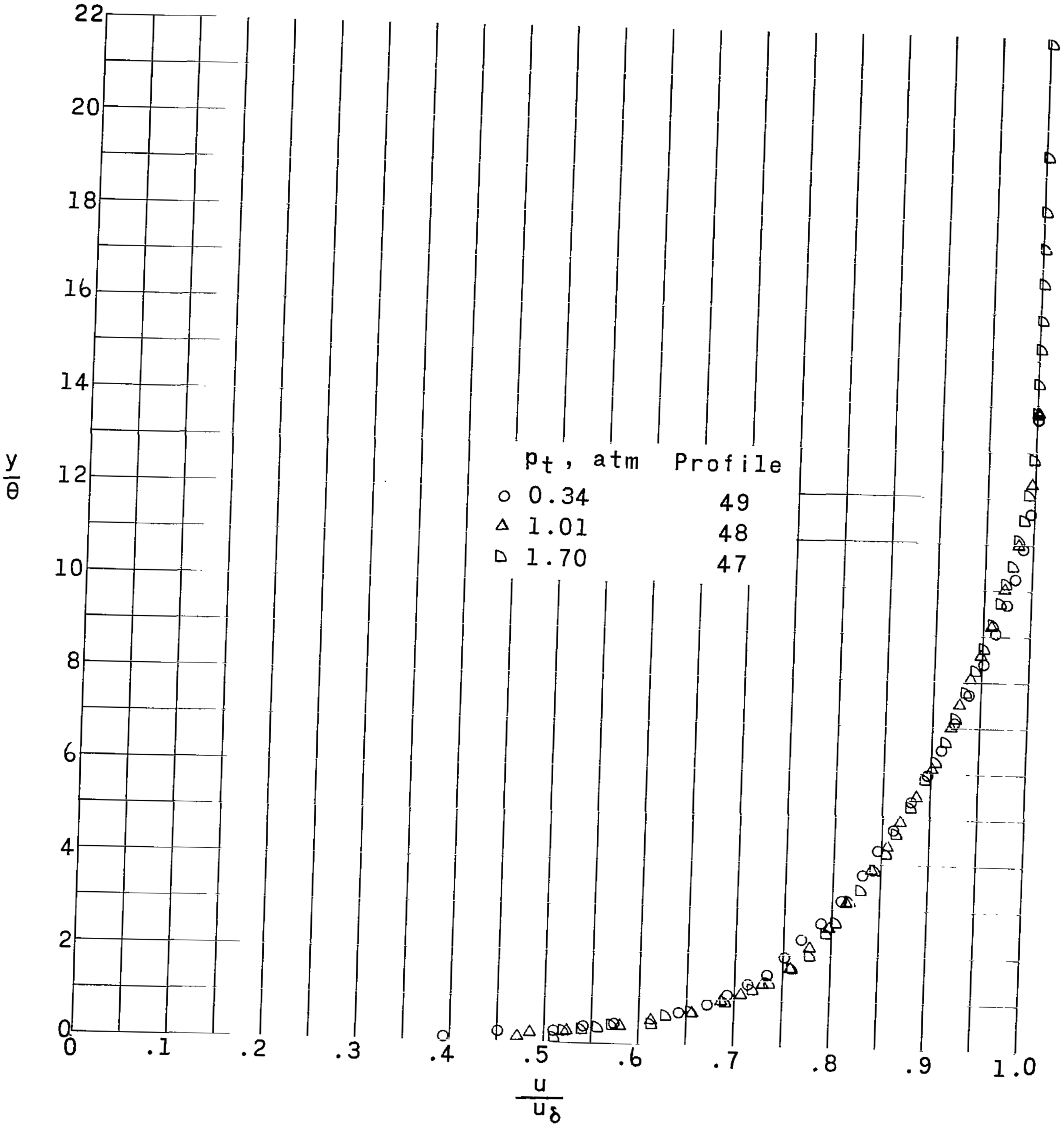

(b) Model 1, station 2.

Figure 5.- Continued.

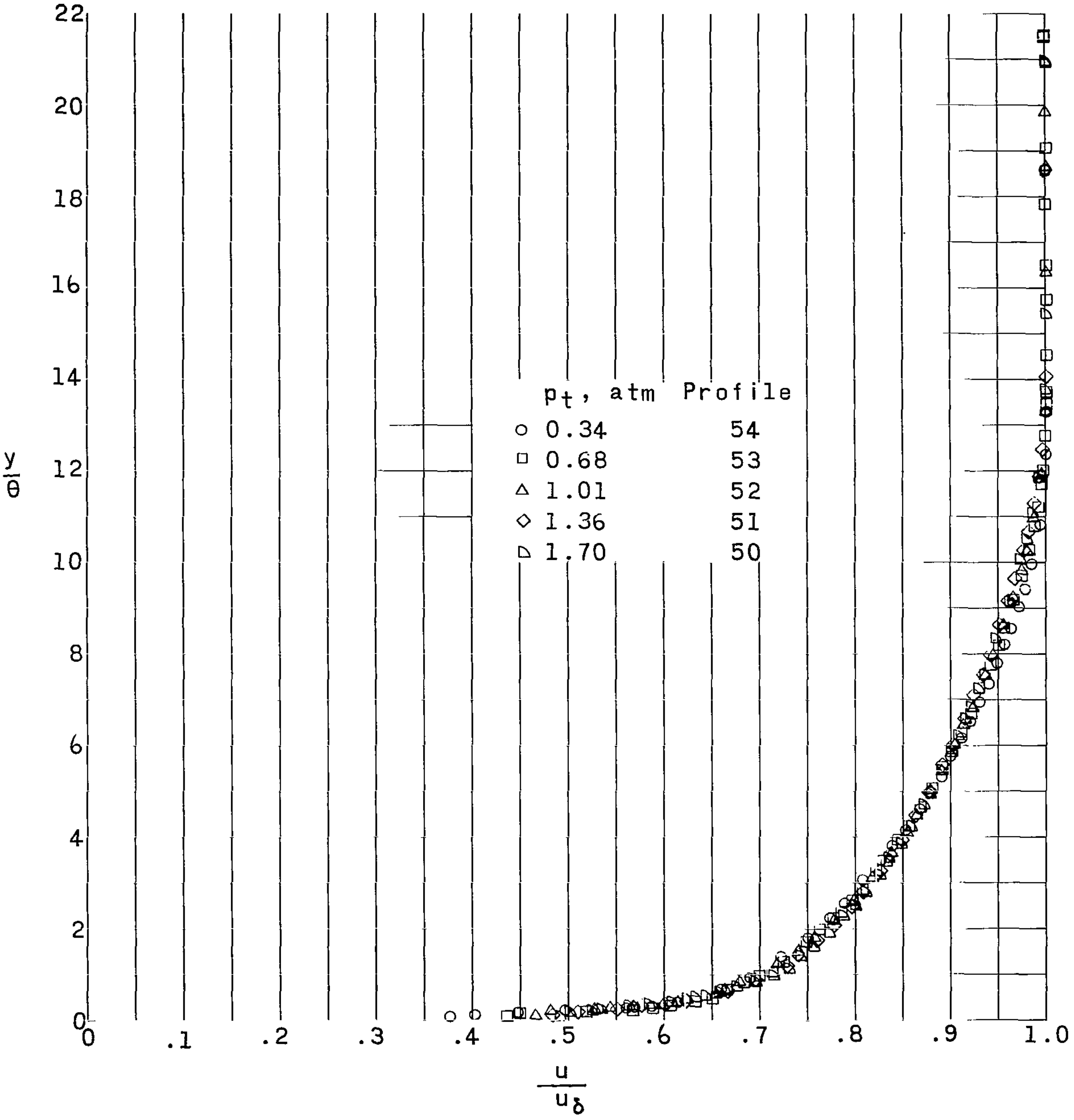

(c) Model 1, station 3.

Figure 5.- Continued.

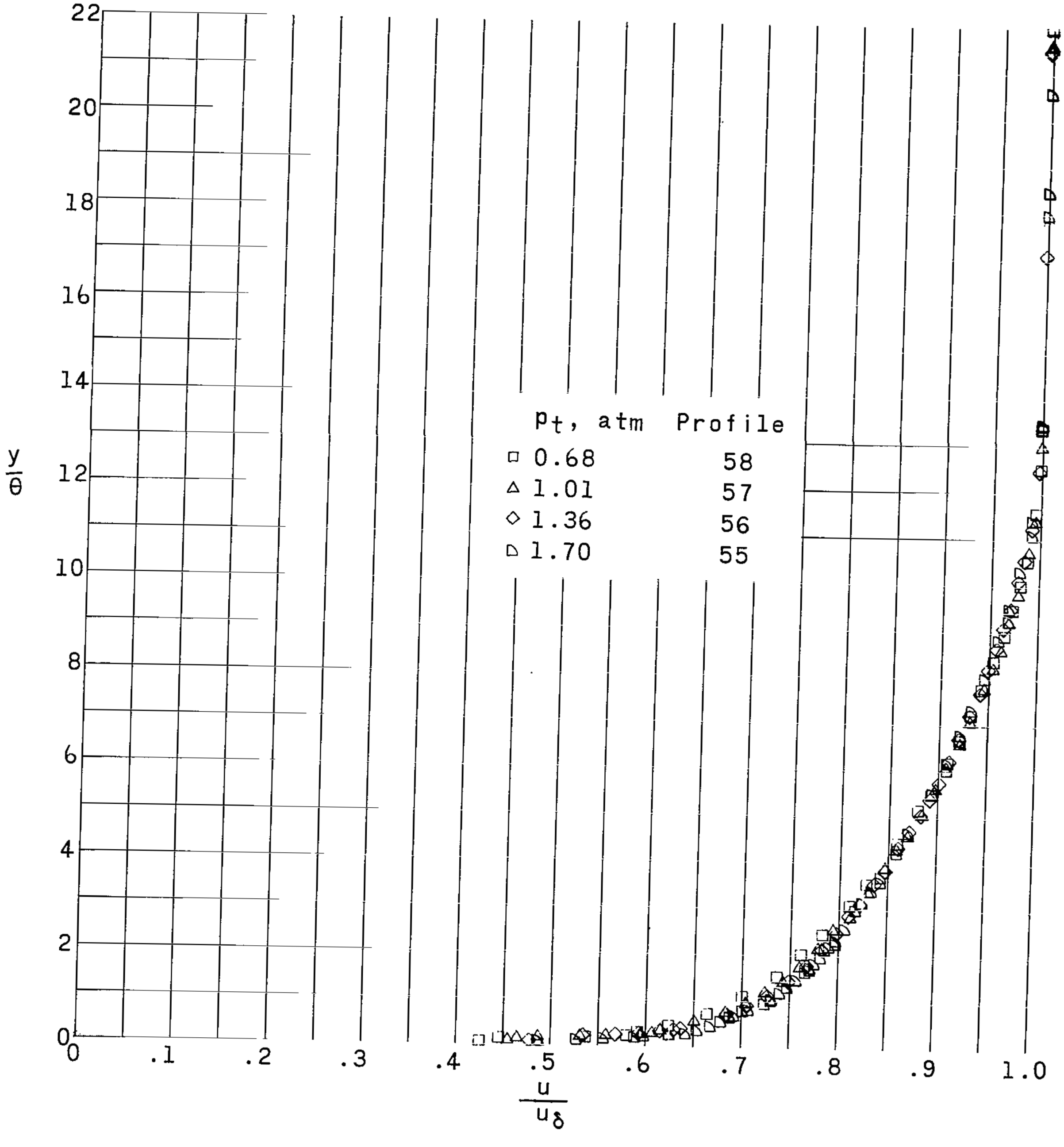

(d) Model 1, station 4.

Figure 5.- Continued.

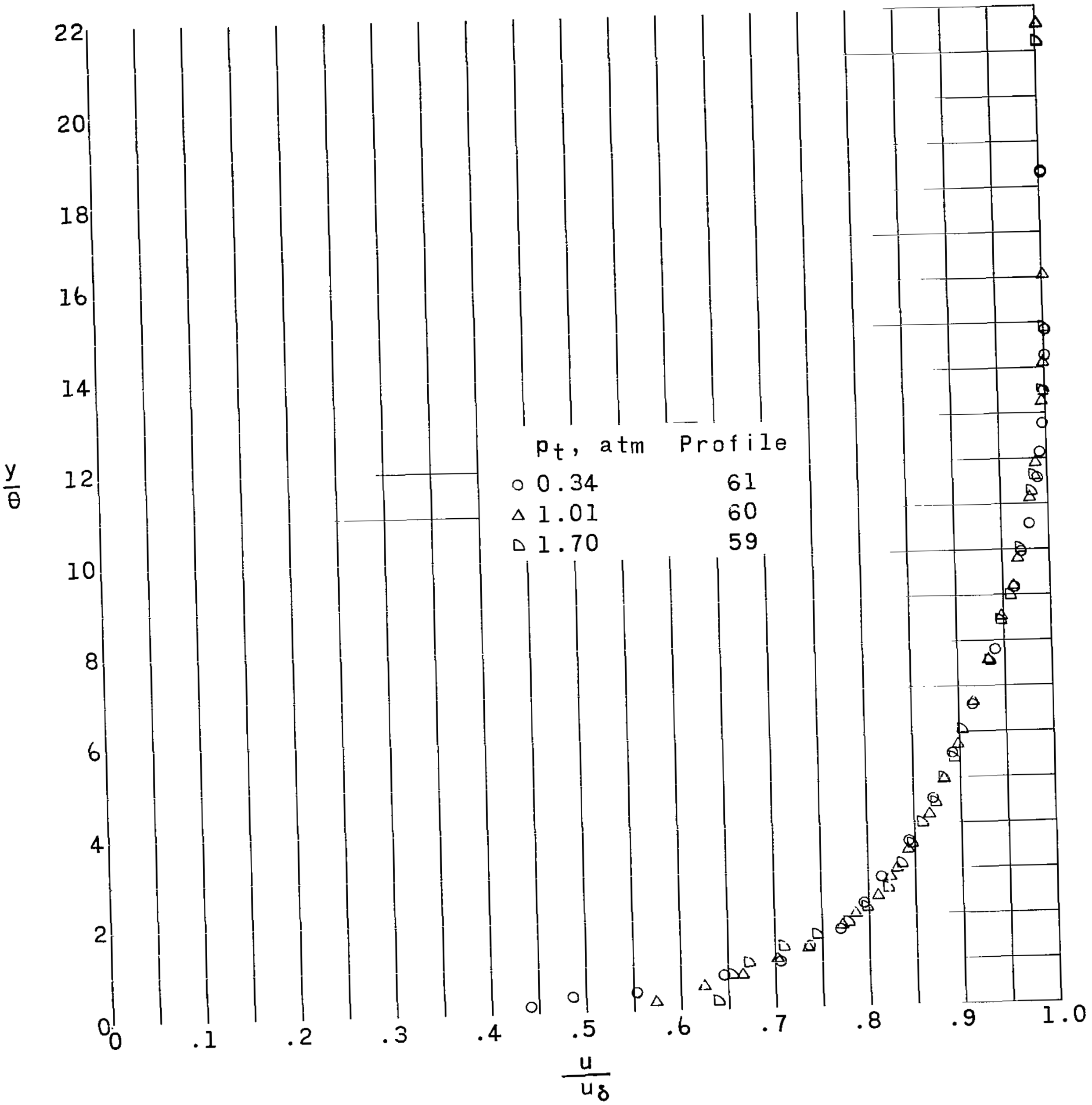

(e) Model 2, station 1.

Figure 5.- Continued.

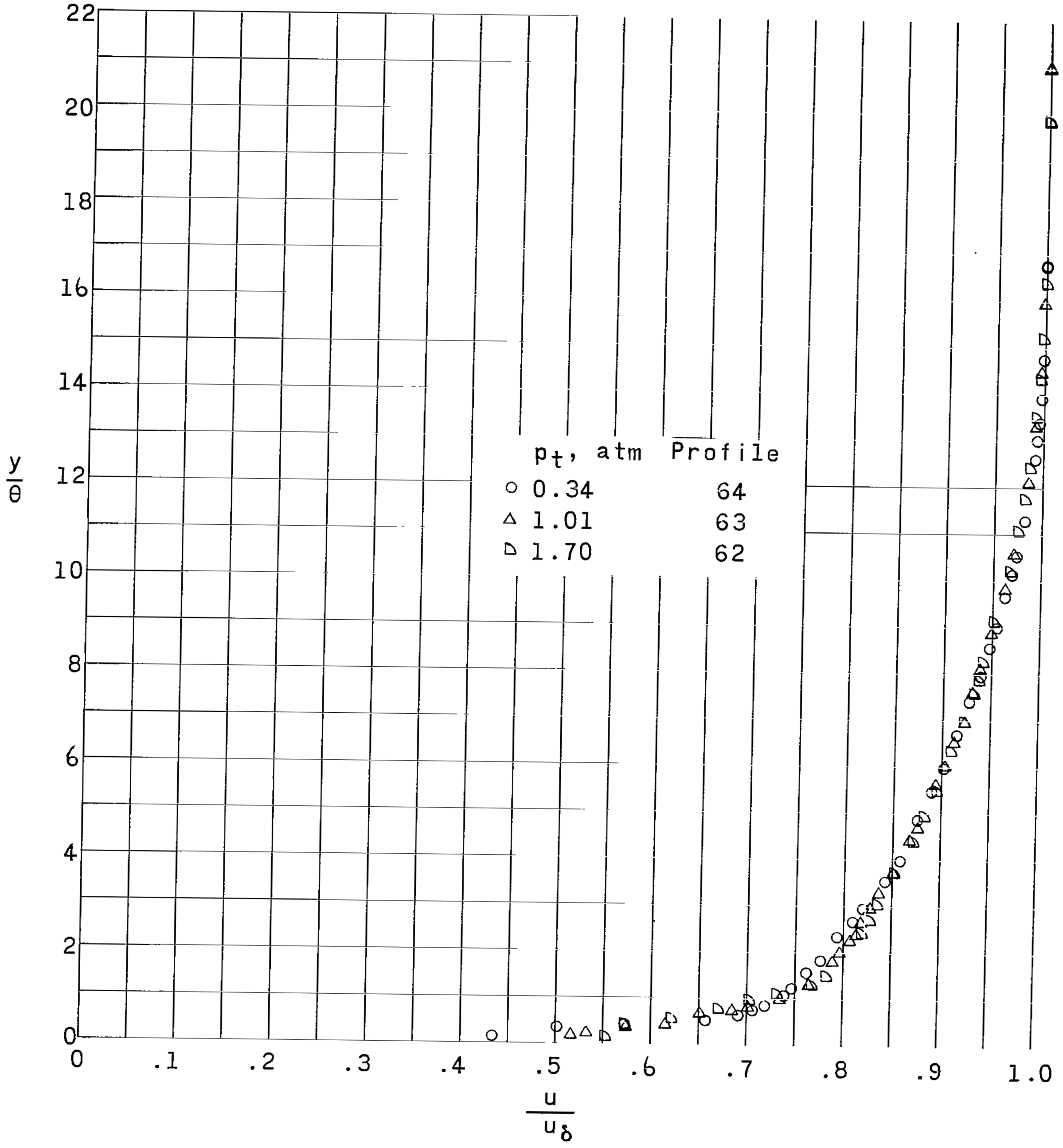

(f) Model 2, station 2.

Figure 5.- Continued.

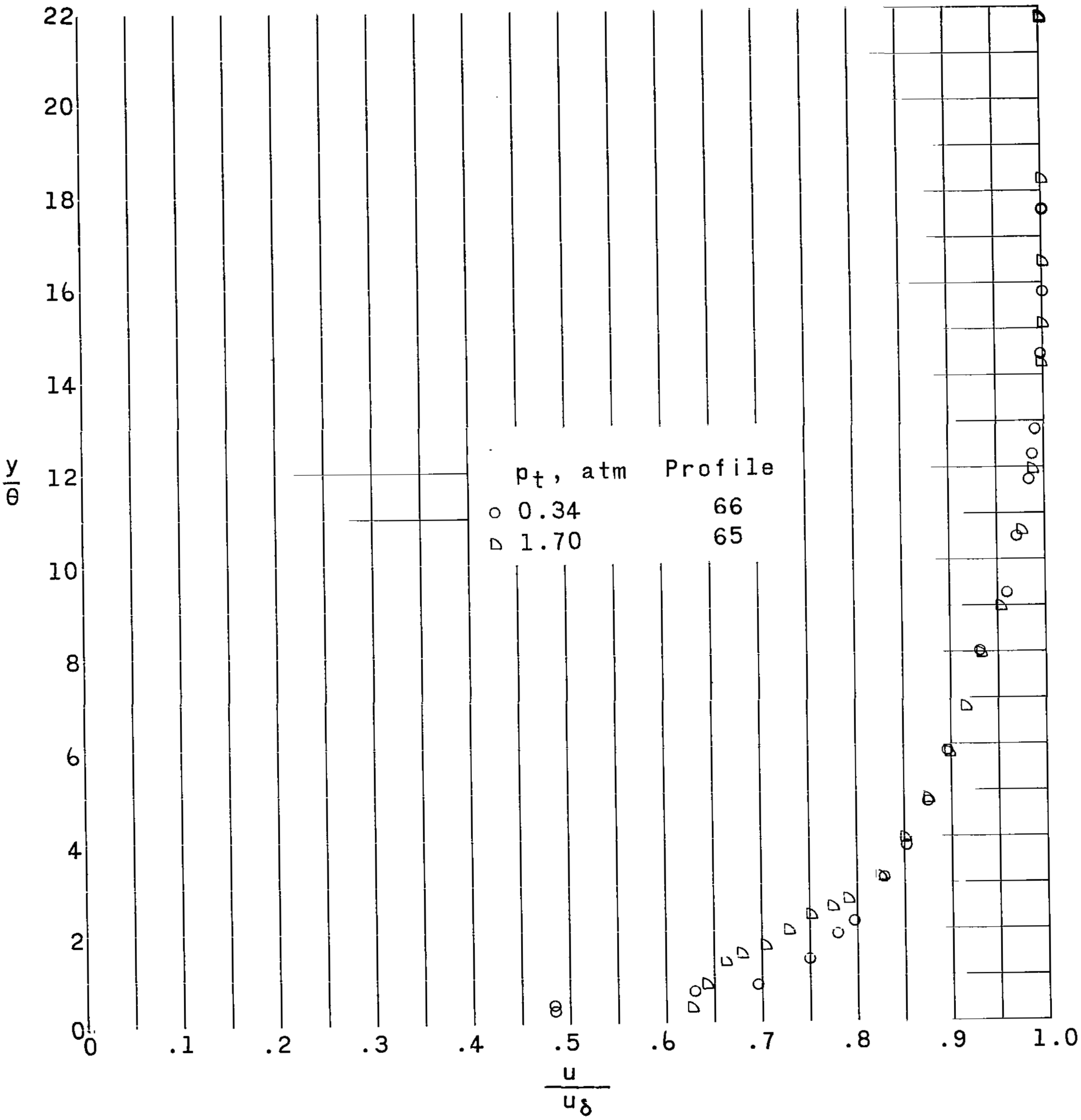

(g) Model 3, station 1.

Figure 5.- Continued.

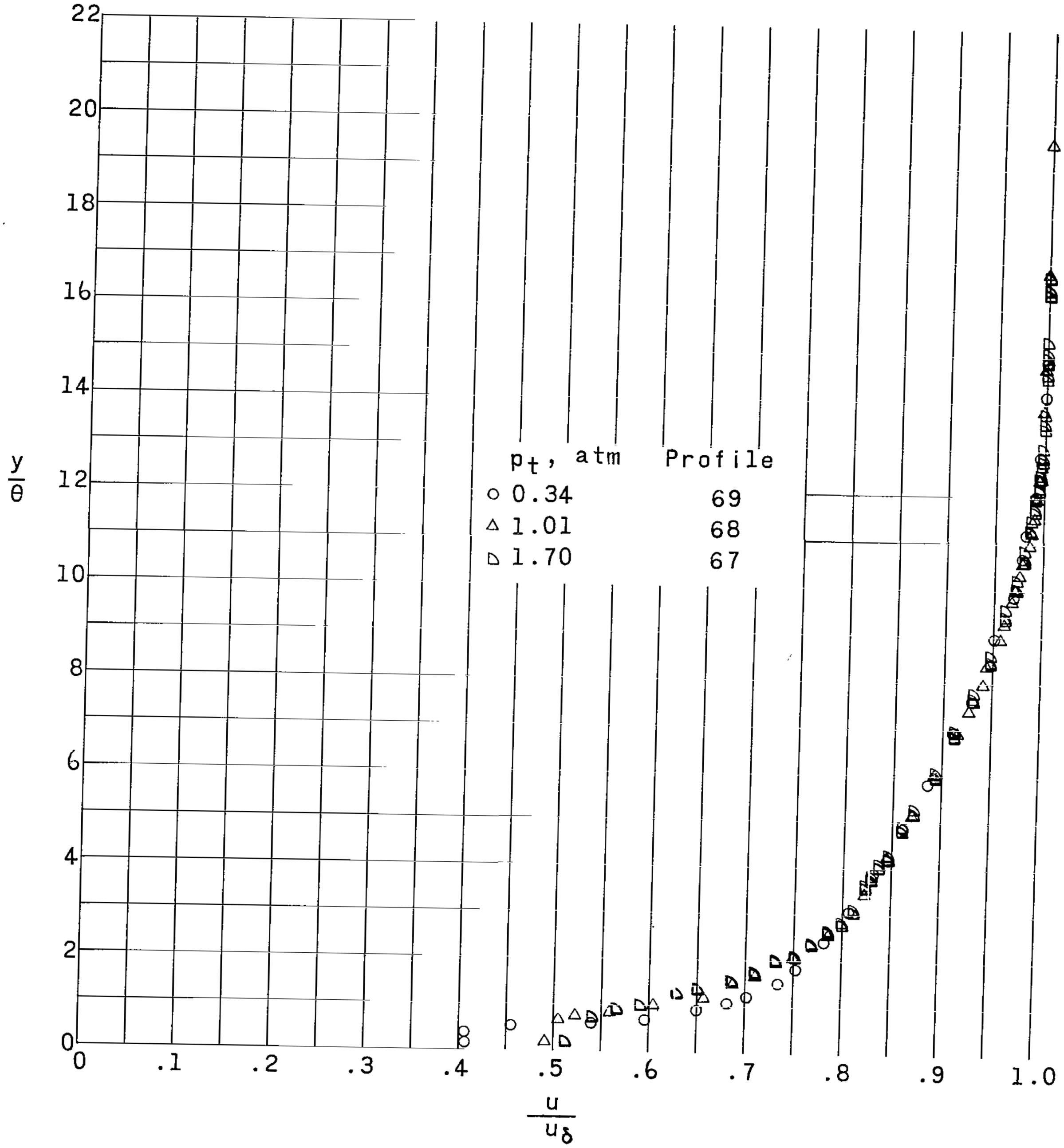

(h) Model 3, station 2.

Figure 5.- Continued.

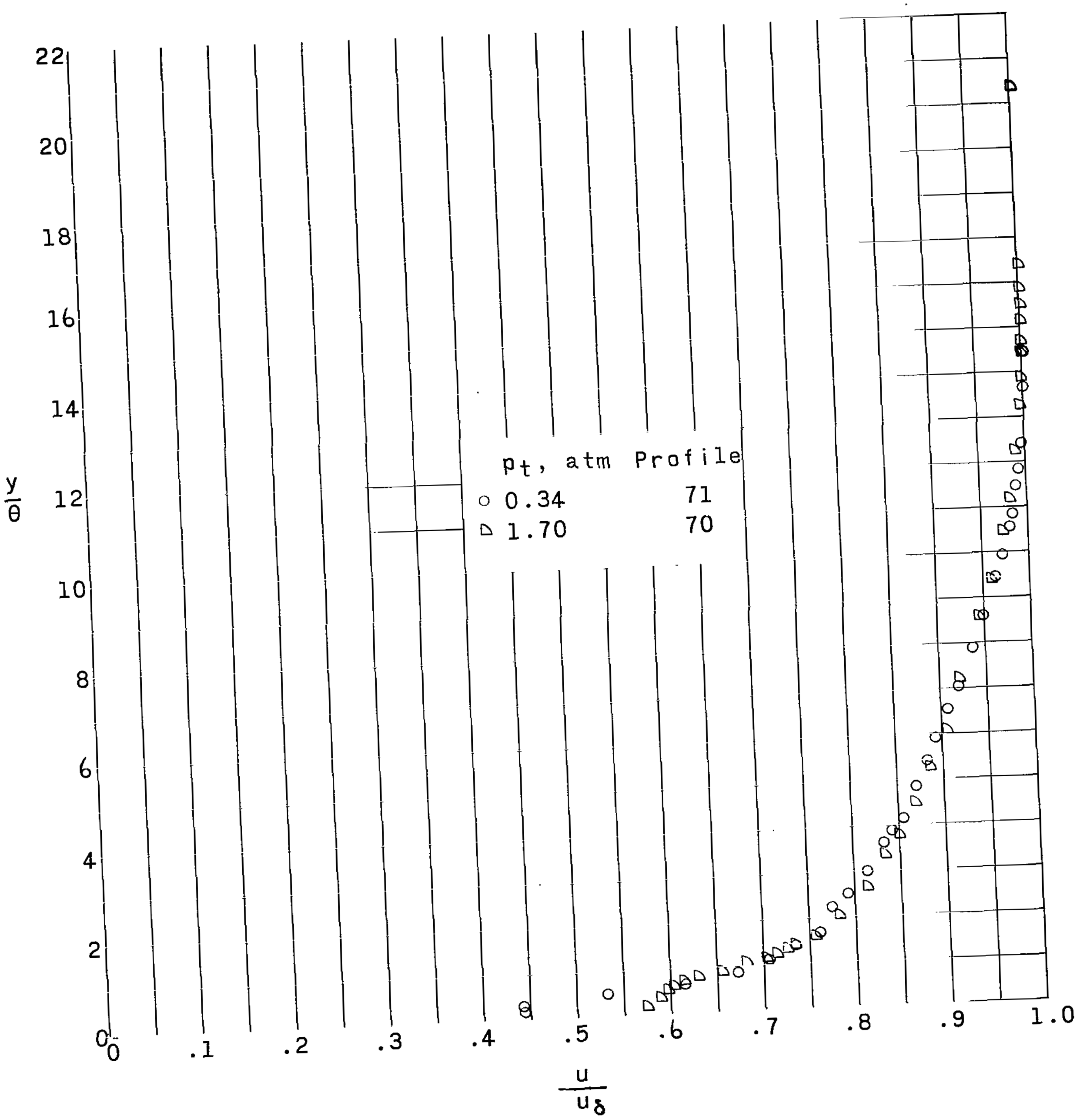

(i) Model 4, station 1.

Figure 5.- Continued.

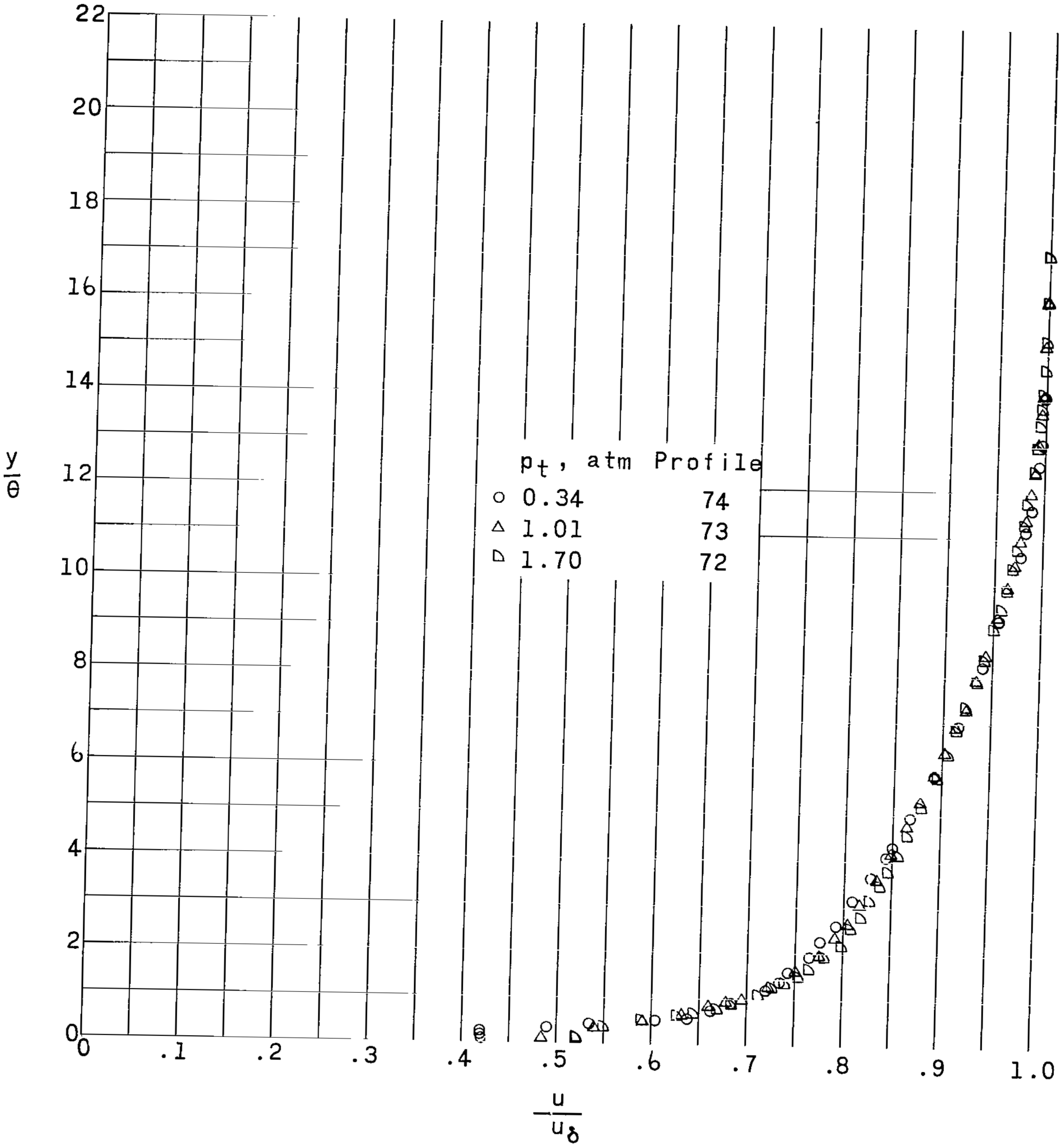

(j) Model 4, station 2.

Figure 5.- Continued.

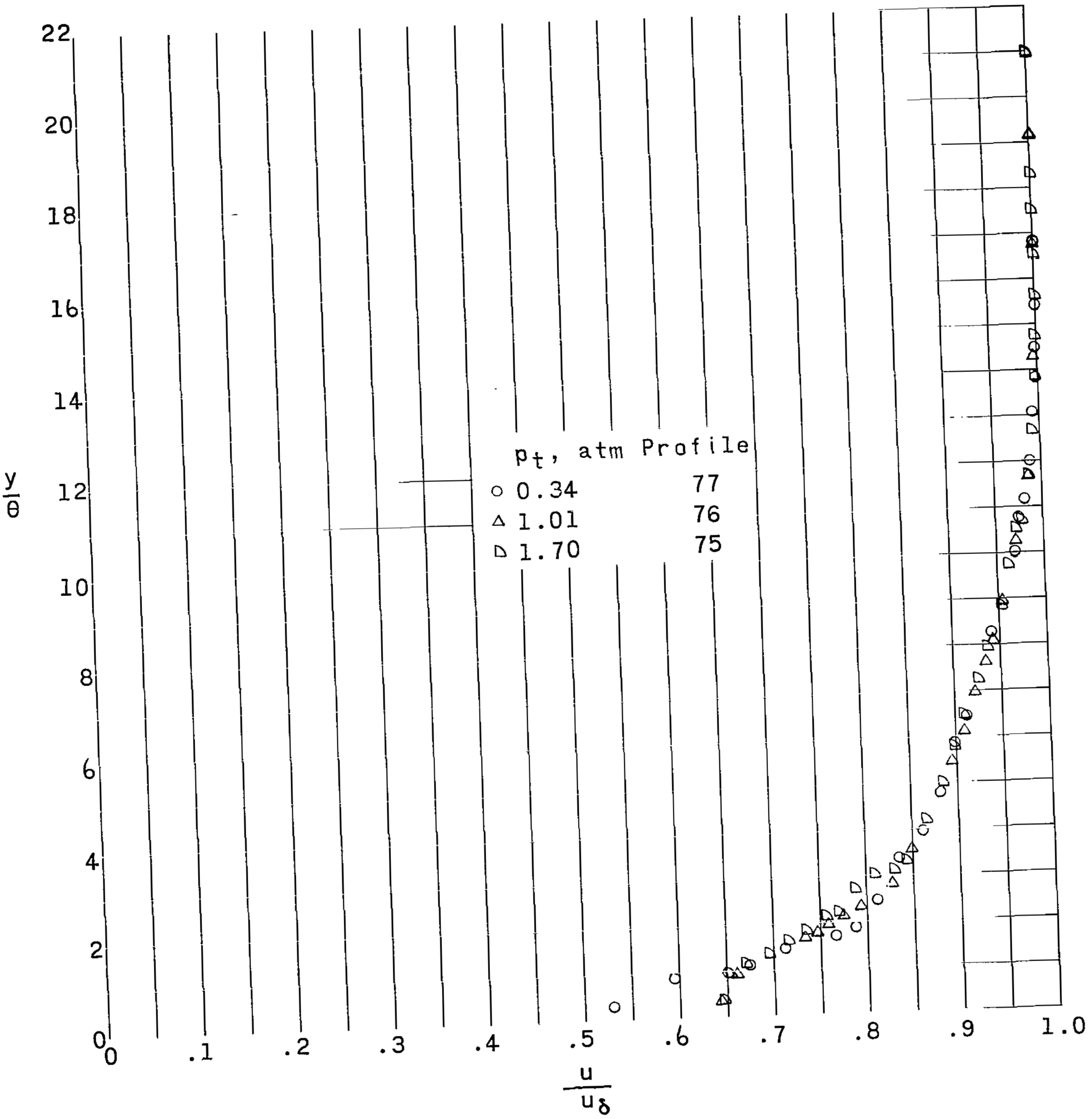

(k) Model 5, station 1.

Figure 5.- Continued.

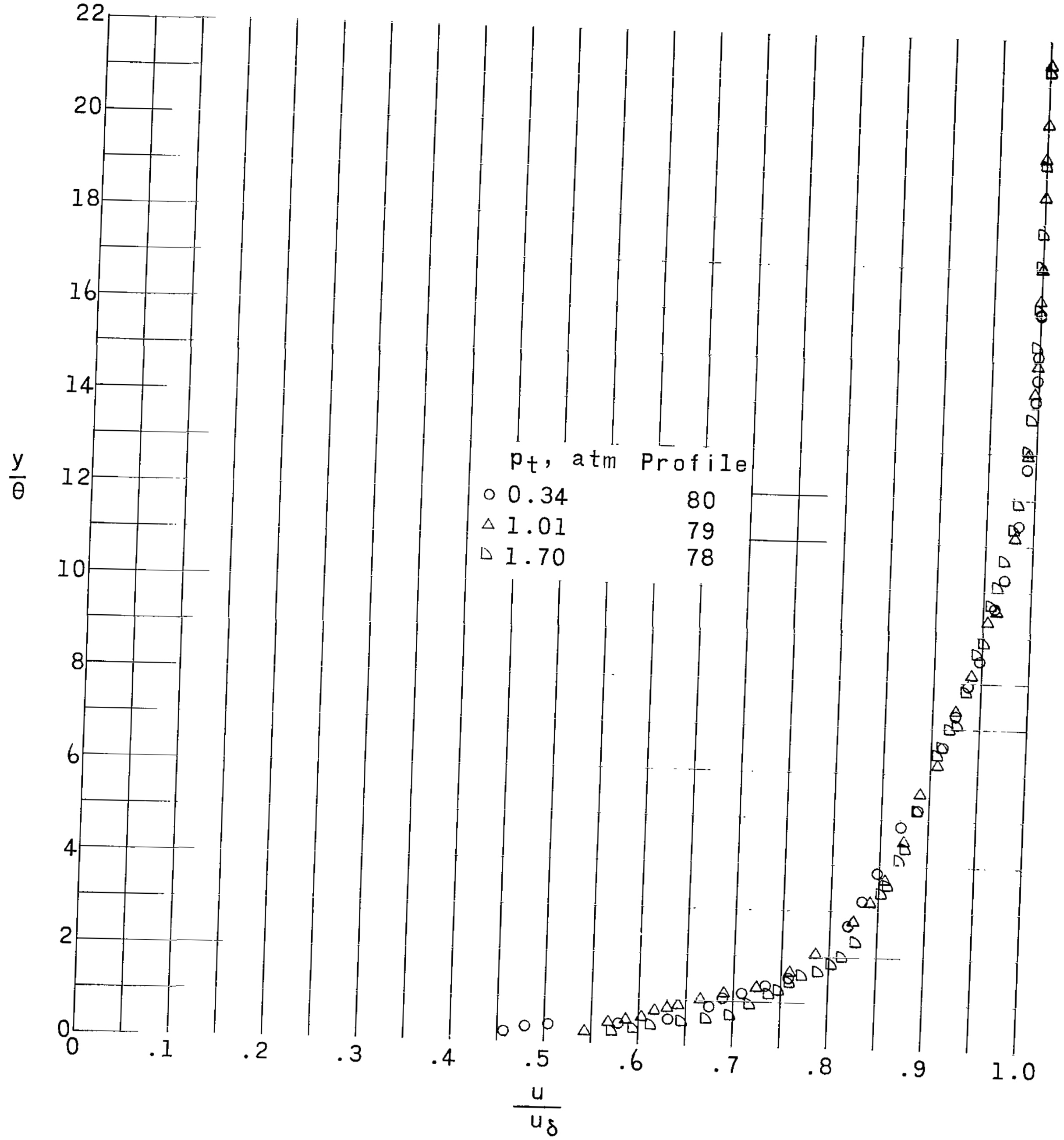

(l) Model 5, station 2.

Figure 5.- Continued.

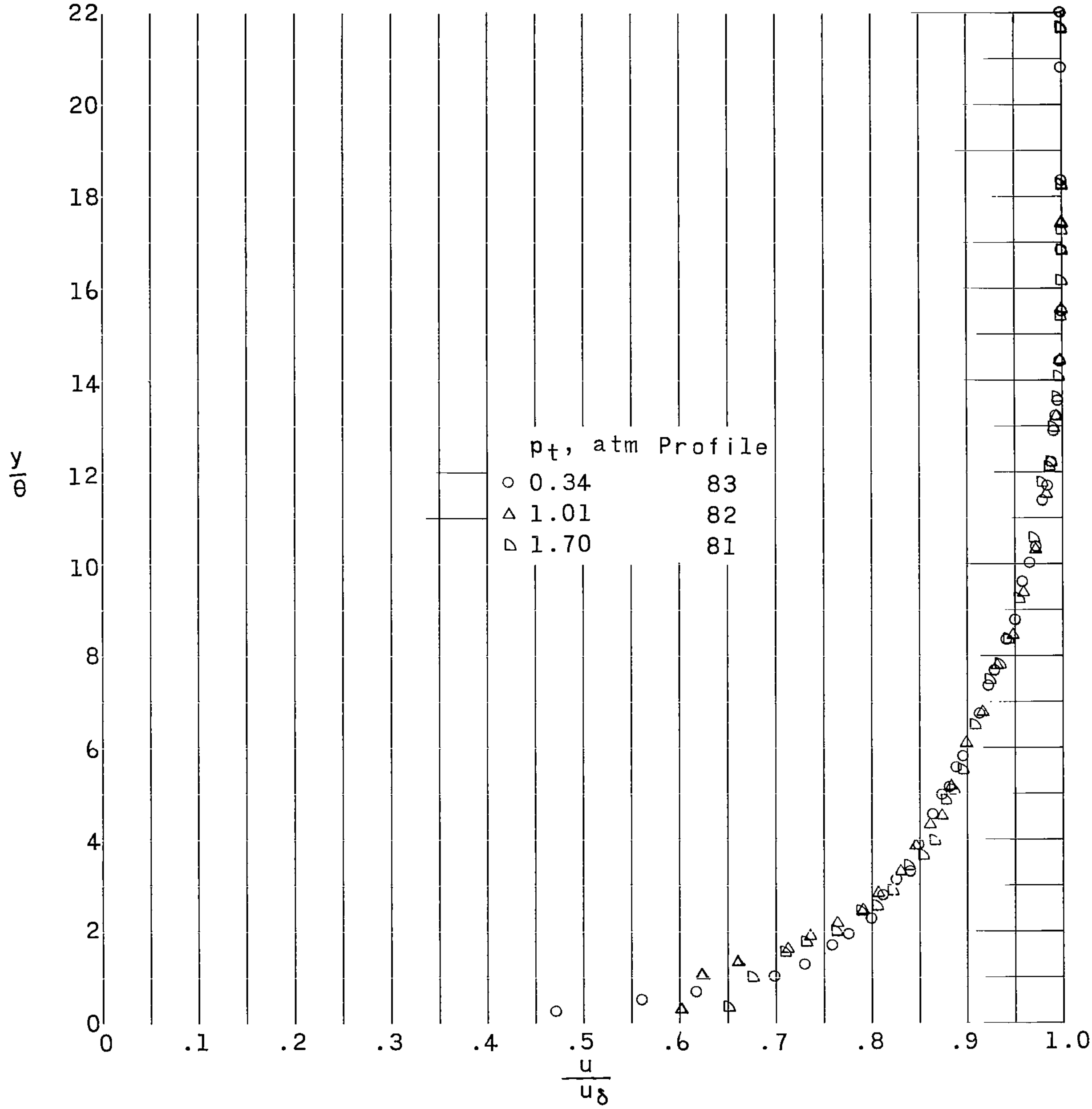

(m) Model 6, station 1.

Figure 5.- Continued.

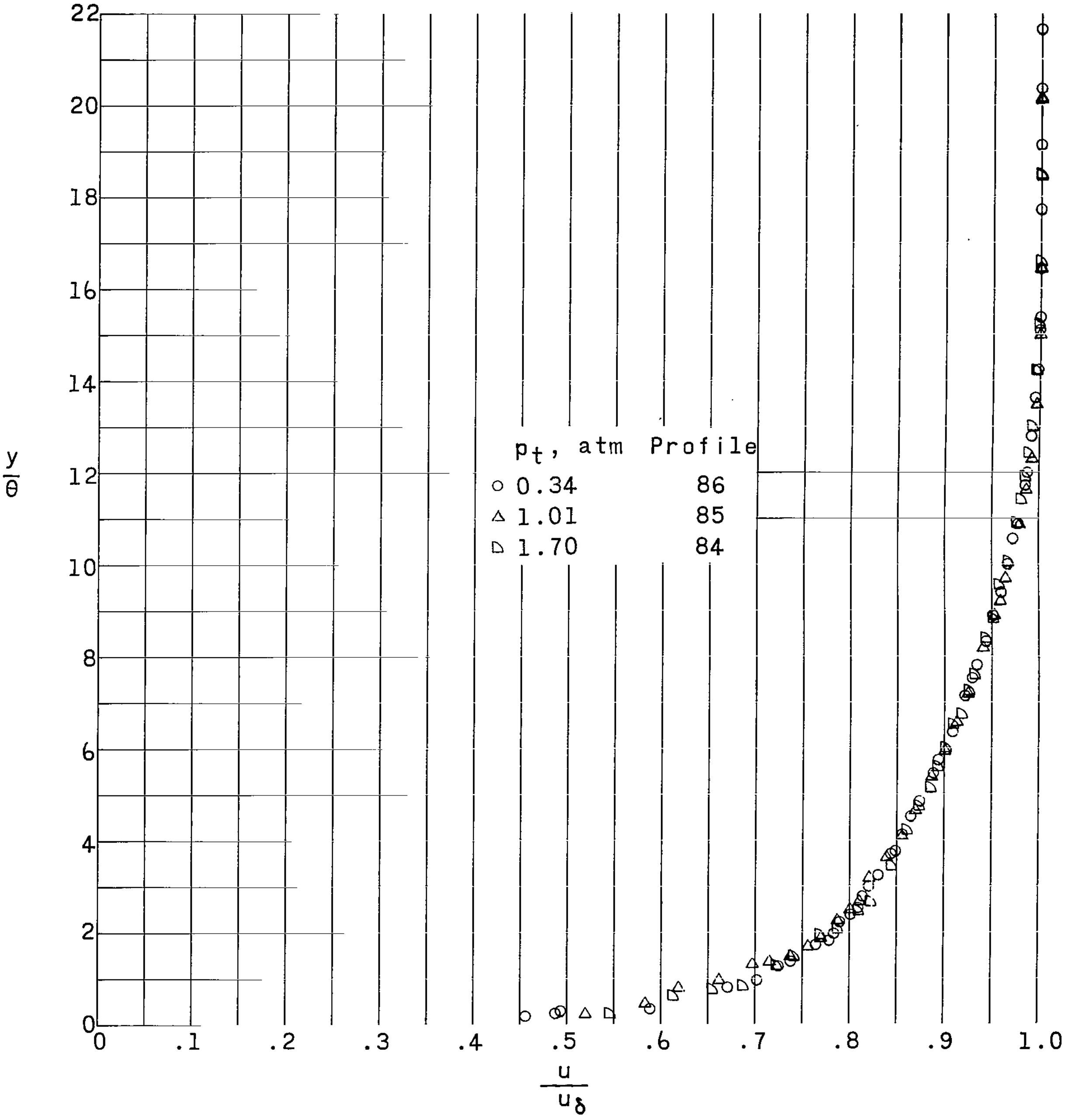

(n) Model 6, station 2.

Figure 5.- Continued.

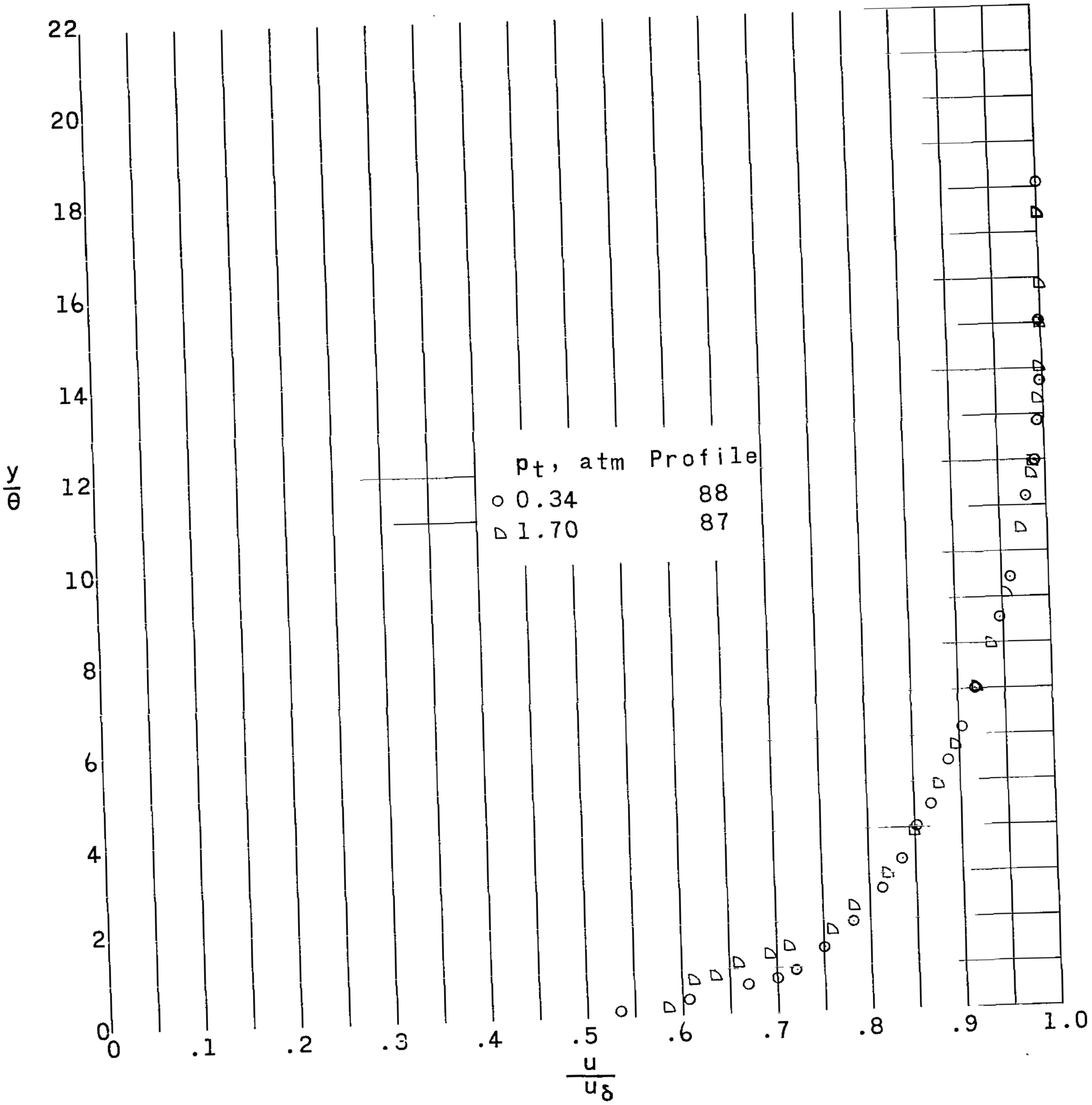

(o) Model 7, station 1.

Figure 5.- Continued.

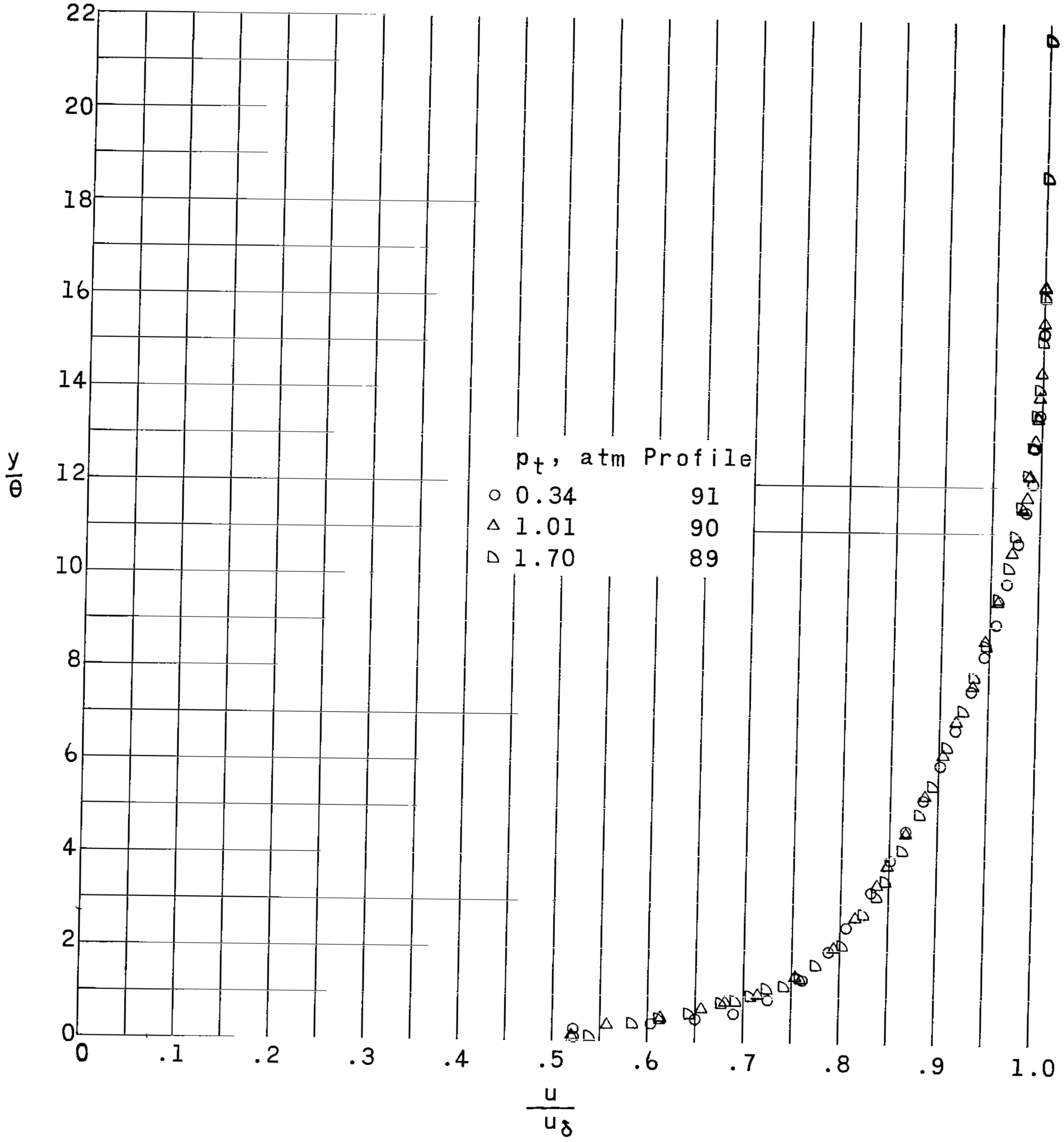

(p) Model 7, station 2.

Figure 5.- Continued.

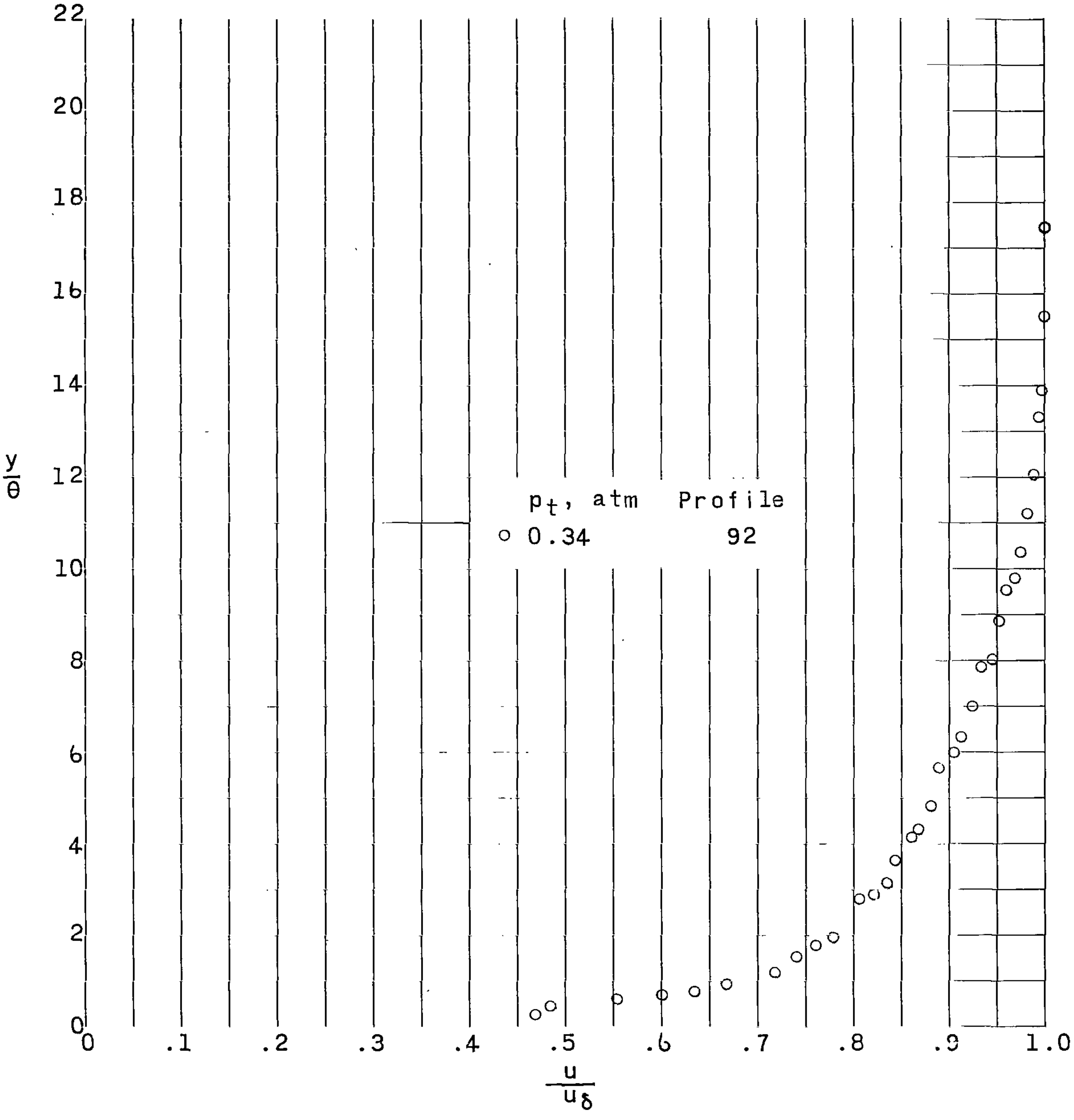

(q) Model 8, station 1.

Figure 5.- Continued.

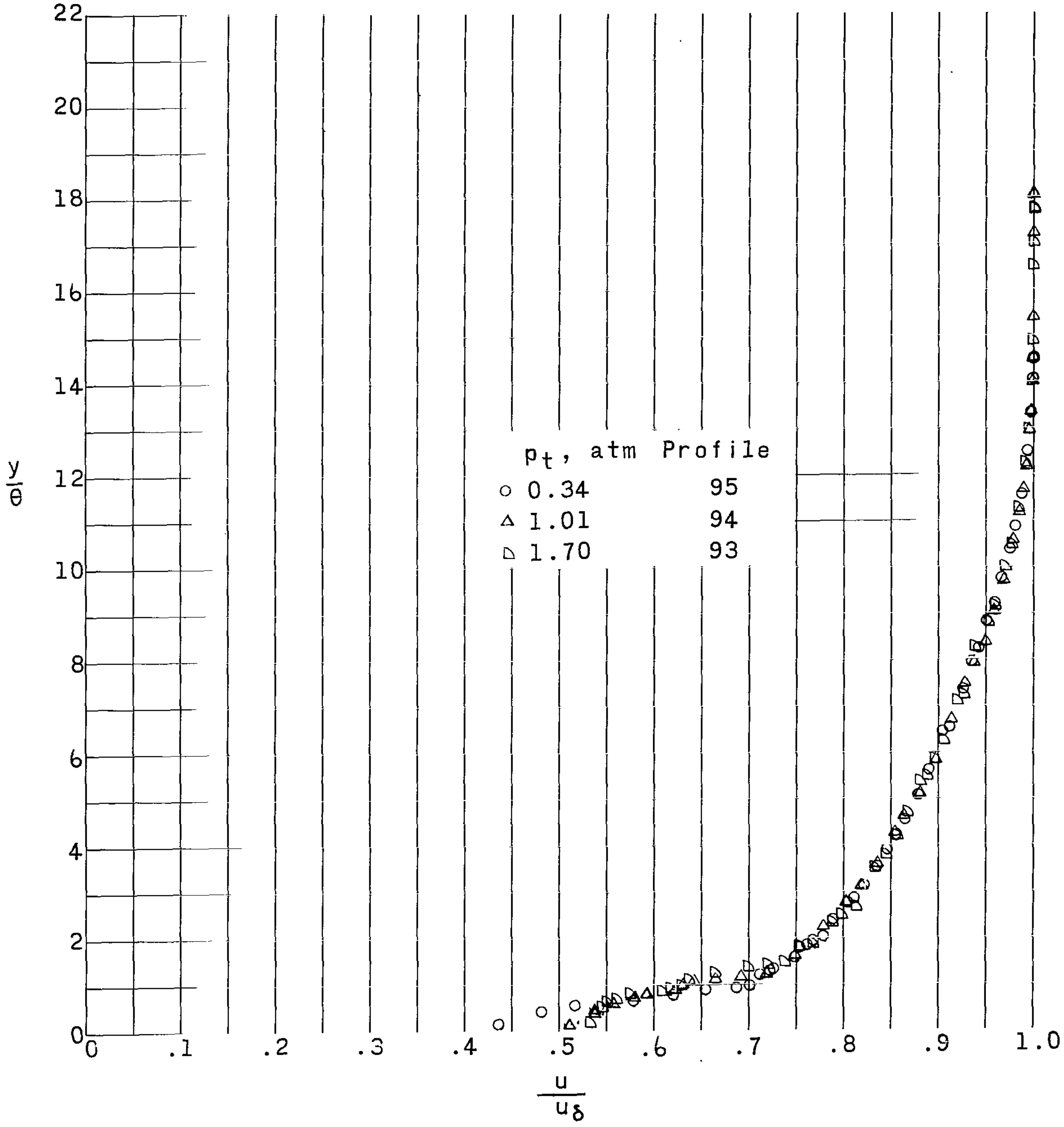

(r) Model 8, station 2.

Figure 5.- Concluded.

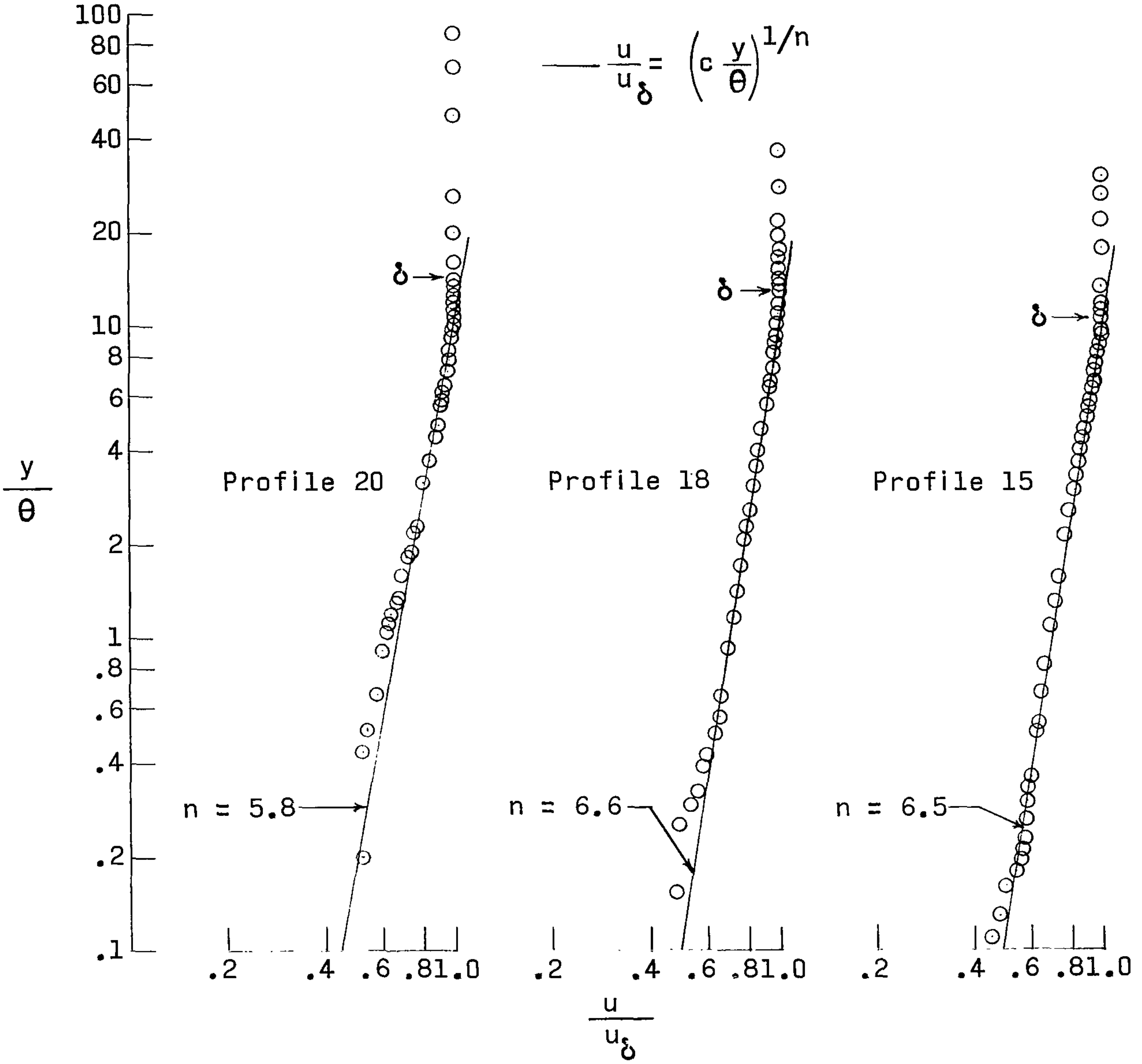

(a) $M_\infty = 1.61$; $p_t = 0.34$ atm.

Figure 6.- Sample velocity profiles in logarithmic form.

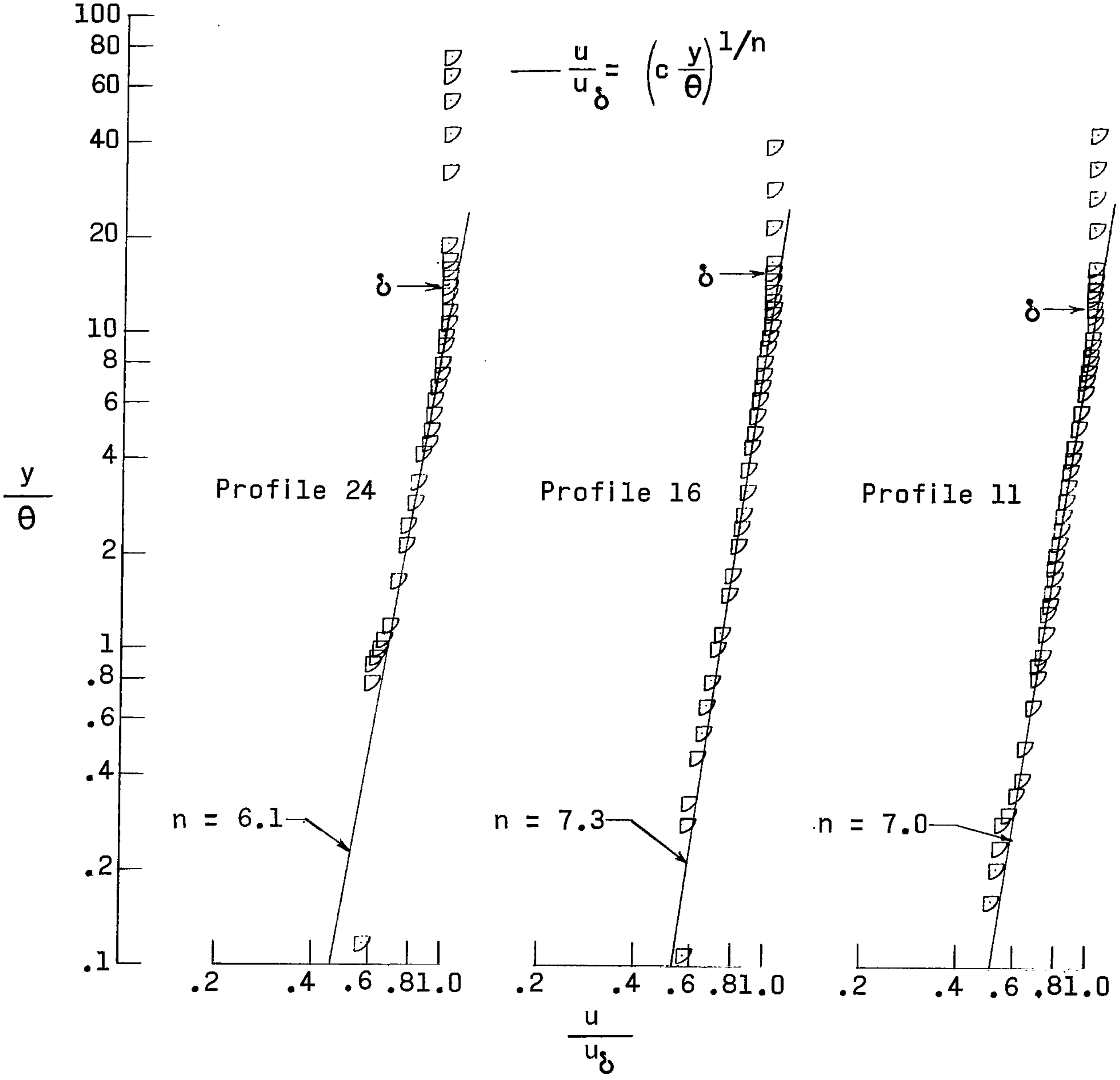

(b) $M_\infty = 1.61$; $p_t = 1.70$ atm.

Figure 6.- Continued.

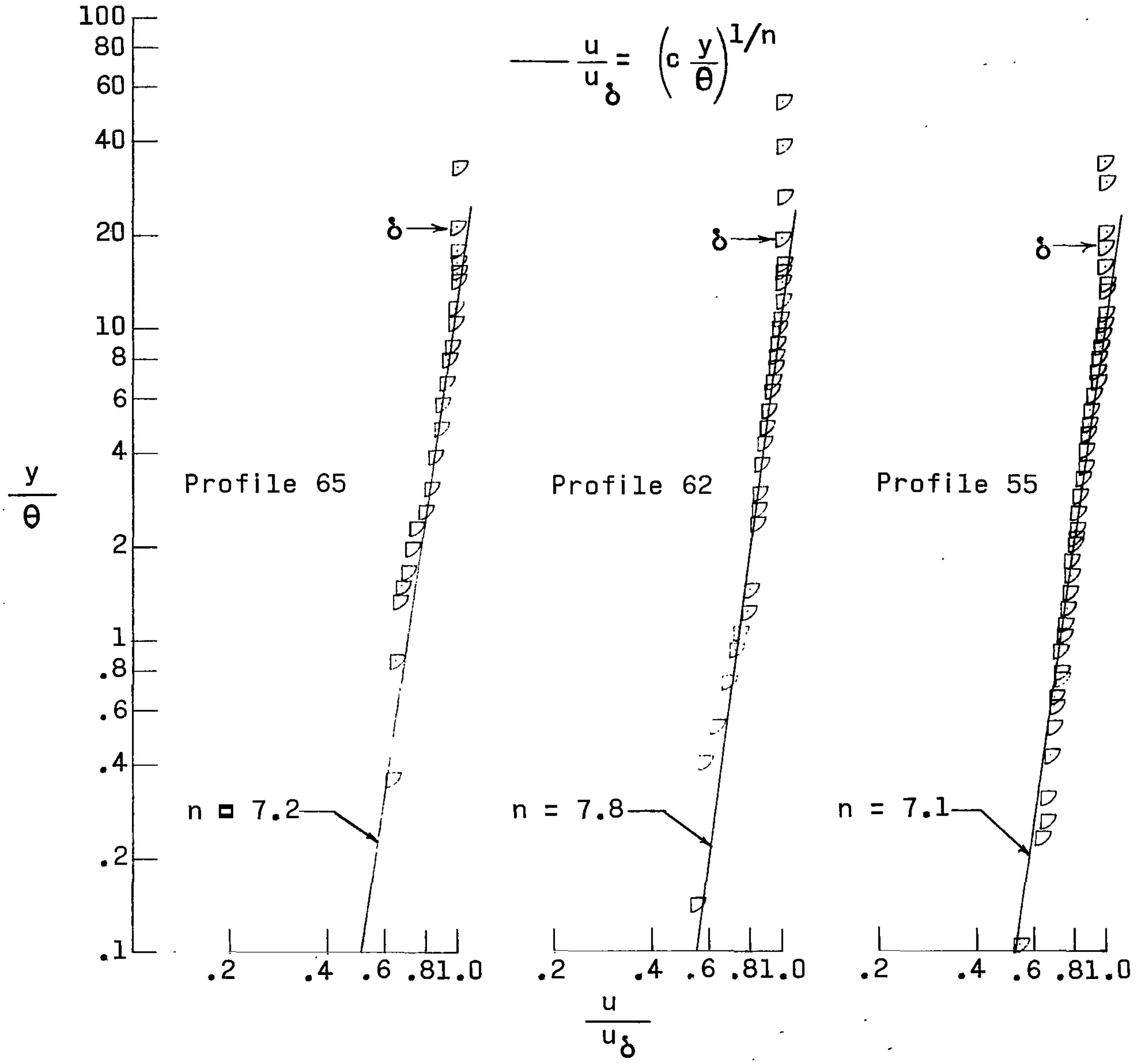

(c) $M_\infty = 2.20$; $p_t = 1.70$ atm.

Figure 6.- Concluded.

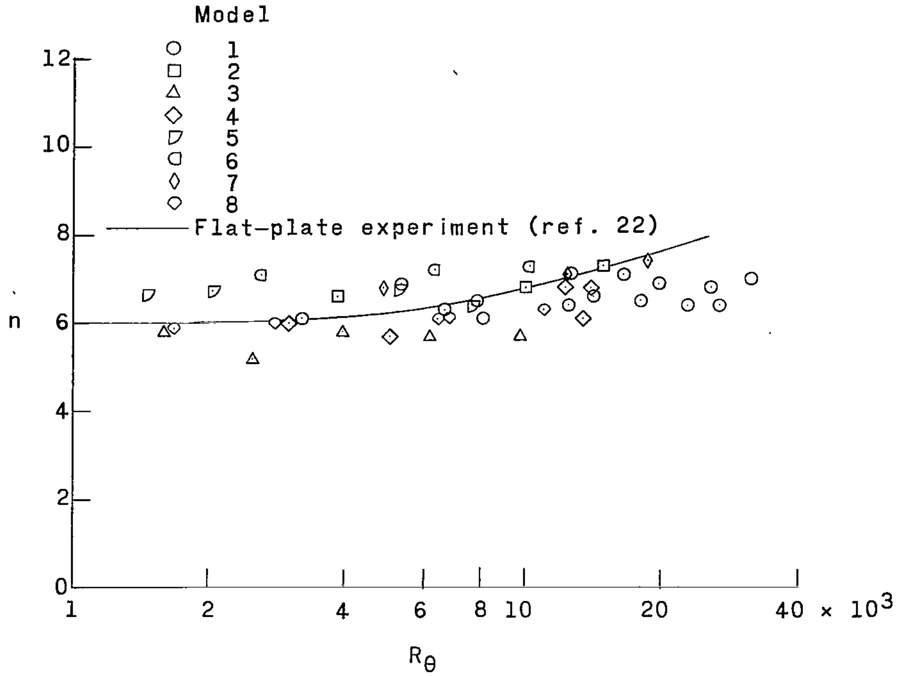

(a) $M_\infty = 1.61$.

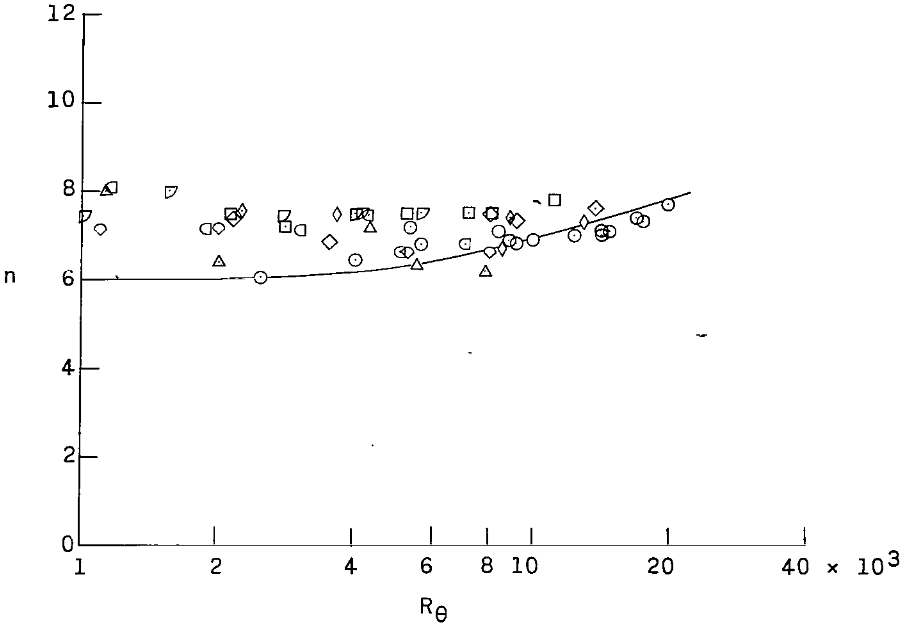

(b) $M_\infty = 2.20$.

Figure 7.- Variation of velocity profile index with Reynolds number based on momentum thickness.

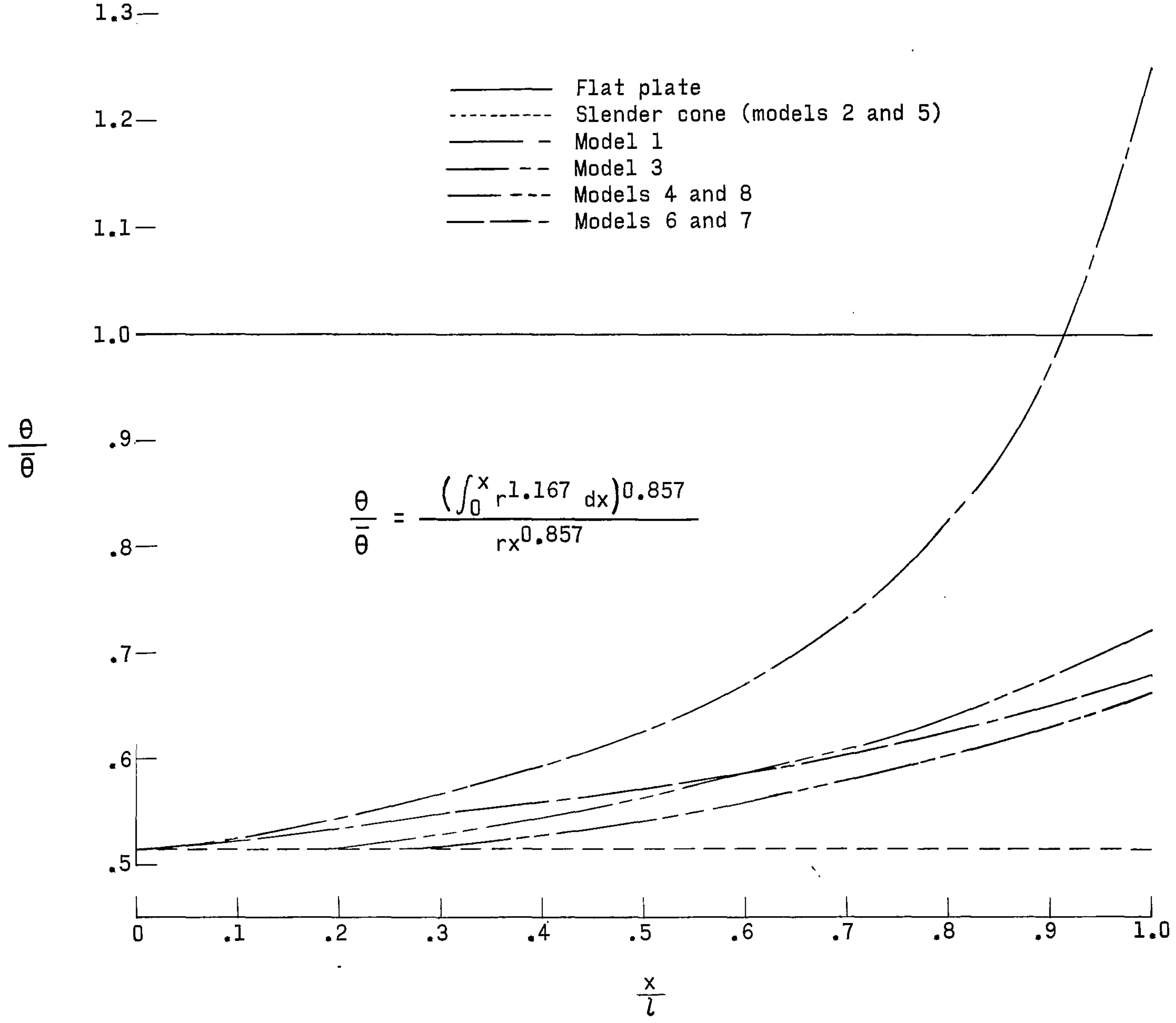

Figure 8.- Theoretical momentum thickness ratios calculated by equation (3).

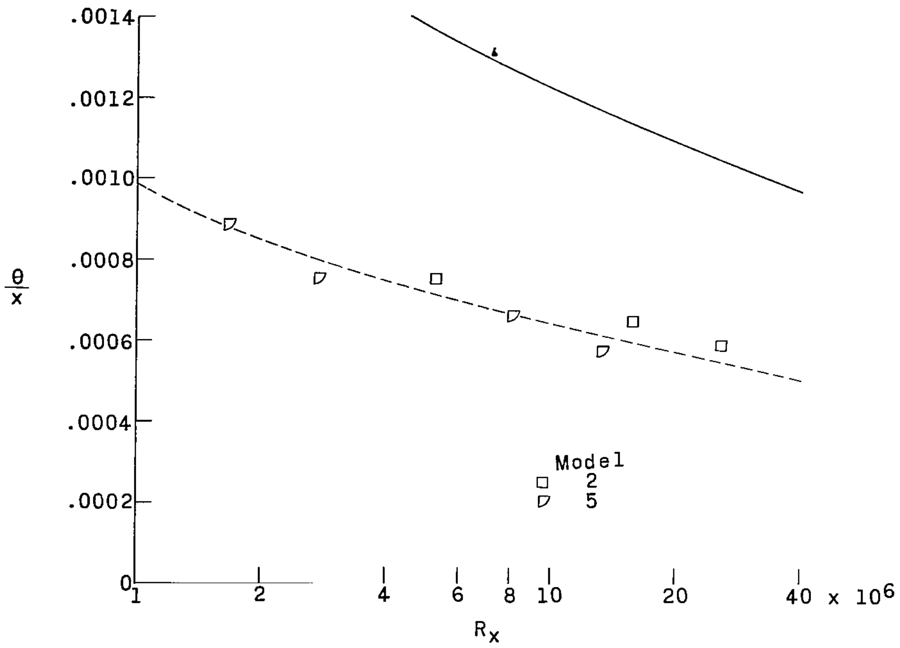

(a) $M_\infty = 1.61$.

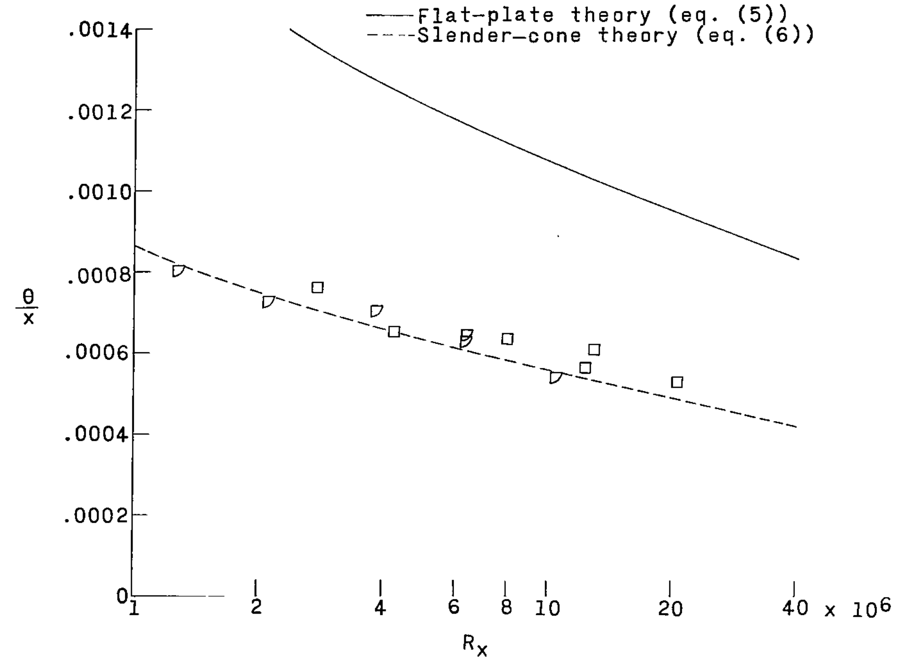

(b) $M_\infty = 2.20$.

Figure 9.- Momentum thickness distributions on models 2 and 5 (slender cones).

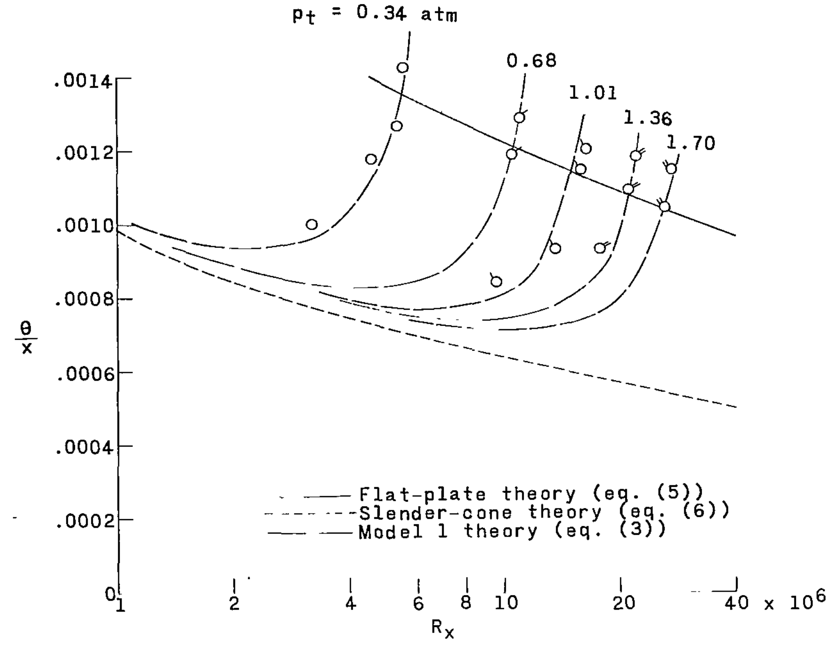

(a) M_∞ = 1.61.

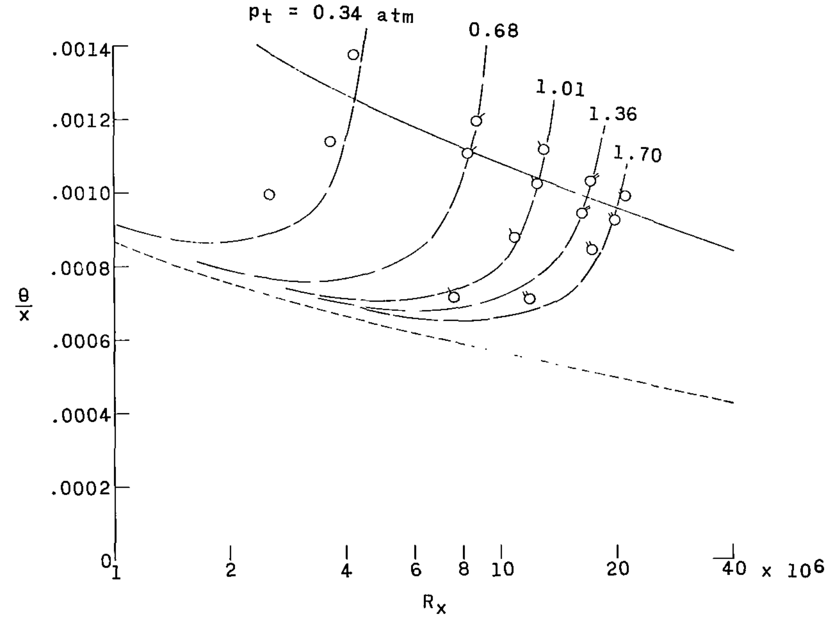

(b) M_∞ = 2.20.

Figure 10.- Momentum thickness distribution on model 1 (RM-10). Ticks differentiate between the stagnation pressure levels.

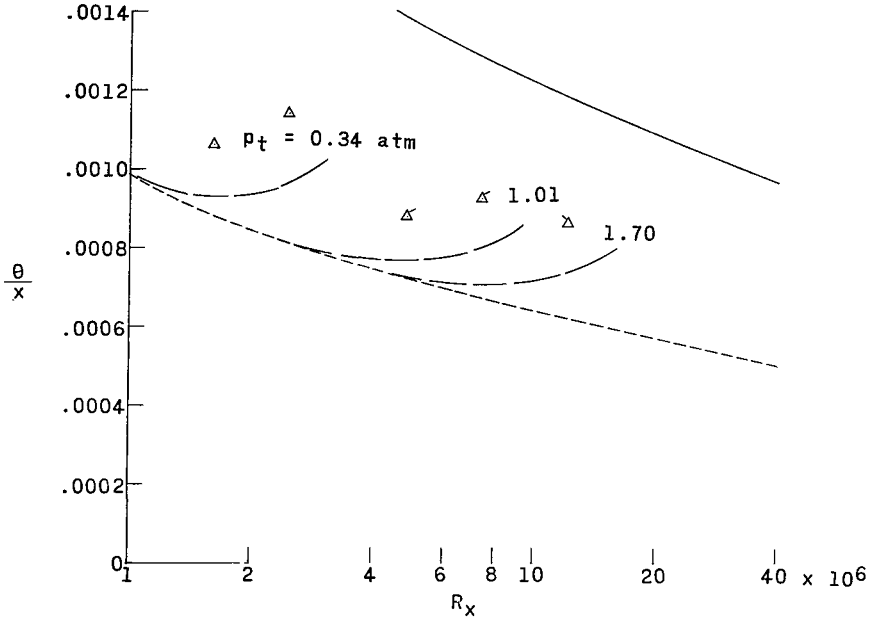

(a) $M_\infty = 1.61$.

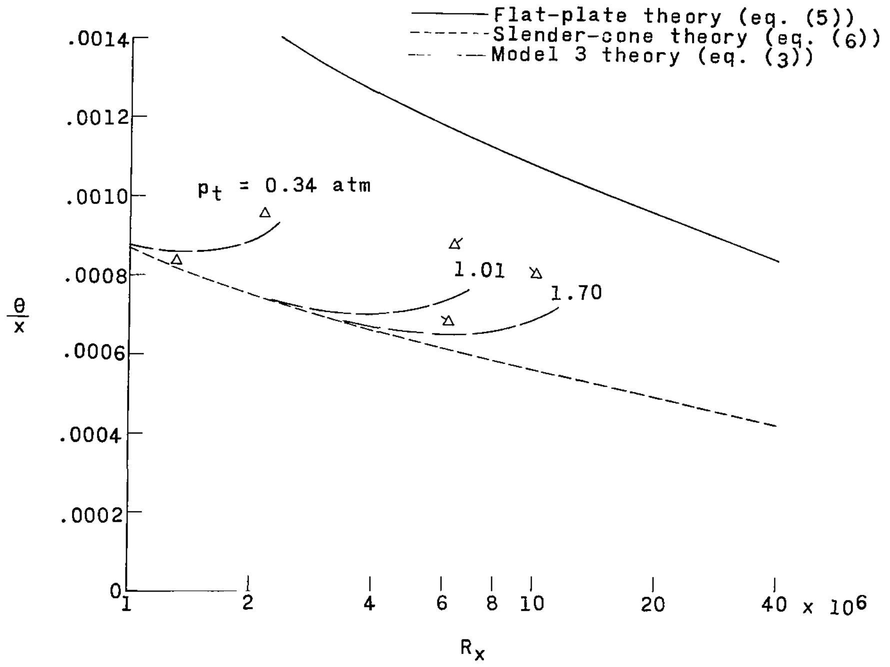

(b) $M_\infty = 2.20$.

Figure 11.- Momentum thickness distribution on model 3 (cone-parabolic arc). Ticks differentiate between the stagnation pressure levels.

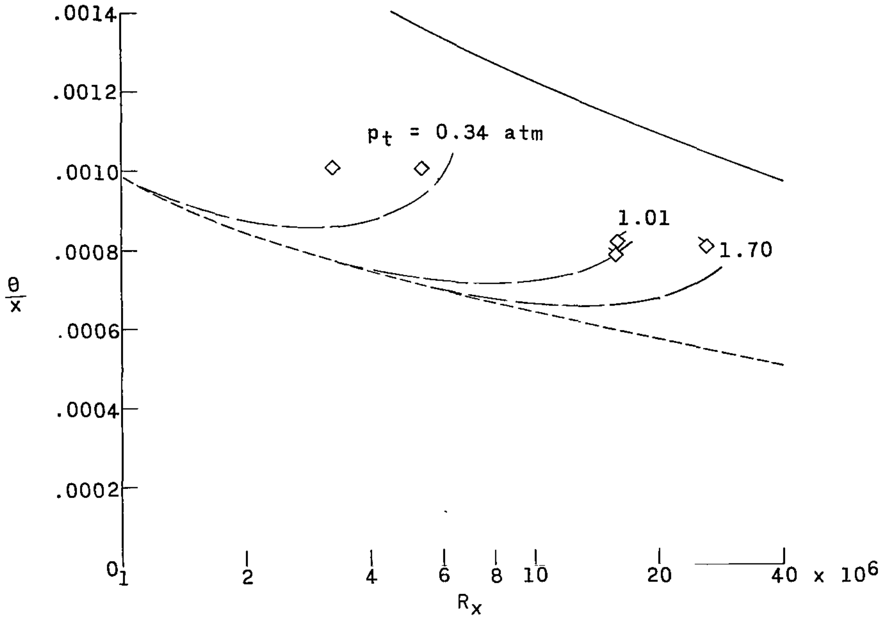

(a) $M_\infty = 1.61$.

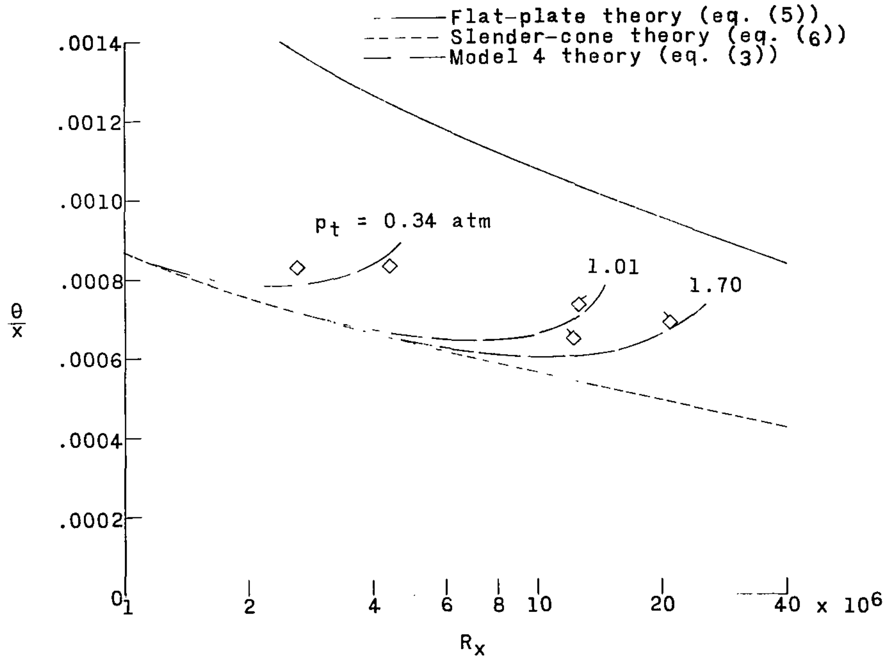

(b) $M_\infty = 2.20$.

Figure 12.- Momentum thickness distribution on model 4 (cone-parabolic arc). Ticks differentiate between the stagnation pressure levels.

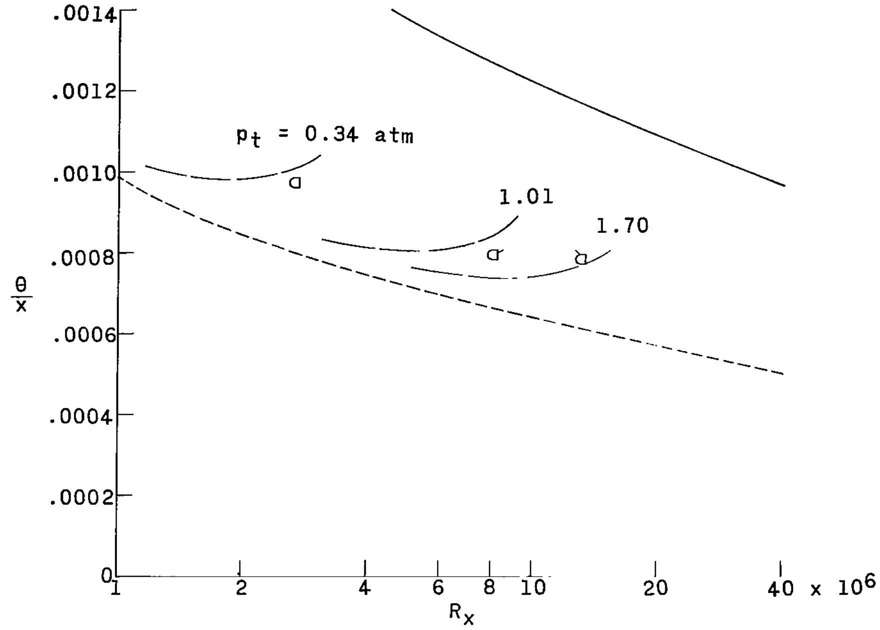

(a) $M_\infty = 1.61$.

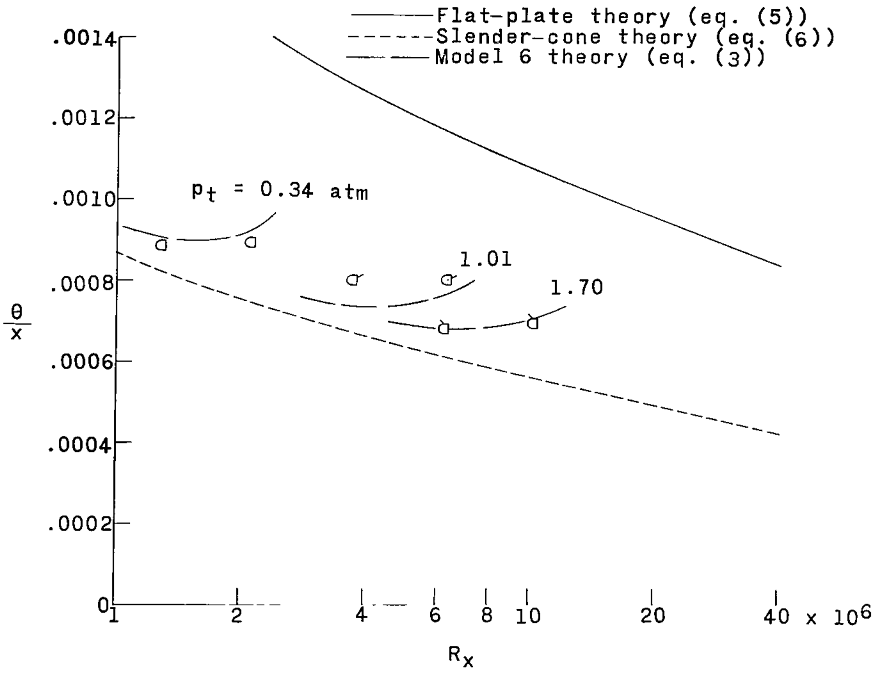

(b) $M_\infty = 2.20$.

Figure 13.- Momentum thickness distribution on model 6 (parabolic arc). Ticks differentiate between the stagnation pressure levels.

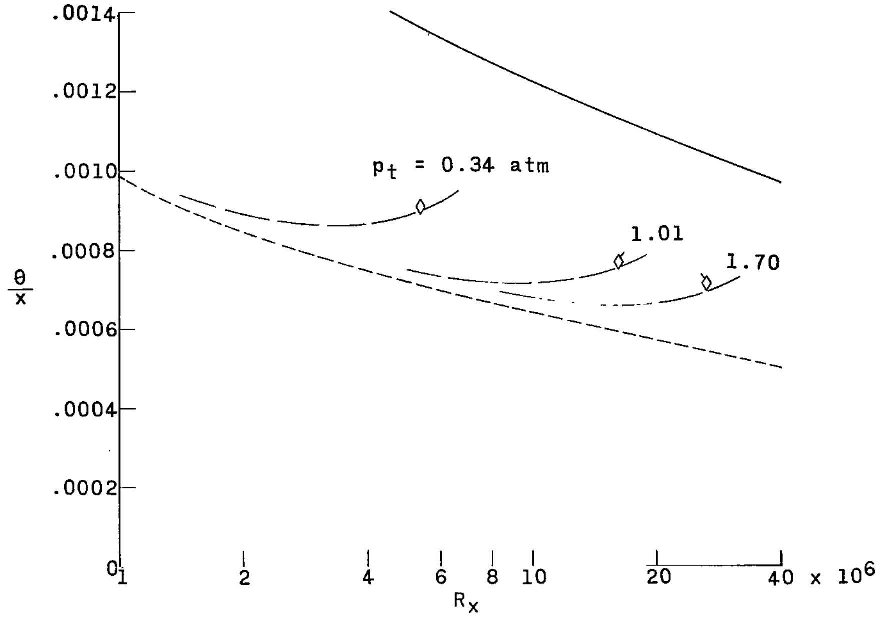

(a) $M_\infty = 1.61$.

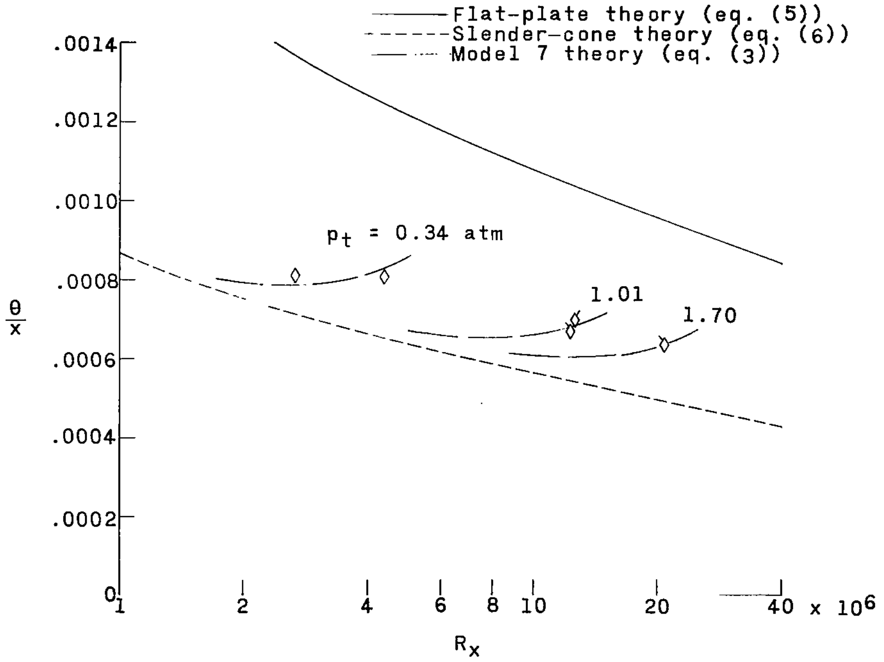

(b) $M_\infty = 2.20$.

Figure 14.- Momentum thickness distribution on model 7 (parabolic arc). Ticks differentiate between the stagnation pressure levels.

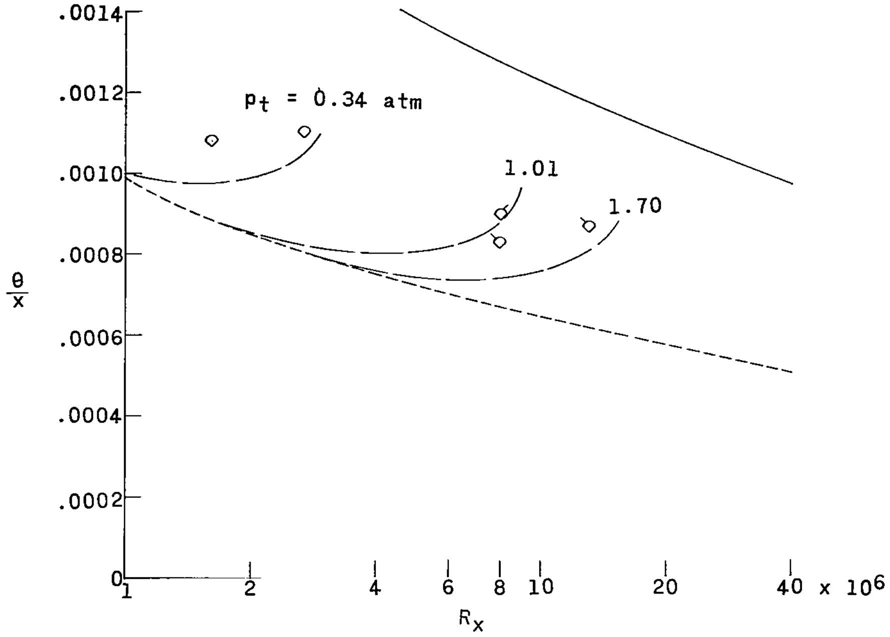

(a) $M_\infty = 1.61$.

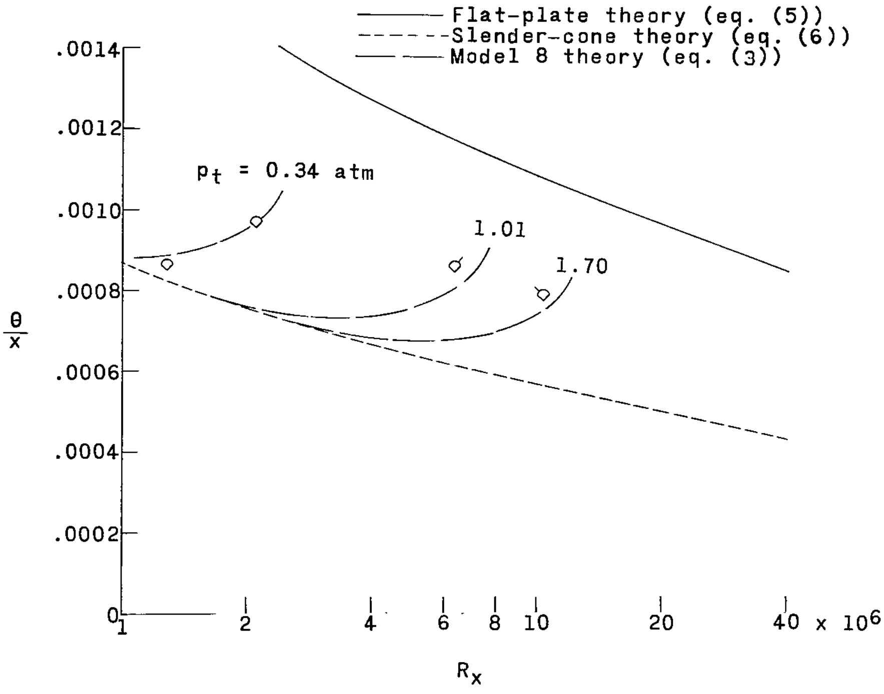

(b) $M_\infty = 2.20$.

Figure 15.- Momentum thickness distribution on model 8 (cone-parabolic arc). Ticks differentiate between the stagnation pressure levels.

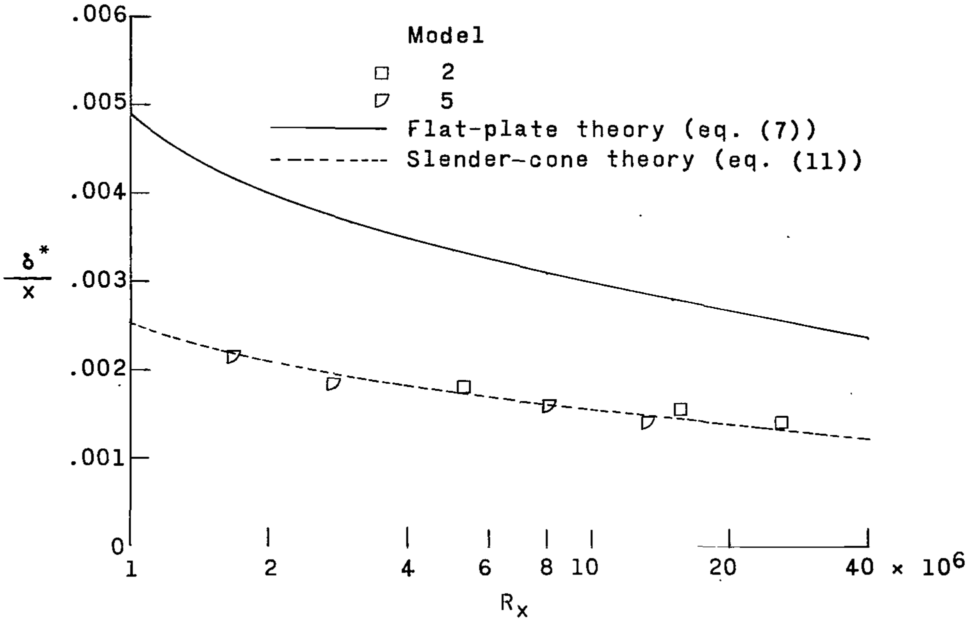

(a) $M_\infty = 1.61.$

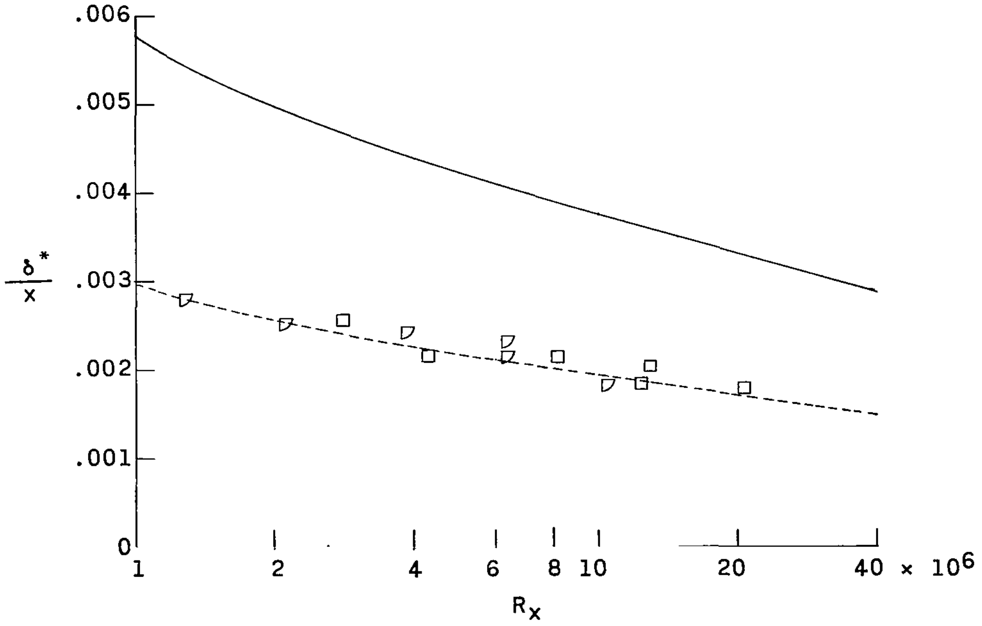

(b) $M_\infty = 2.20.$

Figure 16.- Displacement thickness distributions on models 2 and 5 (slender cones).

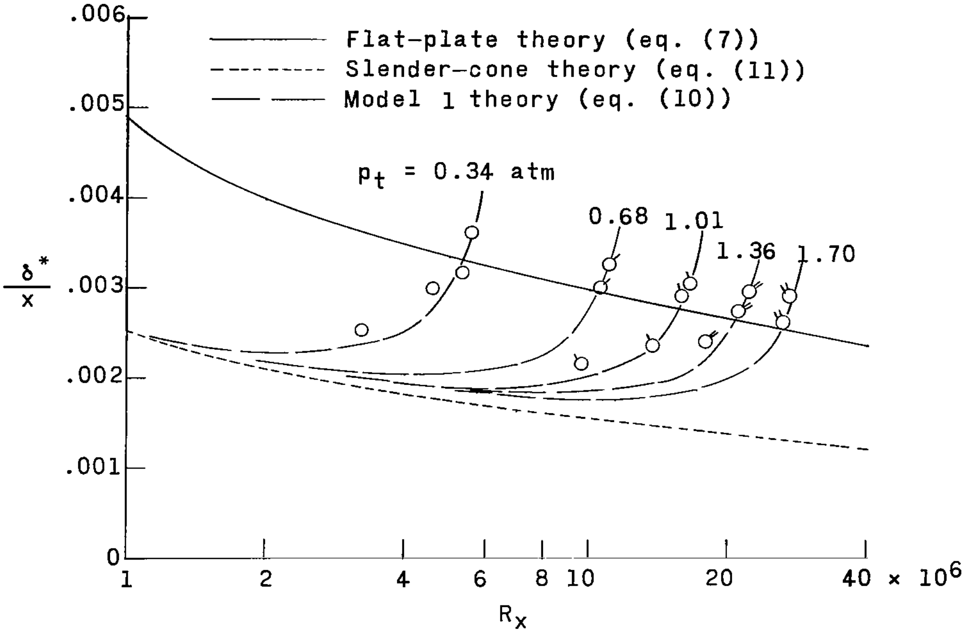

(a) $M_\infty = 1.61$.

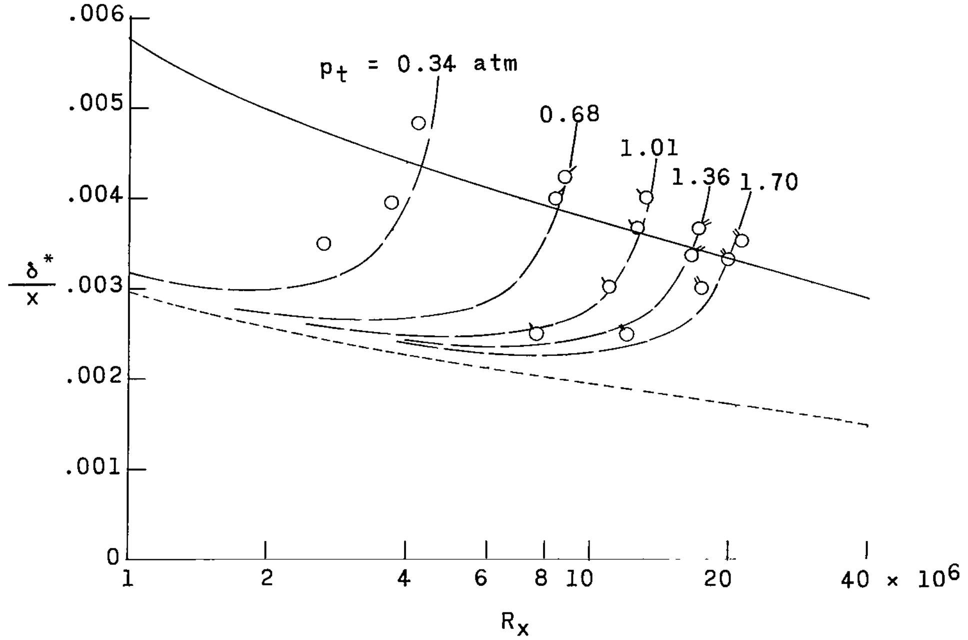

(b) $M_\infty = 2.20$.

Figure 17.- Displacement thickness distribution on model 1 (RM-10). Ticks differentiate between the stagnation pressure levels.

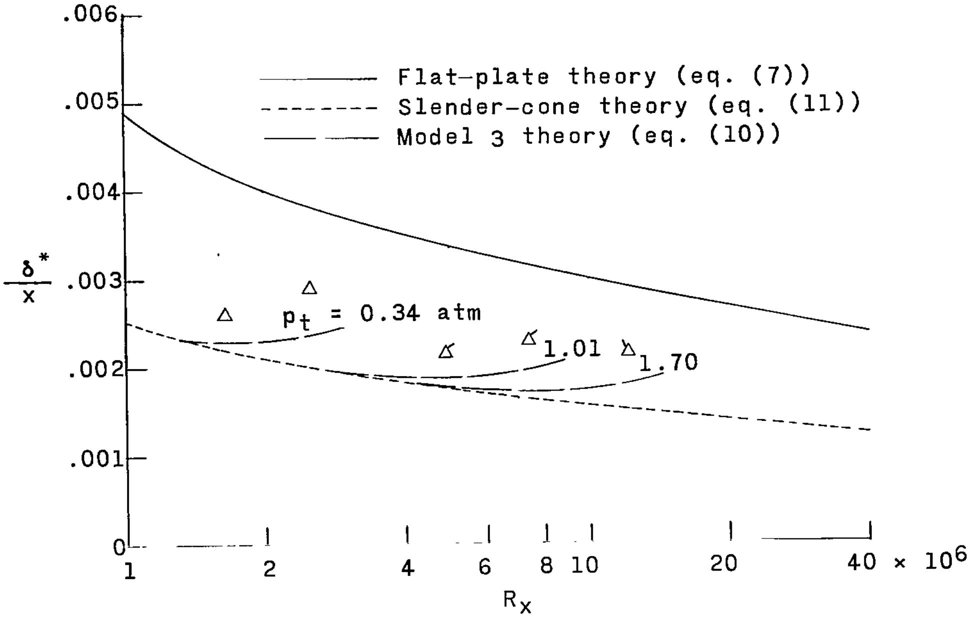

(a) $M_\infty = 1.61.$

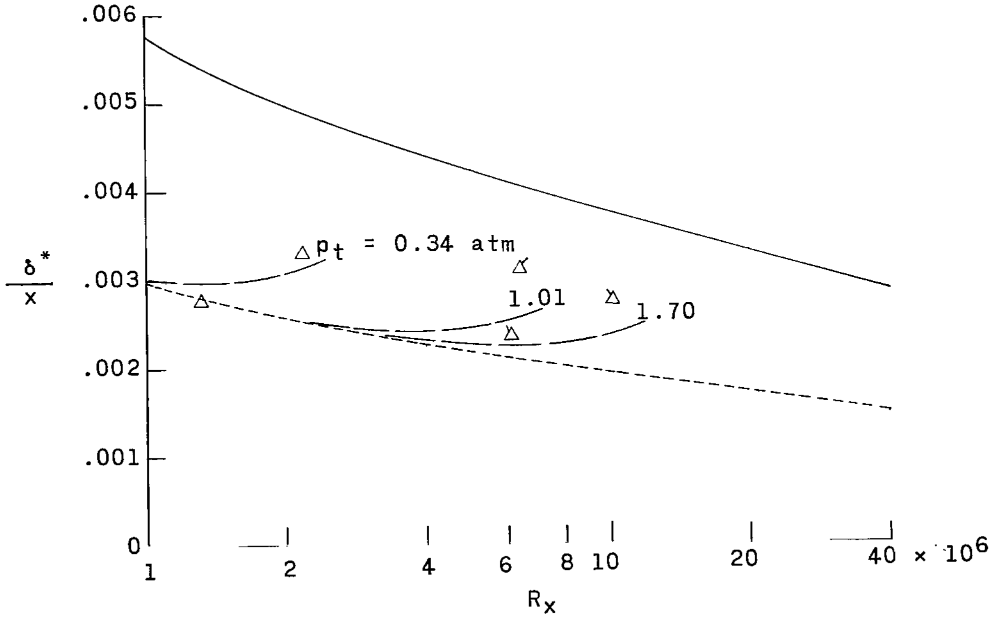

(b) $M_\infty = 2.20.$

Figure 18.- Displacement thickness distribution on model 3 (cone-parabolic arc). Ticks differentiate between the stagnation pressure levels.

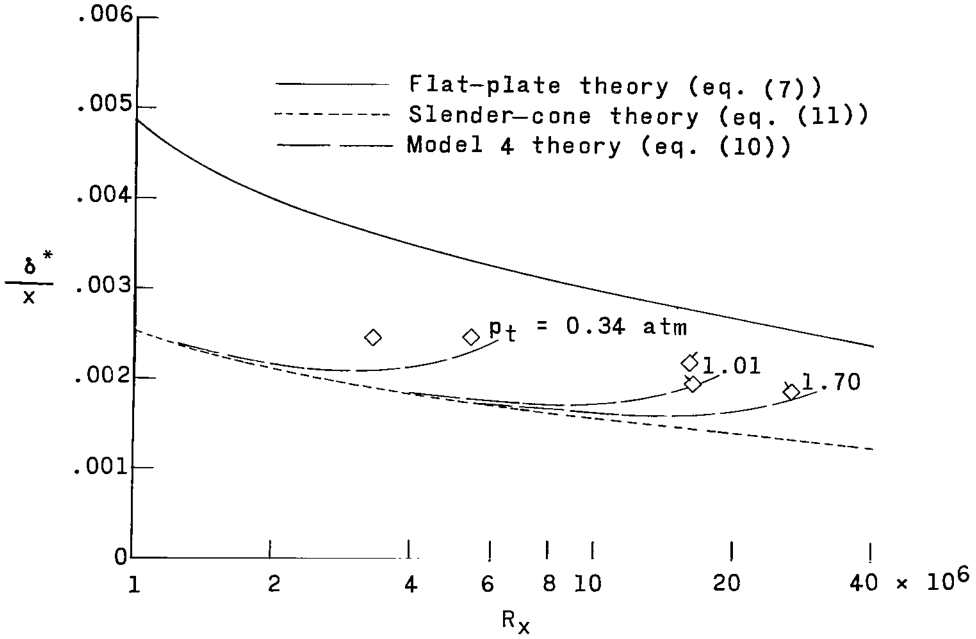

(a) $M_\infty = 1.61$.

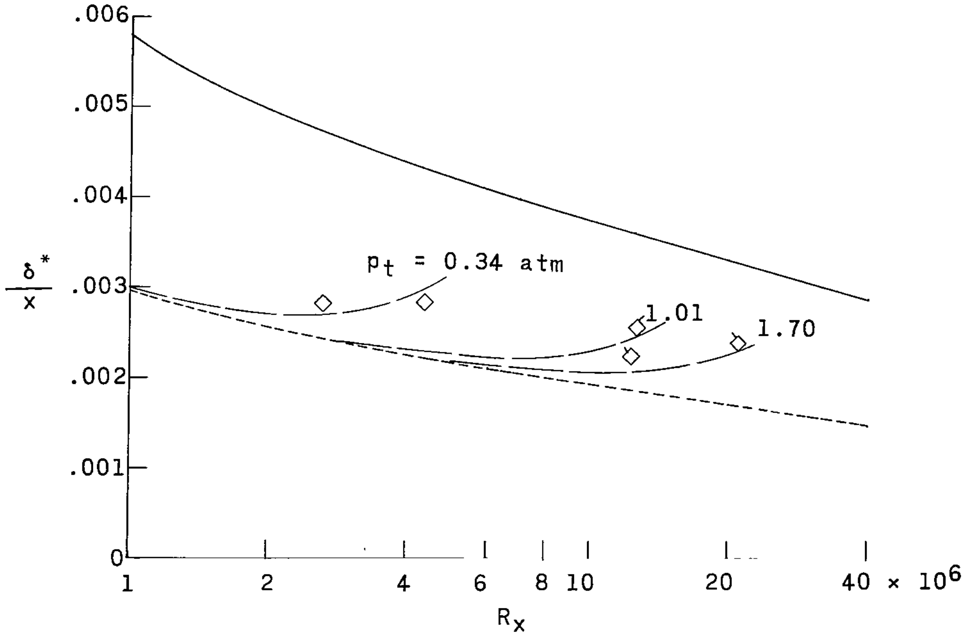

(b) $M_\infty = 2.20$.

Figure 19.- Displacement thickness distribution on model 4 (cone-parabolic arc). Ticks differentiate between the stagnation pressure levels.

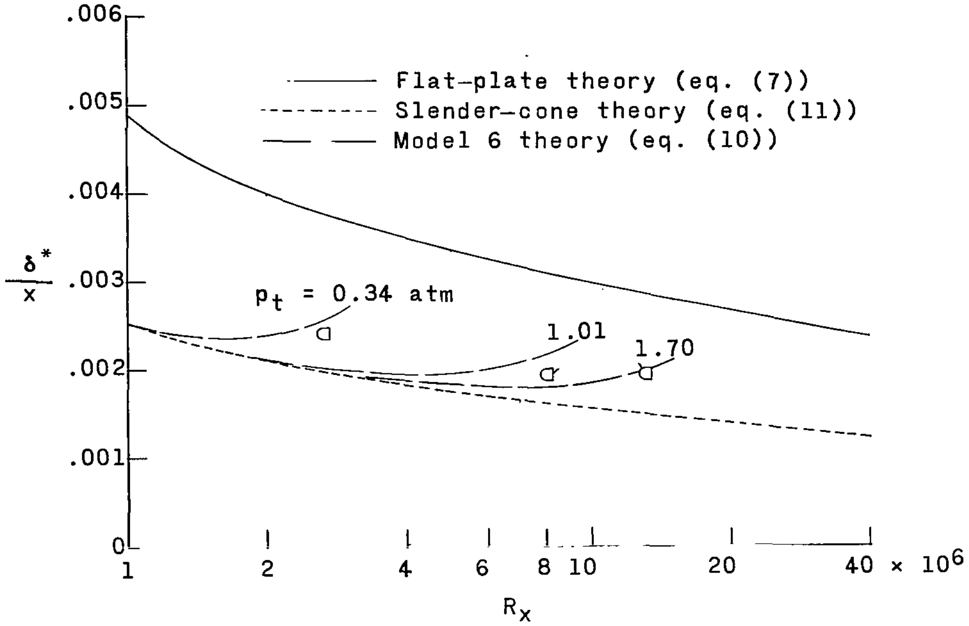

(a) $M_\infty = 1.61$.

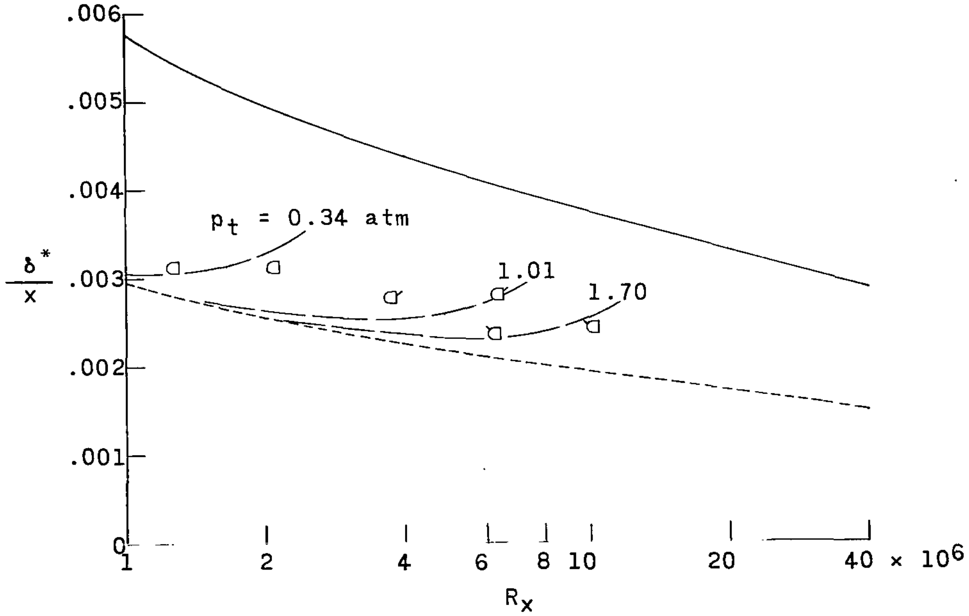

(b) $M_\infty = 2.20$.

Figure 20.- Displacement thickness distribution on model 6 (parabolic arc). Ticks differentiate between the stagnation pressure levels.

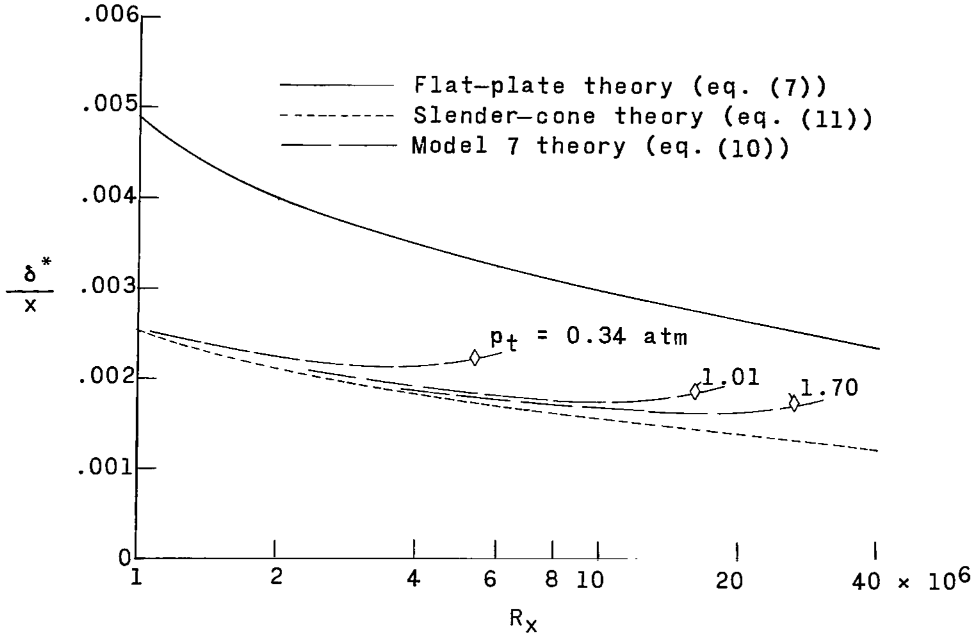

(a) $M_\infty = 1.61$.

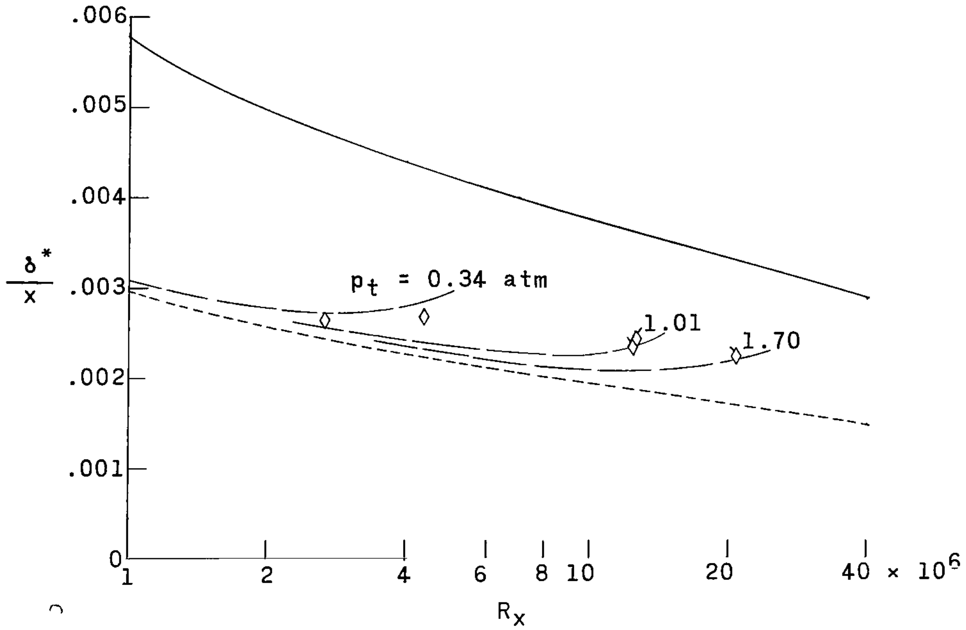

(b) $M_\infty = 2.20$.

Figure 21.- Displacement thickness distribution on model 7 (parabolic arc). Ticks differentiate between the stagnation pressure levels.

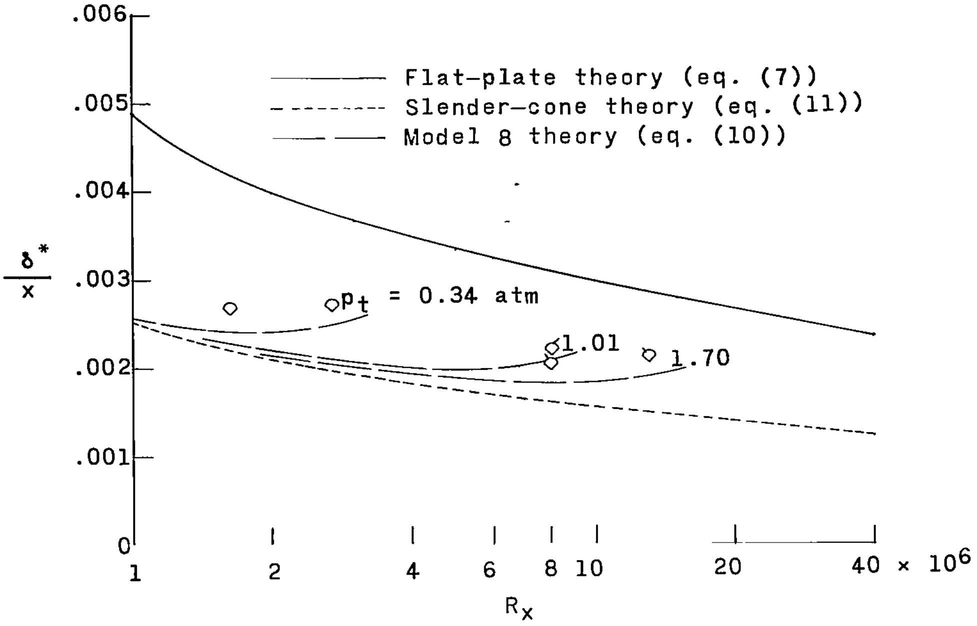

(a) M_∞ = 1.61.

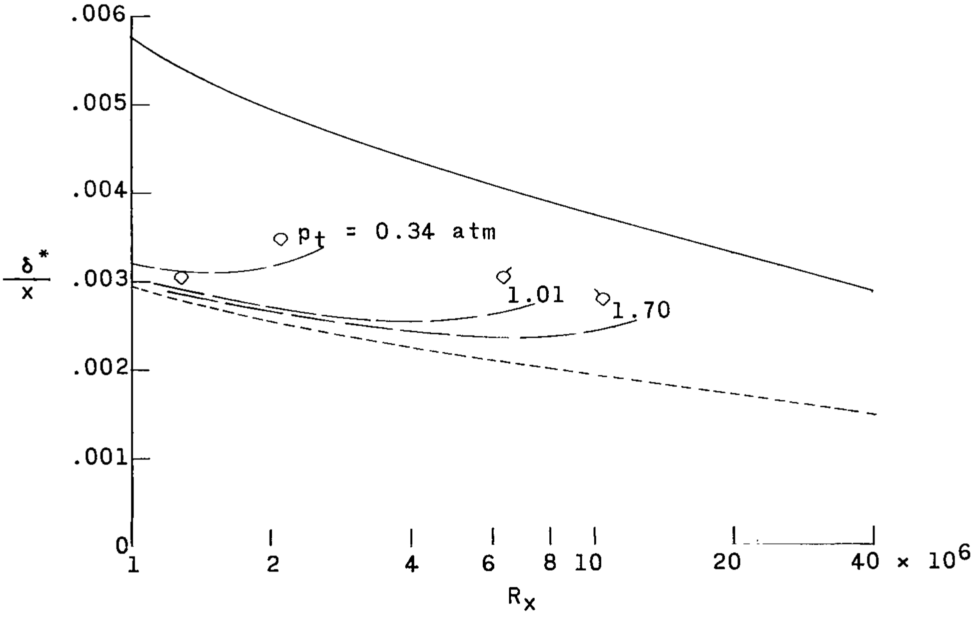

(b) M_∞ = 2.20.

Figure 22.- Displacement thickness distribution on model 8 (cone-parabolic arc). Ticks differentiate between the stagnation pressure levels.

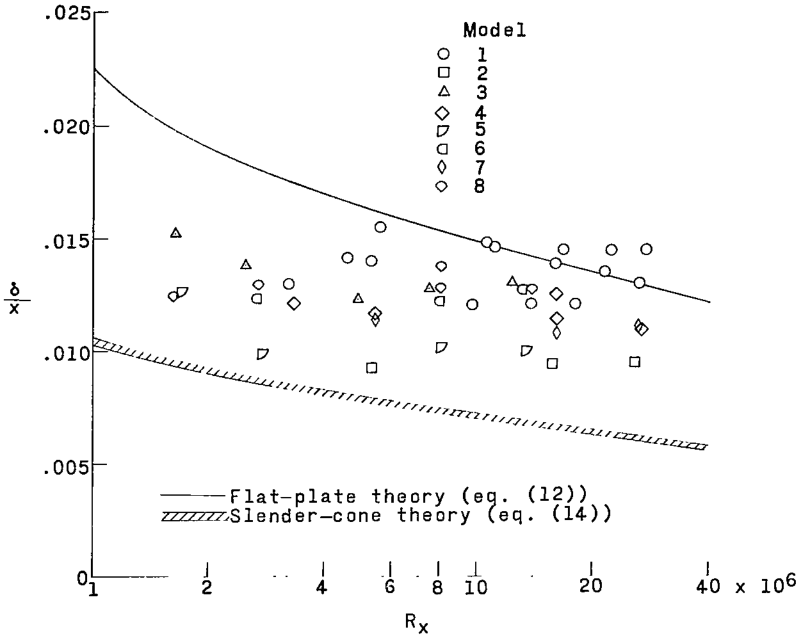

(a) $M_\infty = 1.61$.

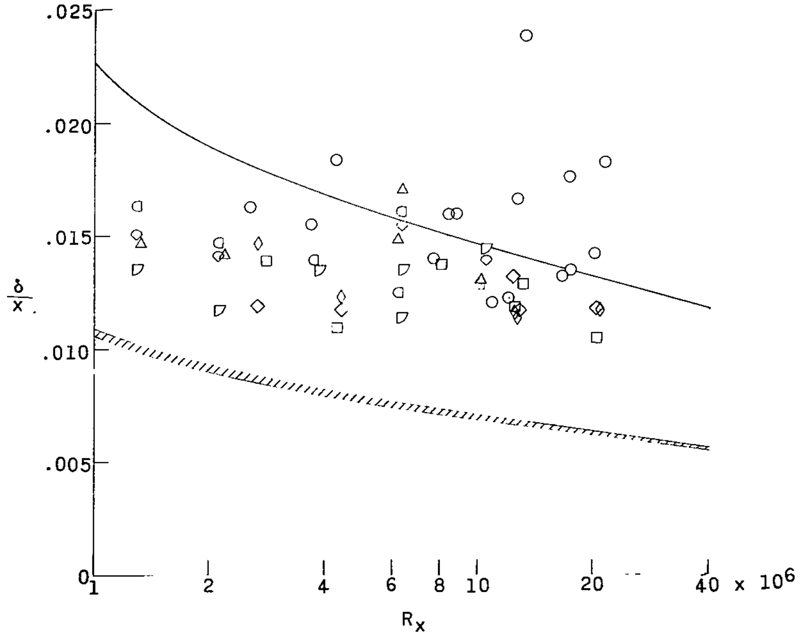

(b) $M_\infty = 2.20$.

Figure 23.- Boundary-layer thickness distribution.

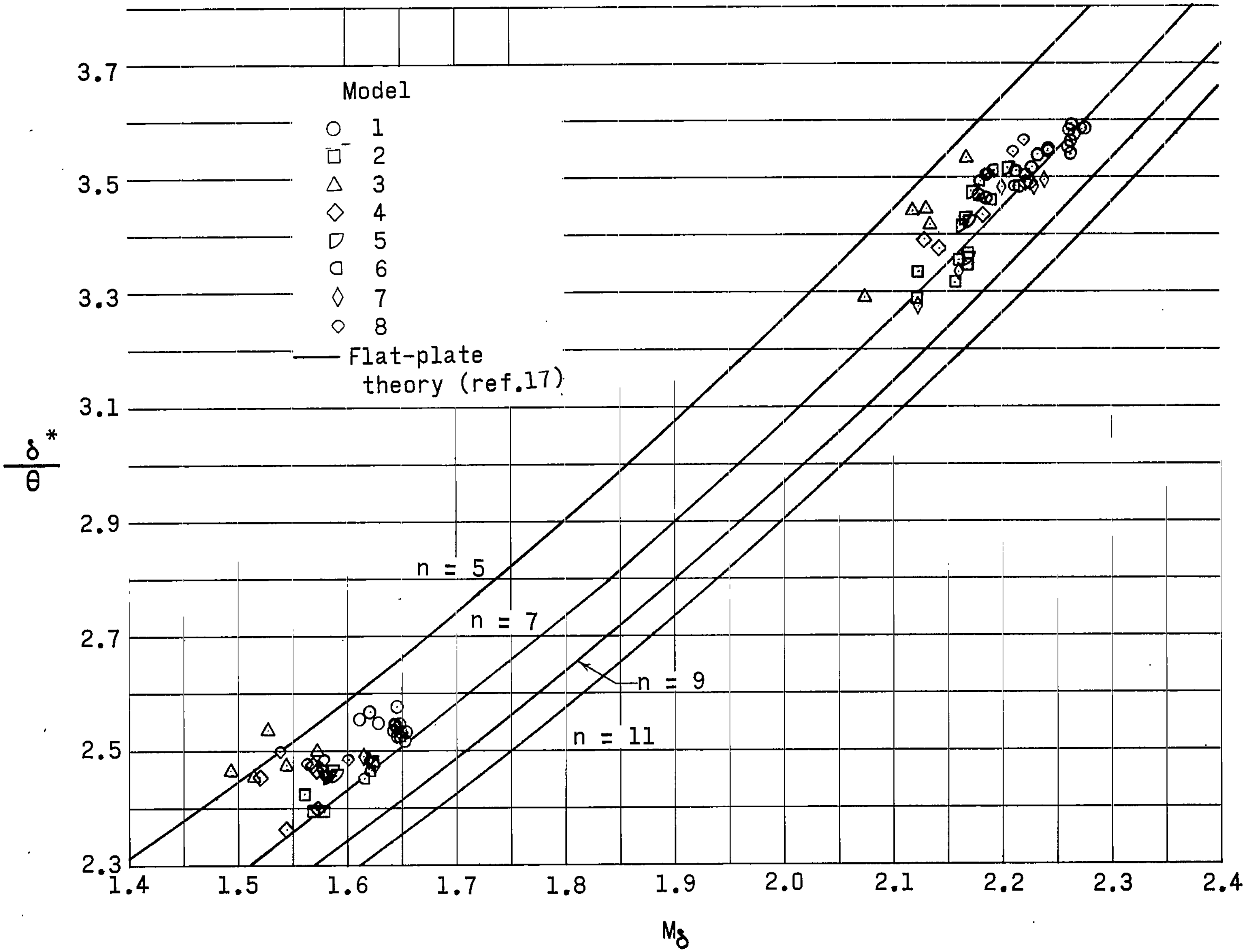

Figure 24.- Variation of δ^*/θ with M_δ.

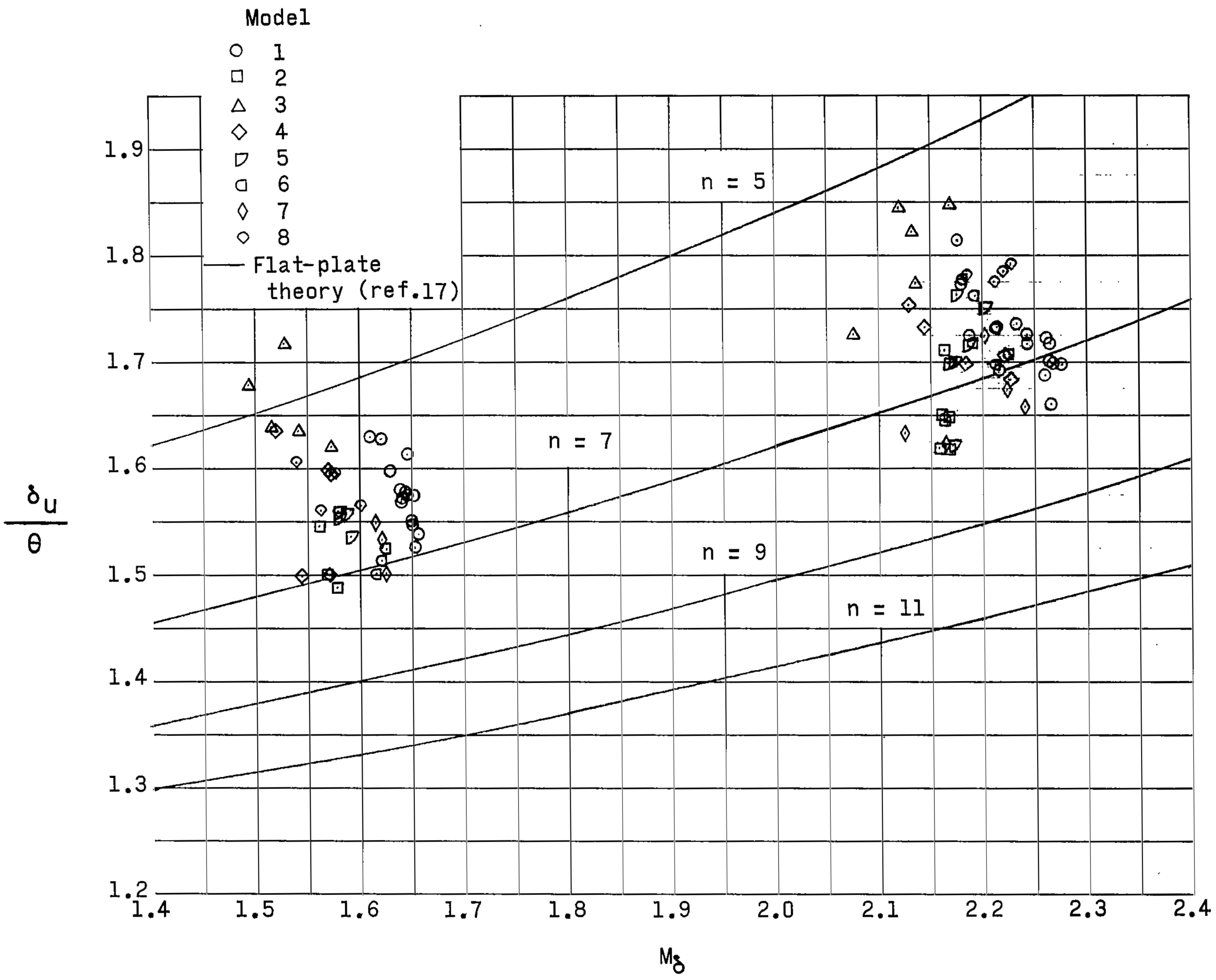

Figure 25.- Variation of δ_u/θ with M_δ.

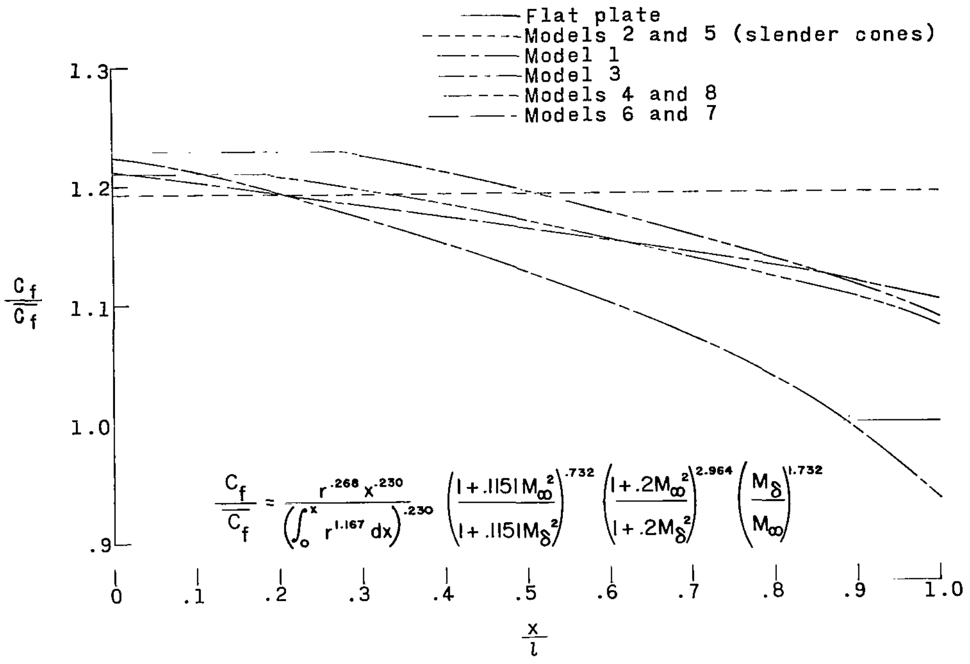

(a) $M_\infty = 1.61$.

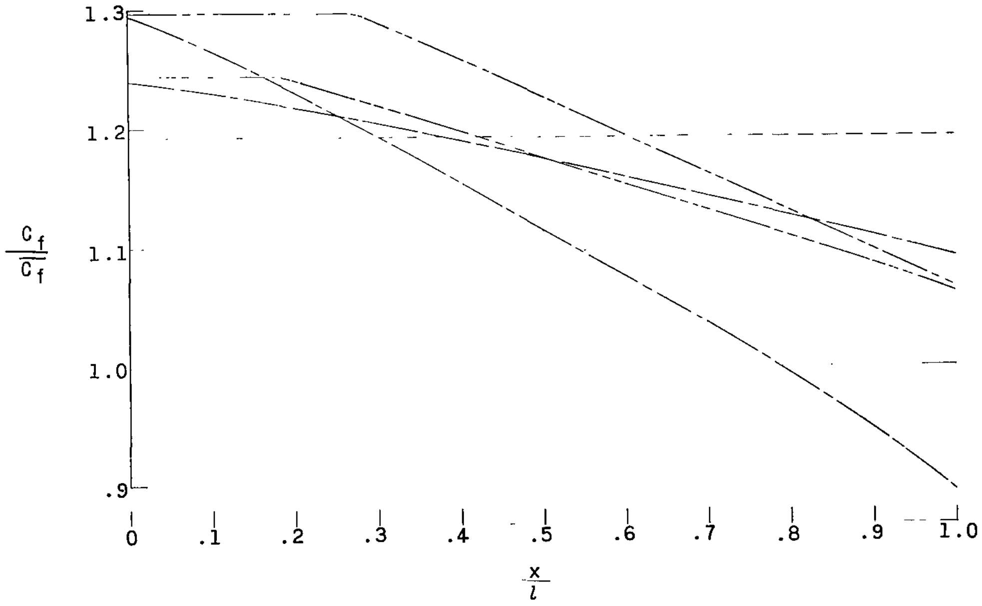

(b) $M_\infty = 2.20$.

Figure 26.- Theoretical local skin-friction-coefficient ratios calculated by equation (18).

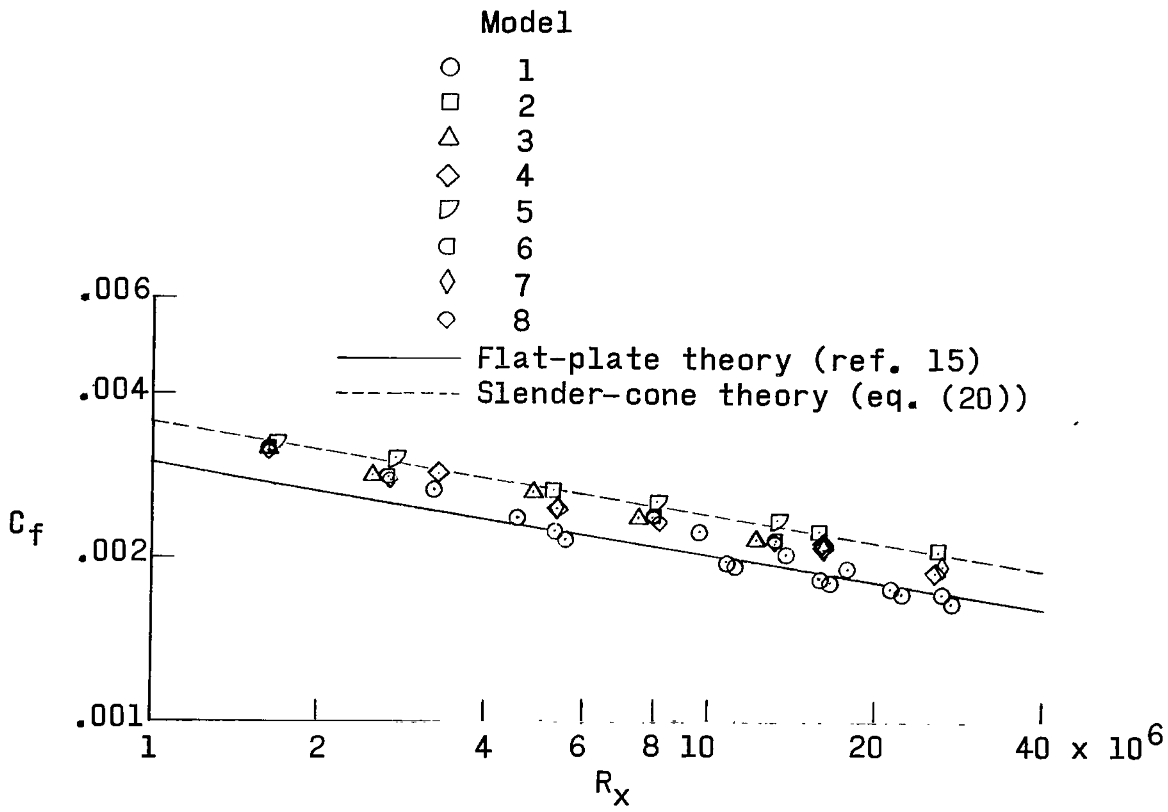

(a) $M_\infty = 1.61$.

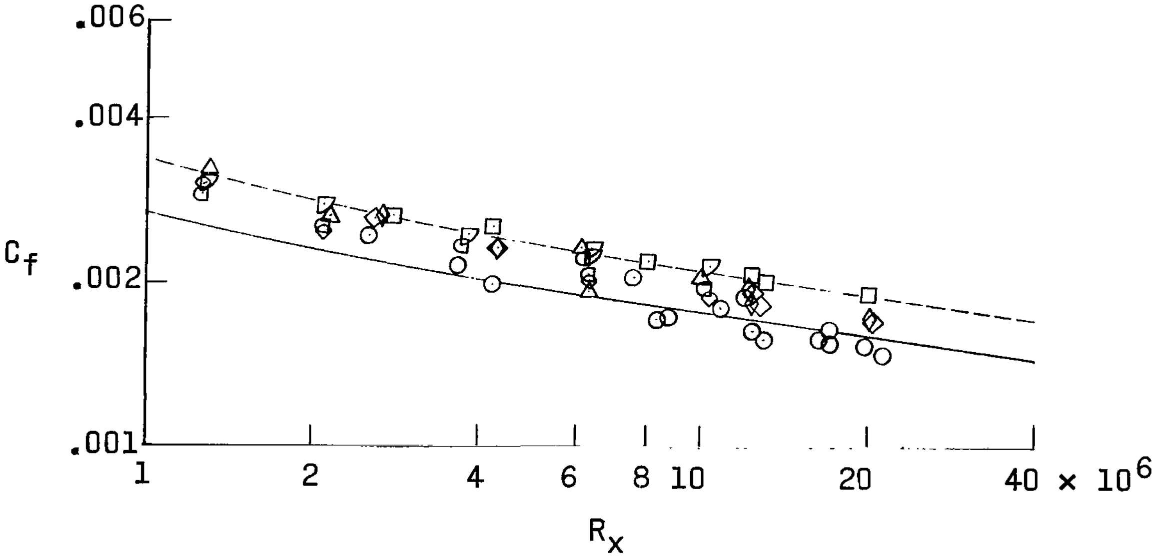

(b) $M_\infty = 2.20$.

Figure 27.- Summary of local skin-friction-coefficient data.

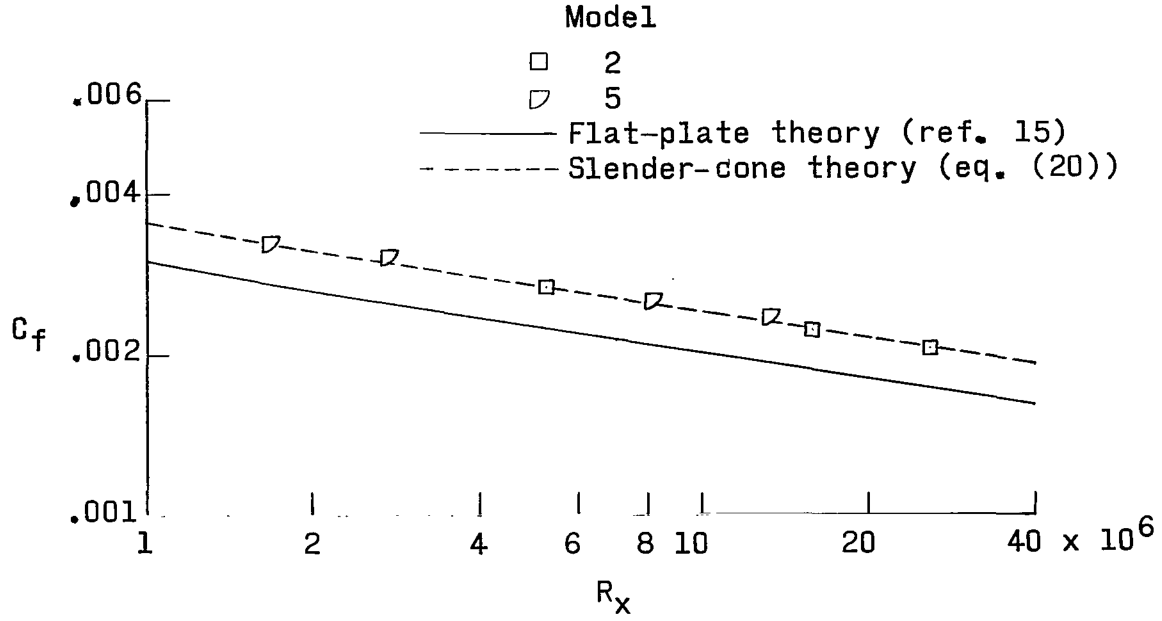

(a) $M_\infty = 1.61$.

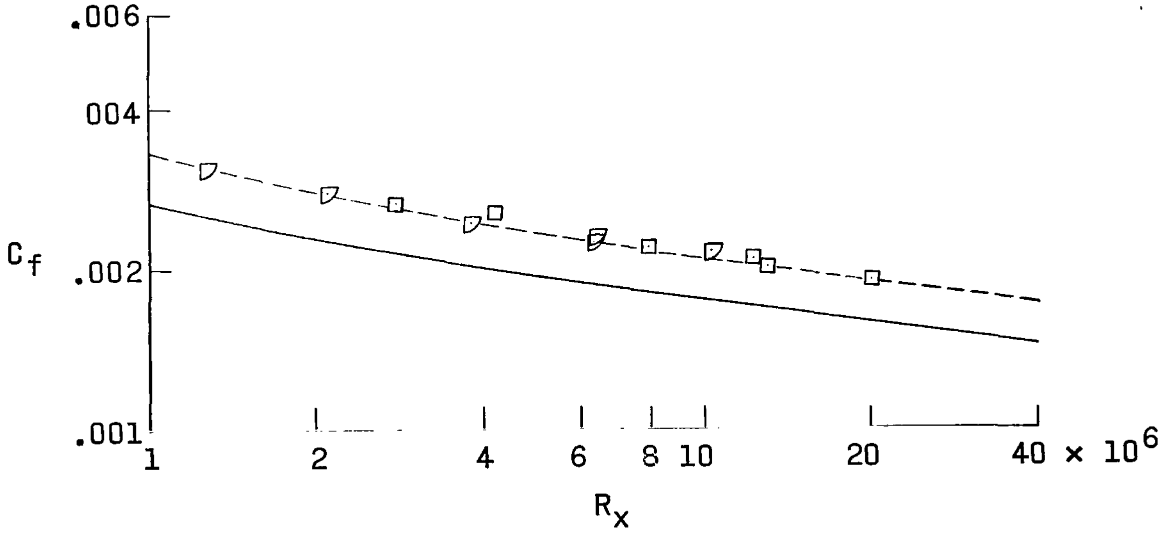

(b) $M_\infty = 2.20$.

Figure 28.- Local skin-friction-coefficient distributions on models 2 and 5 (slender cones).

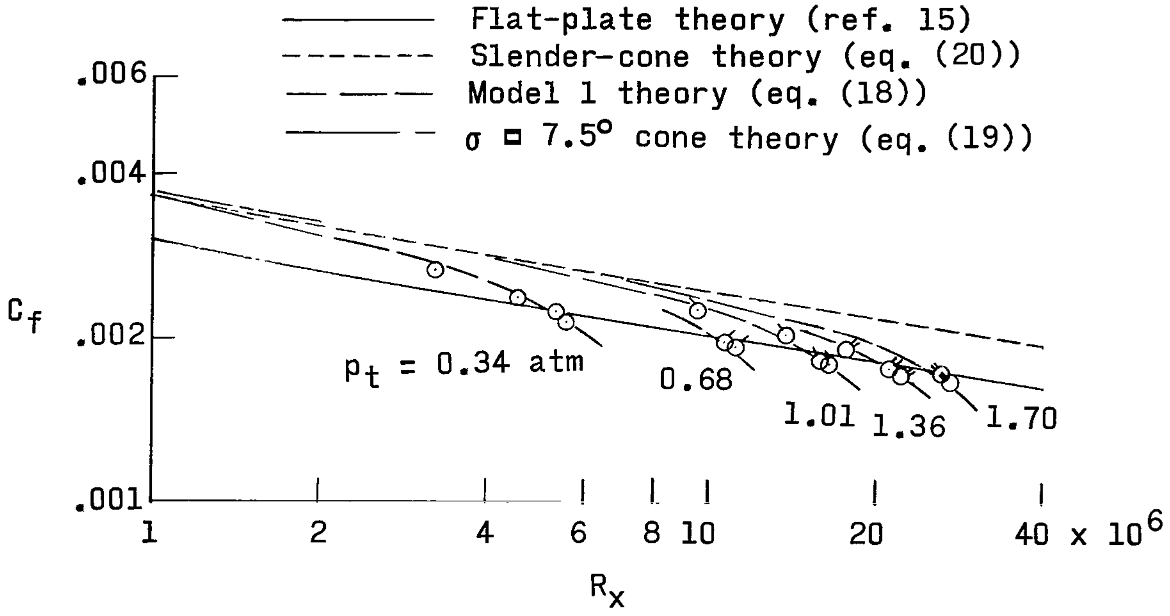

(a) $M_\infty = 1.61$.

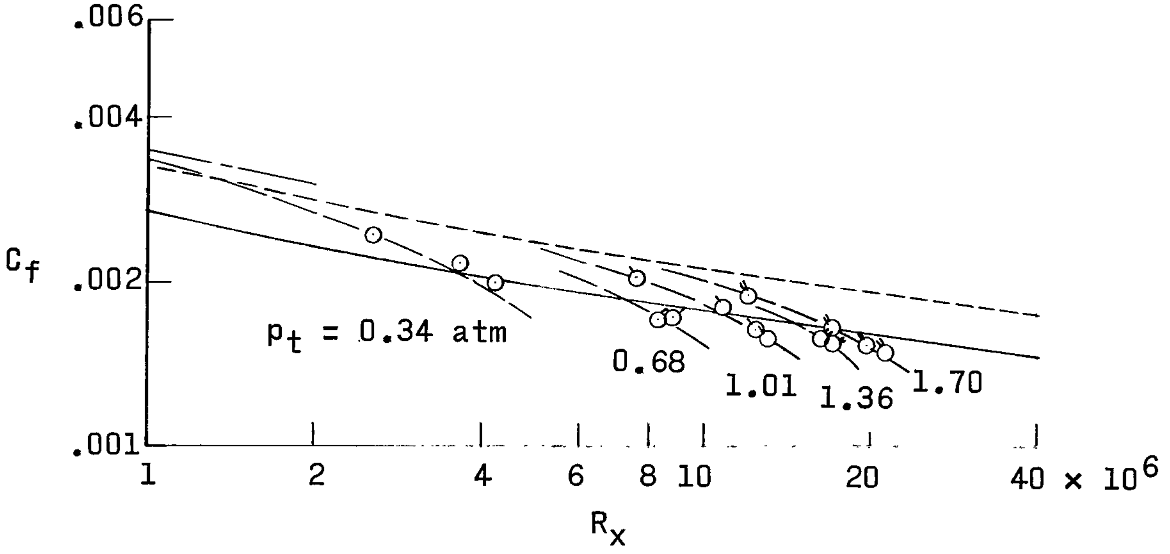

(b) $M_\infty = 2.20$.

Figure 29.- Local skin-friction-coefficient distribution on model 1 (RM-10). Ticks differentiate between the stagnation pressure levels.

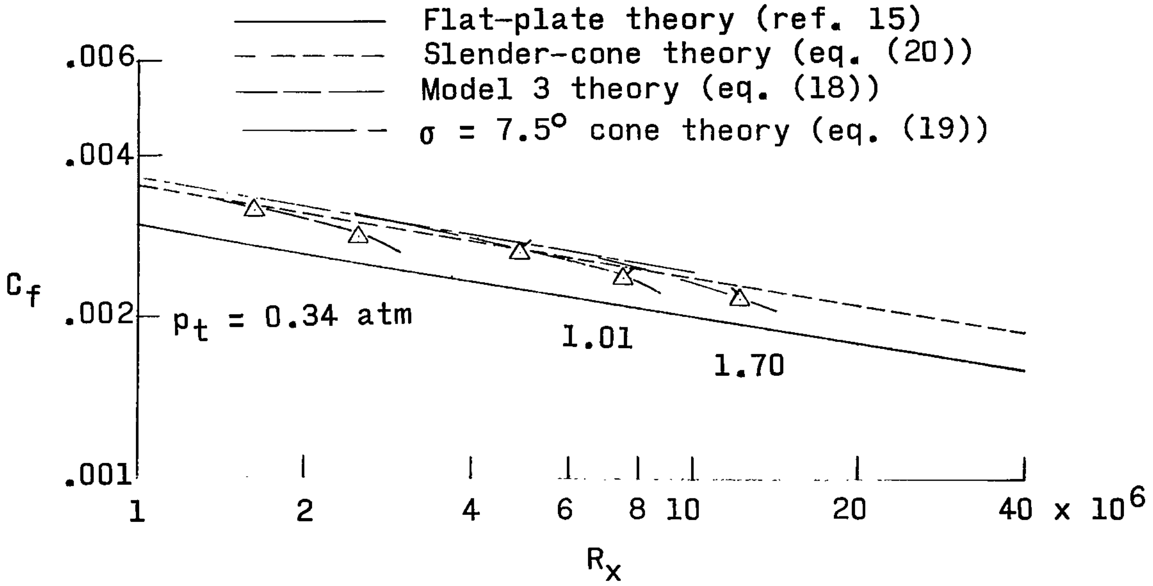

(a) $M_\infty = 1.61$.

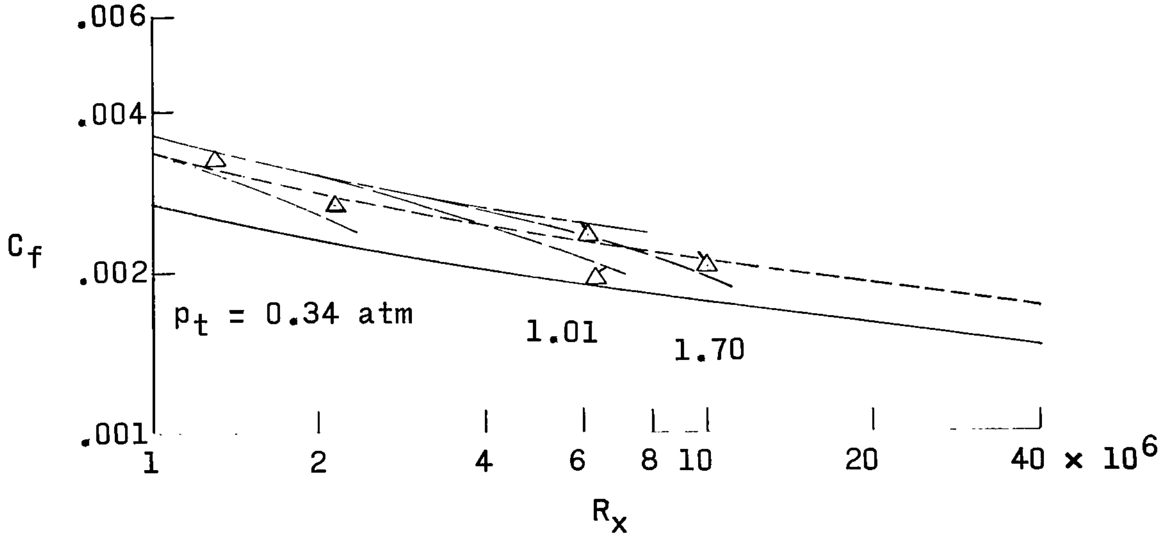

(b) $M_\infty = 2.20$.

Figure 30.- Local skin-friction-coefficient distribution on model 3 (cone-parabolic arc). Ticks differentiate between the stagnation pressure levels.

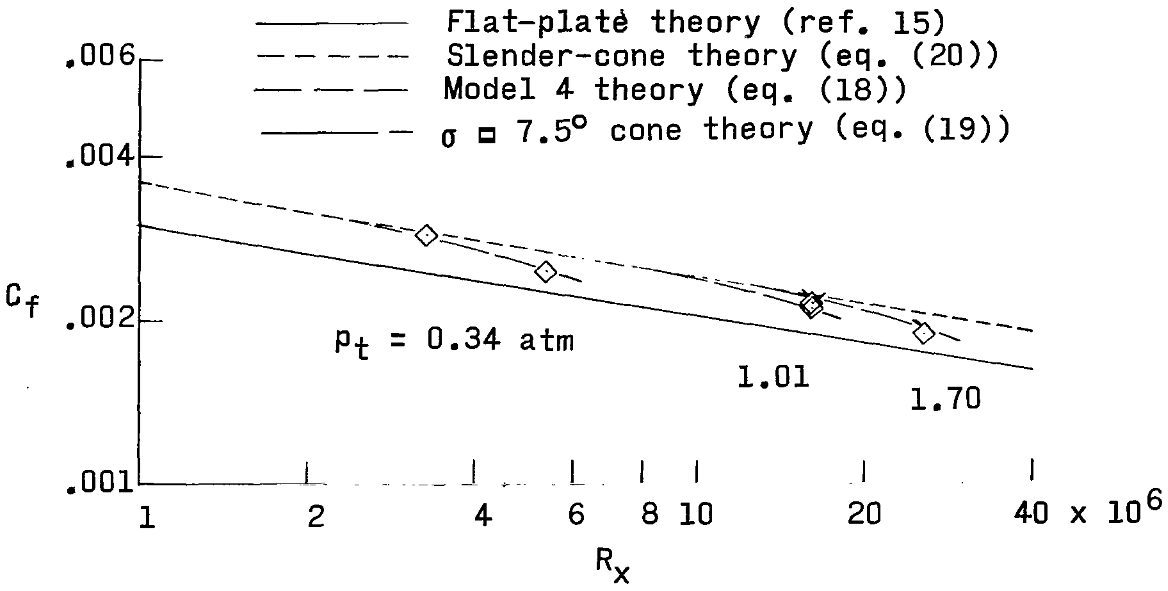

(a) $M_\infty = 1.61$.

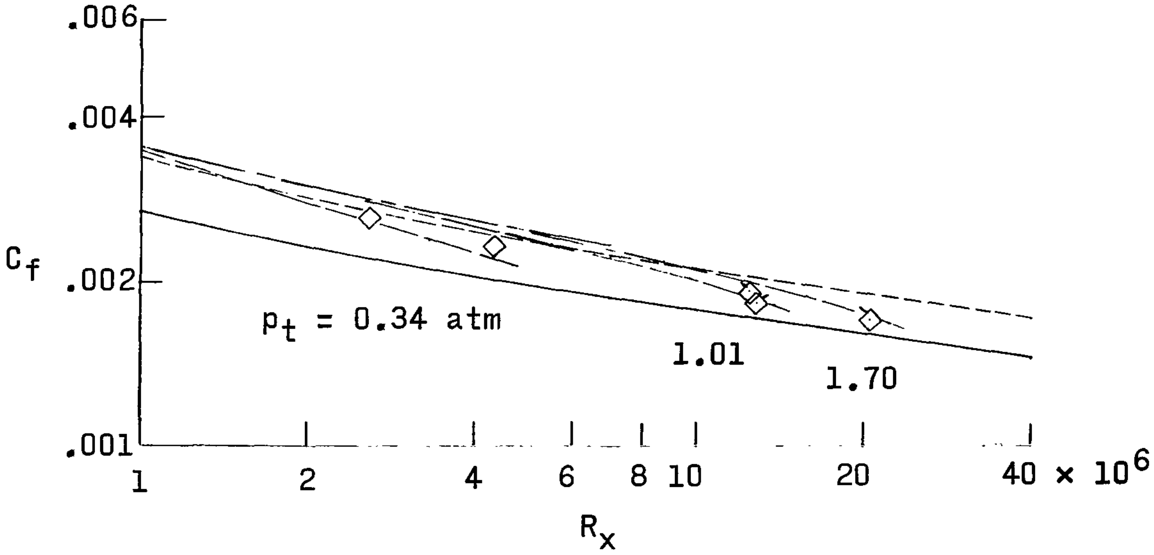

(b) $M_\infty = 2.20$.

Figure 31.- Local skin-friction-coefficient distribution on model 4 (cone-parabolic arc). Ticks differentiate between the stagnation pressure levels.

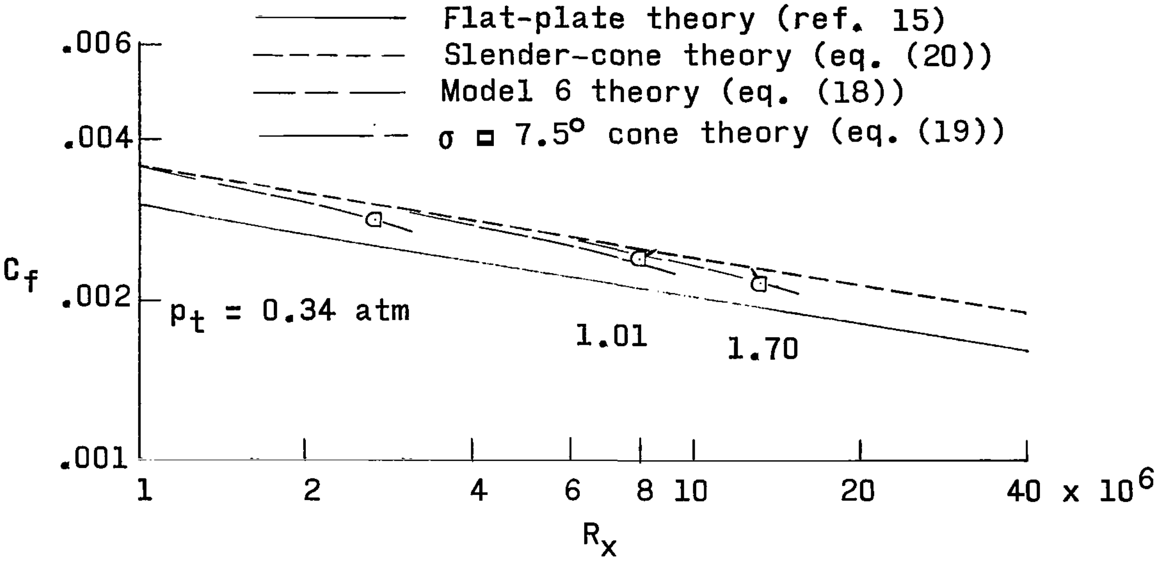

(a) $M_\infty = 1.61$.

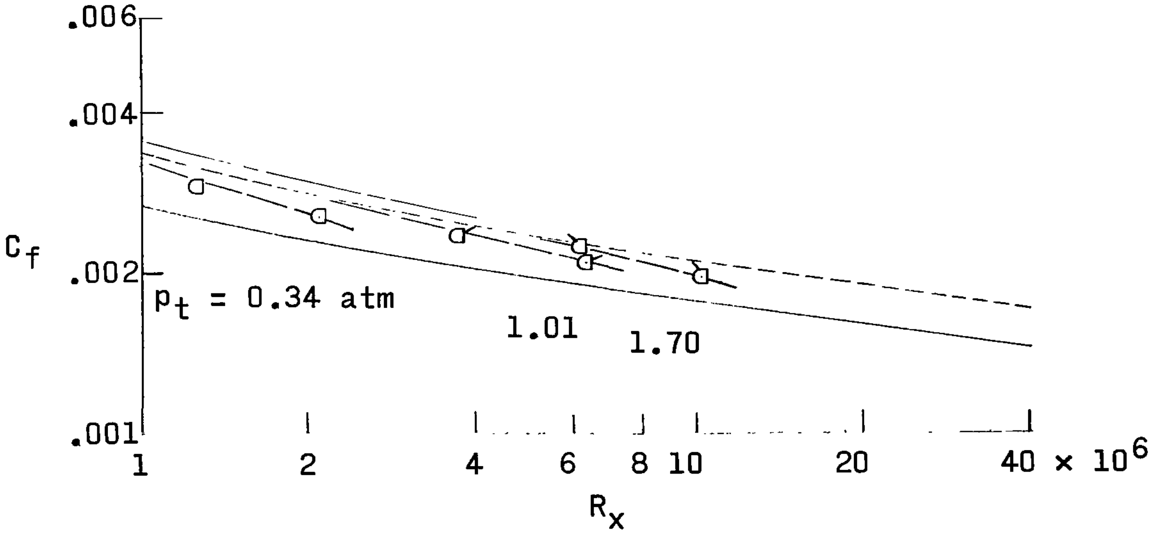

(b) $M_\infty = 2.20$.

Figure 32.- Local skin-friction-coefficient distribution on model 6 (parabolic arc). Ticks differentiate between the stagnation pressure levels.

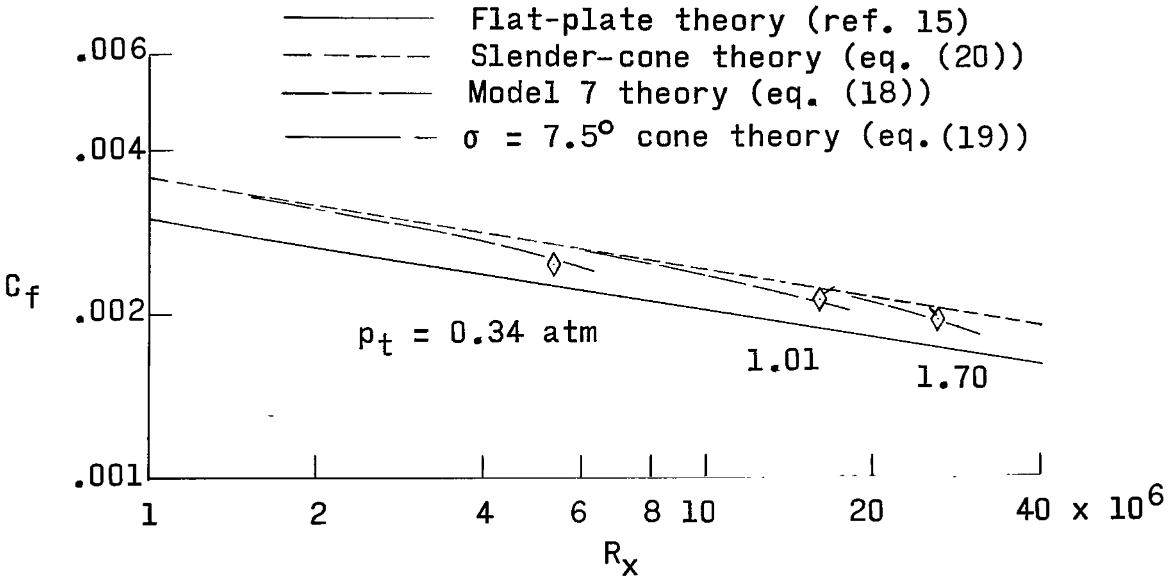

(a) $M_\infty = 1.61$.

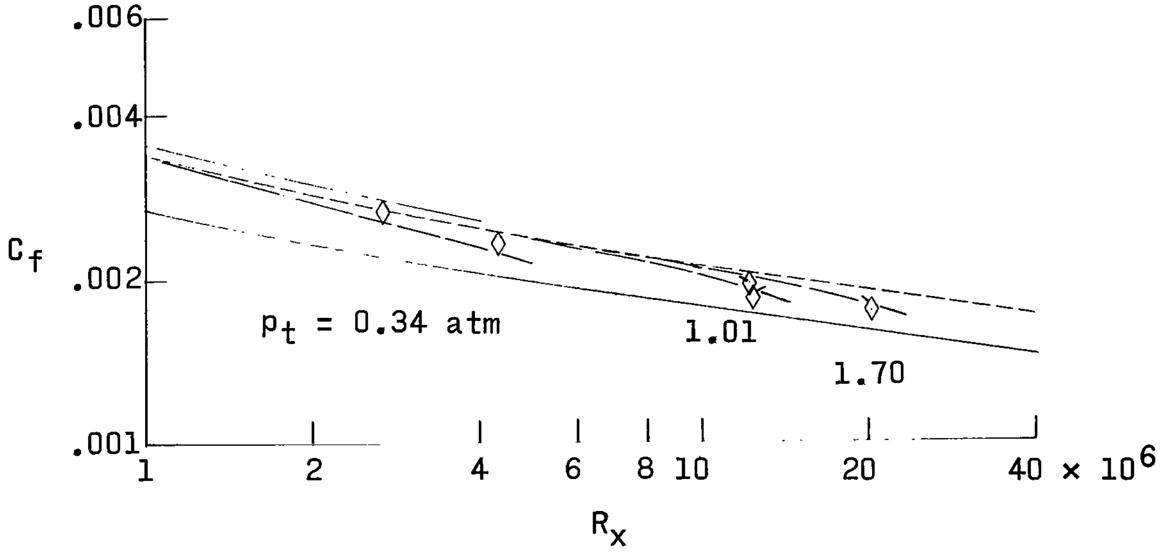

(b) $M_\infty = 2.20$.

Figure 33.- Local skin-friction-coefficient distribution on model 7 (parabolic arc). Ticks differentiate between the stagnation pressure levels.

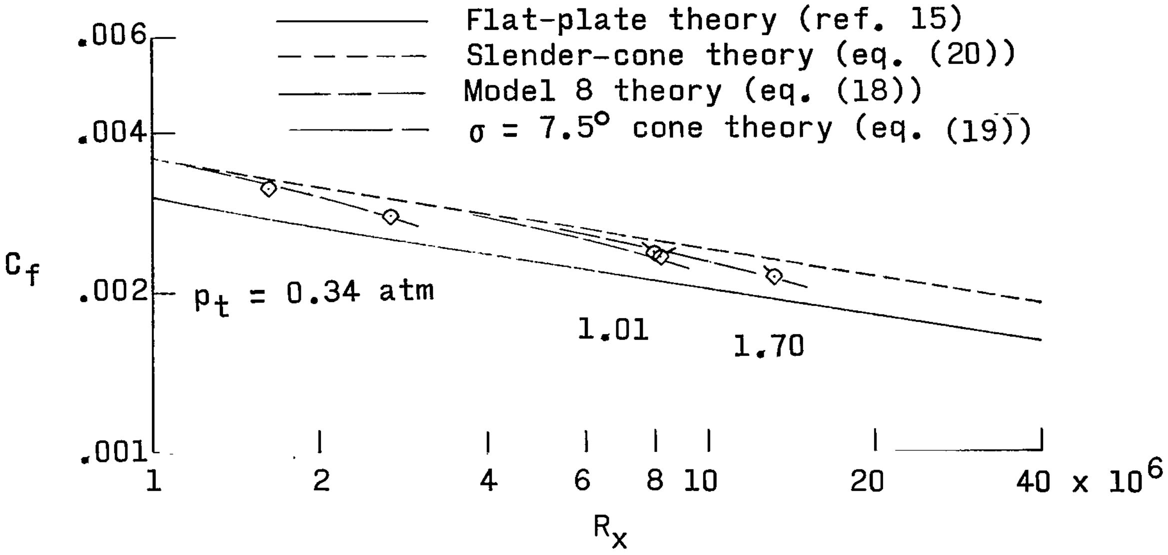

(a) $M_\infty = 1.61$.

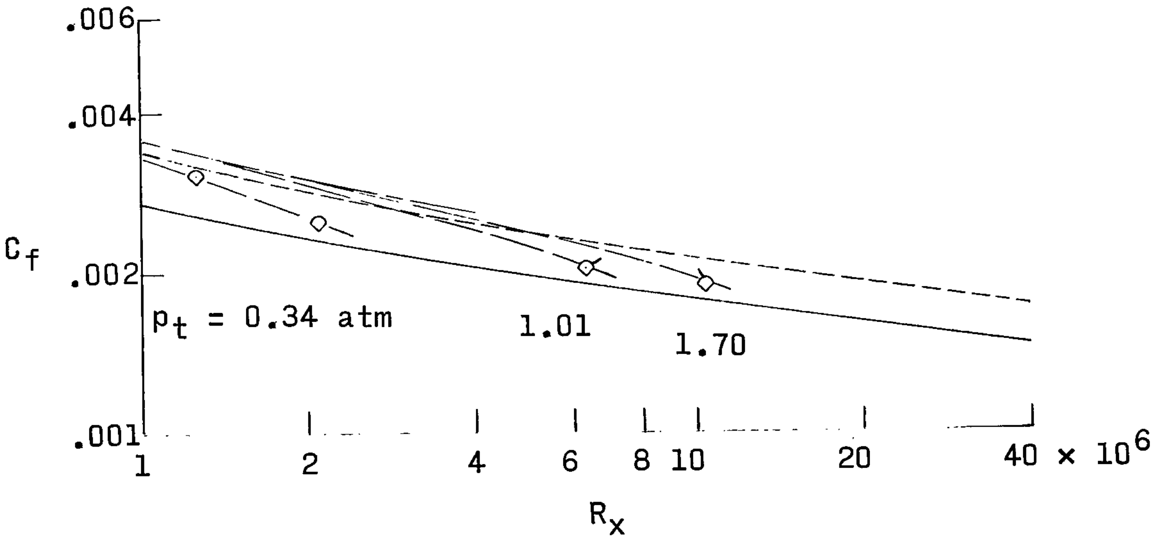

(b) $M_\infty = 2.20$.

Figure 34.- Local skin-friction-coefficient distribution on model 8 (cone-parabolic arc). Ticks differentiate between the stagnation pressure levels.

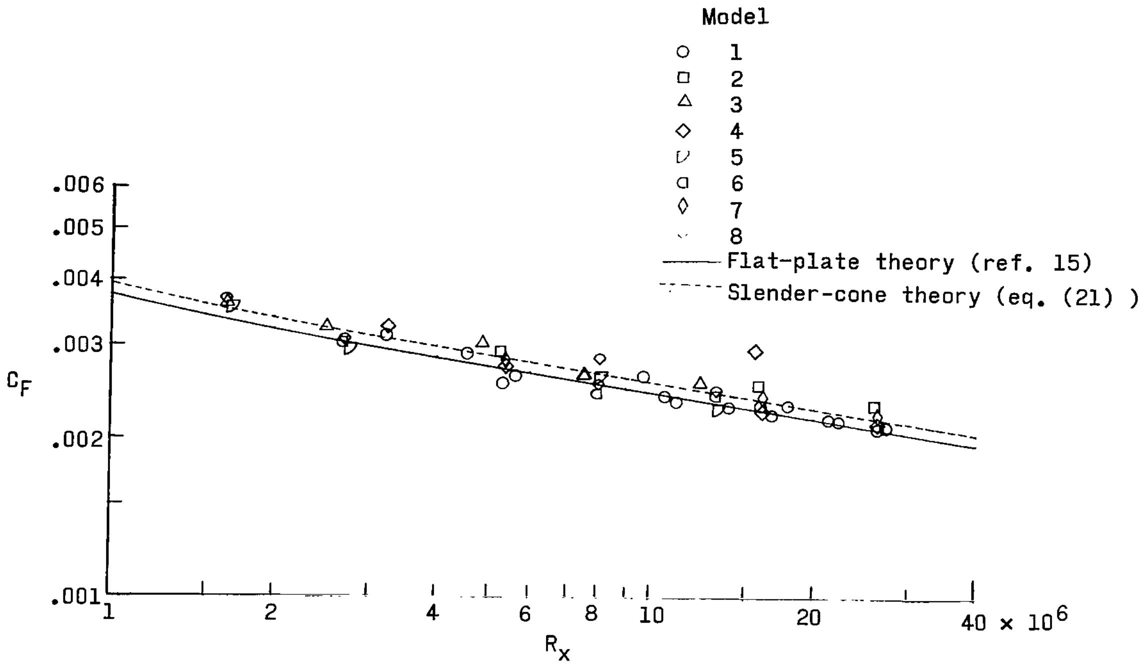

(a) $M_\infty = 1.61$.

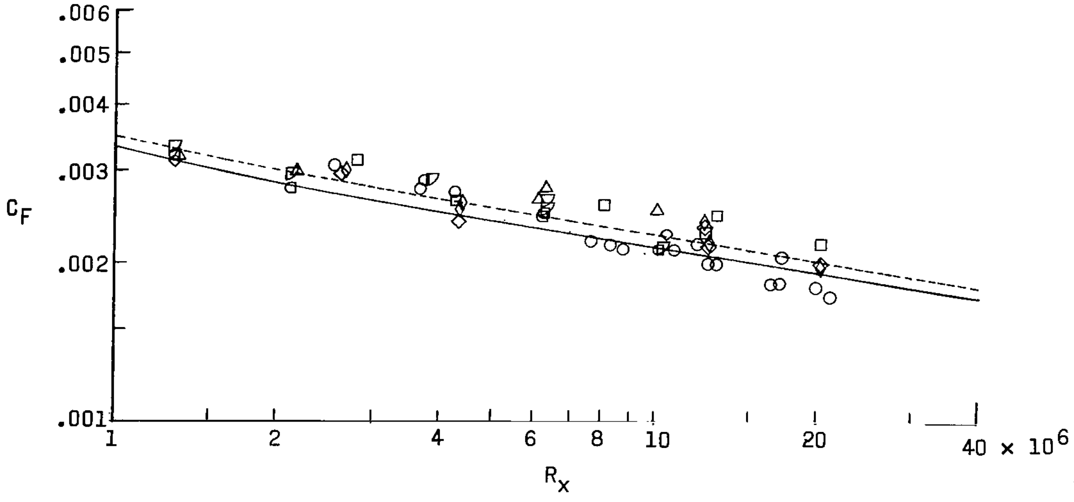

(b) $M_\infty = 2.20$.

Figure 35.- Variation of average skin-friction coefficient with free-stream Reynolds number.

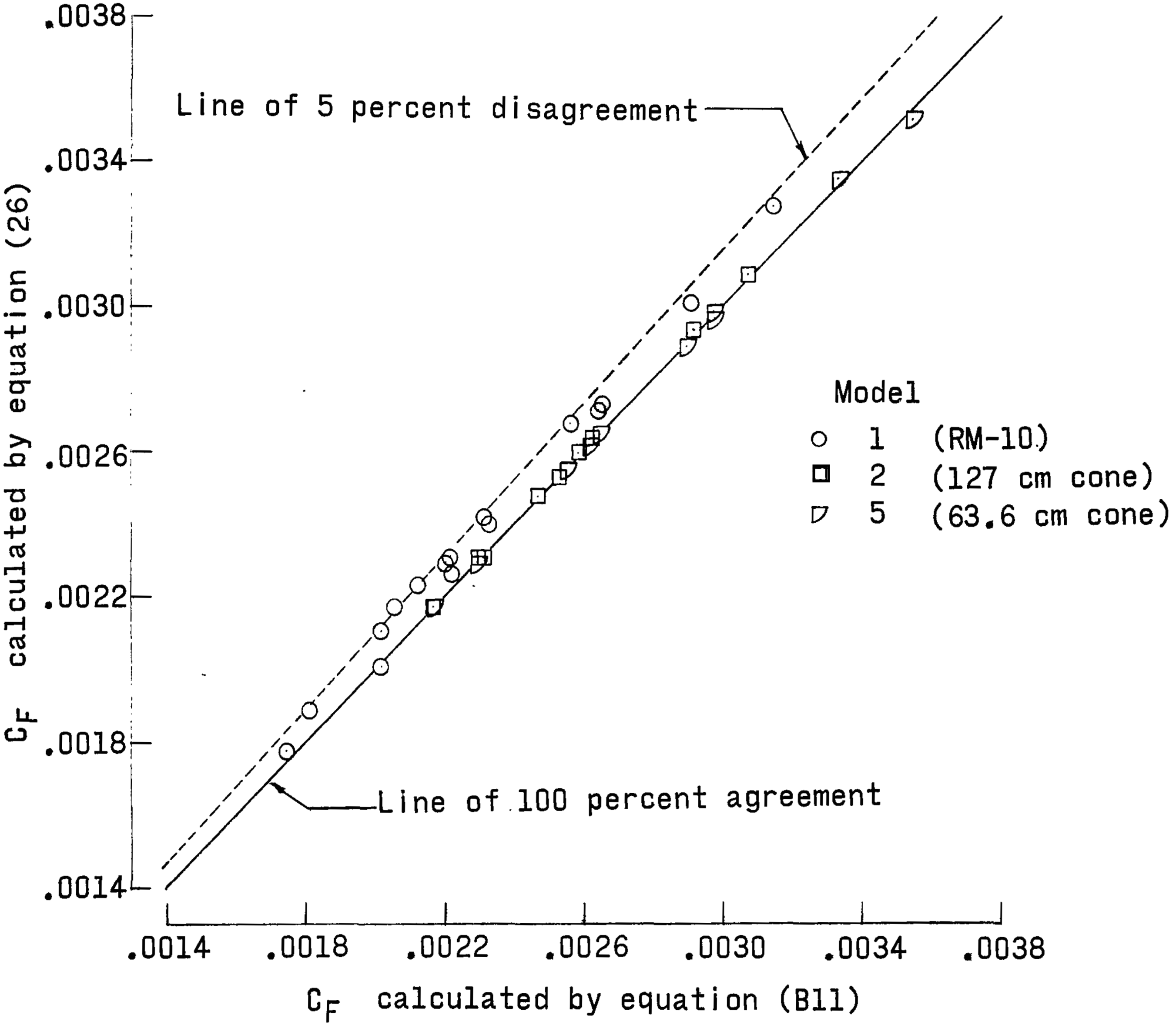

Figure 36.- Comparison of methods of calculating average skin-friction coefficient.

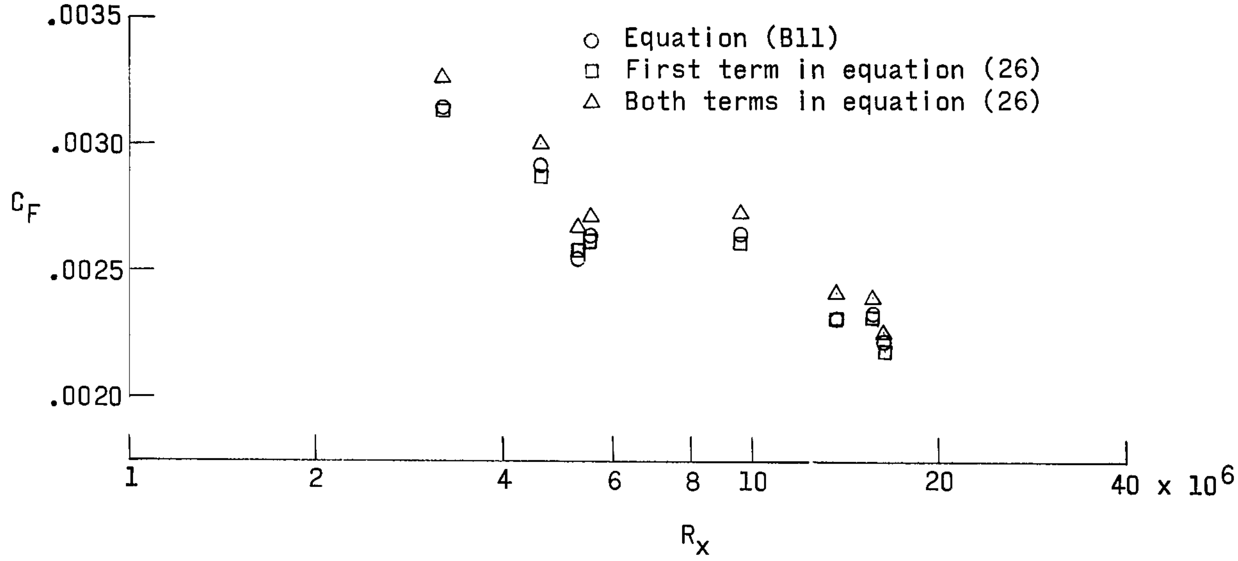

(a) $M_\infty = 1.61$.

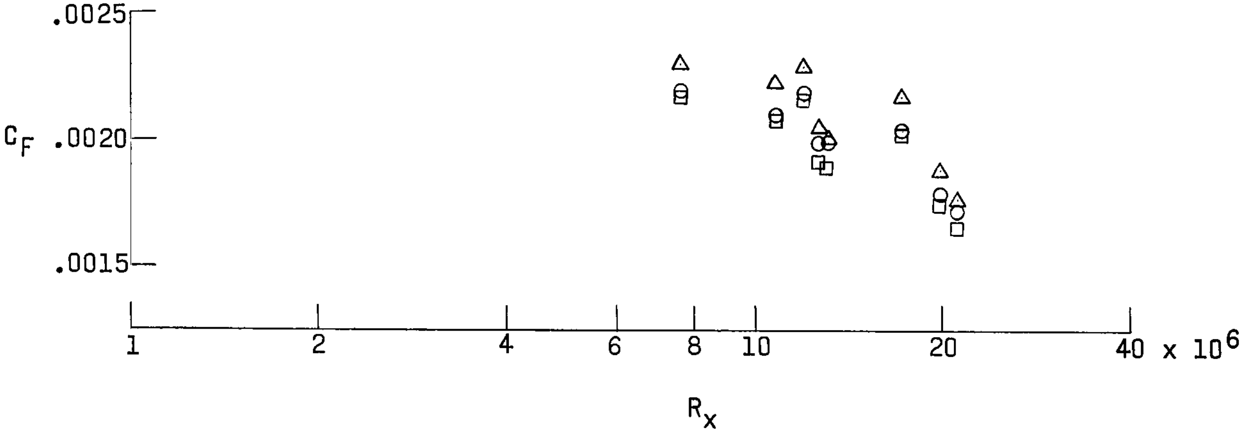

(b) $M_\infty = 2.20$.

Figure 37.- Contributors to average skin-friction coefficient on model 1 (RM-10).

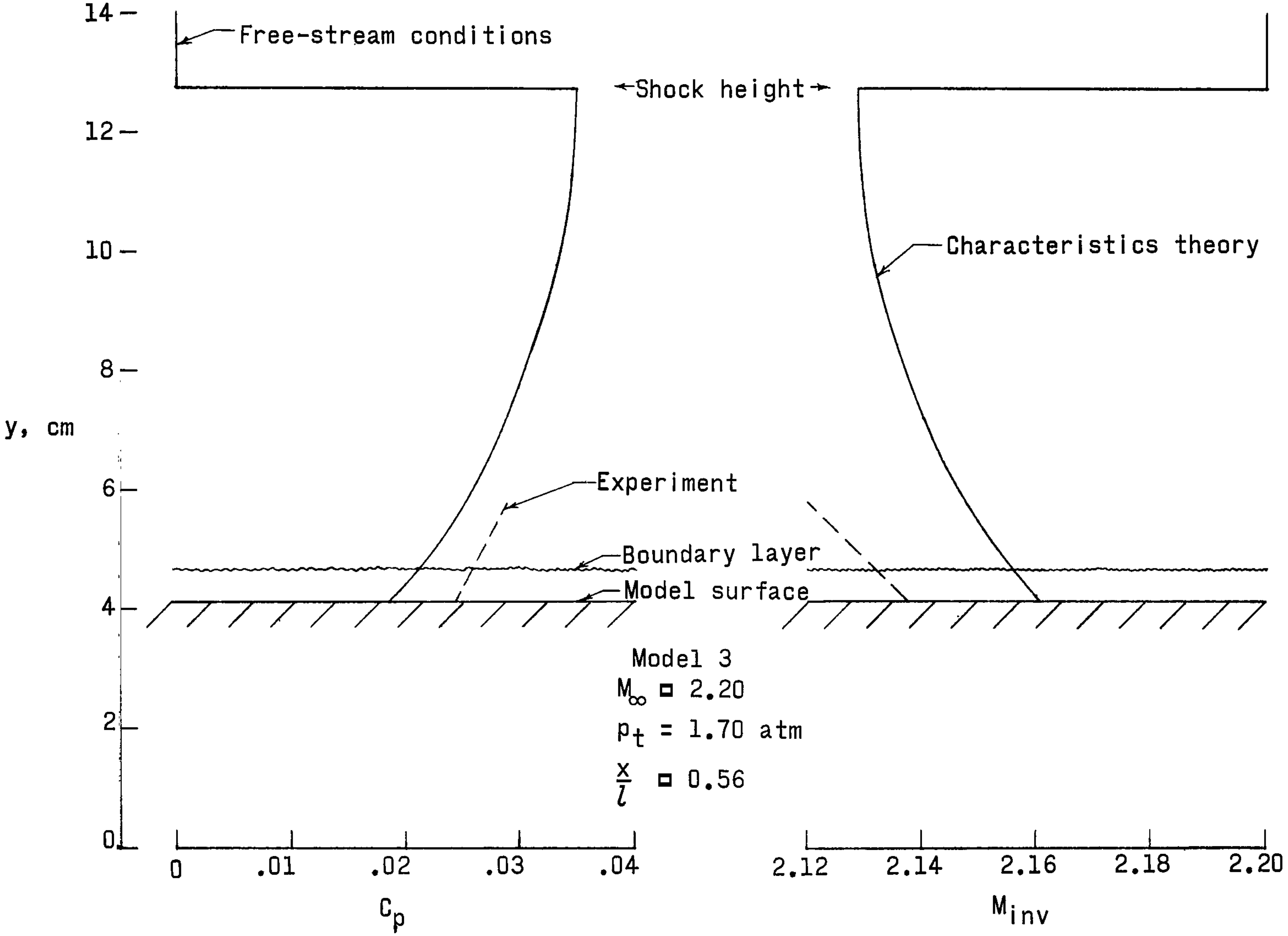

Figure 38.- Typical pressure-coefficient and inviscid Mach number profiles.

> *"The aeronautical and space activities of the United States shall be conducted so as to contribute . . . to the expansion of human knowledge of phenomena in the atmosphere and space. The Administration shall provide for the widest practicable and appropriate dissemination of information concerning its activities and the results thereof."*
>
> —NATIONAL AERONAUTICS AND SPACE ACT OF 1958

NASA SCIENTIFIC AND TECHNICAL PUBLICATIONS

TECHNICAL REPORTS: Scientific and technical information considered important, complete, and a lasting contribution to existing knowledge.

TECHNICAL NOTES: Information less broad in scope but nevertheless of importance as a contribution to existing knowledge.

TECHNICAL MEMORANDUMS: Information receiving limited distribution because of preliminary data, security classification, or other reasons.

CONTRACTOR REPORTS: Scientific and technical information generated under a NASA contract or grant and considered an important contribution to existing knowledge.

TECHNICAL TRANSLATIONS: Information published in a foreign language considered to merit NASA distribution in English.

SPECIAL PUBLICATIONS: Information derived from or of value to NASA activities. Publications include conference proceedings, monographs, data compilations, handbooks, sourcebooks, and special bibliographies.

TECHNOLOGY UTILIZATION PUBLICATIONS: Information on technology used by NASA that may be of particular interest in commercial and other non-aerospace applications. Publications include Tech Briefs, Technology Utilization Reports and Notes, and Technology Surveys.

Details on the availability of these publications may be obtained from:

SCIENTIFIC AND TECHNICAL INFORMATION DIVISION

NATIONAL AERONAUTICS AND SPACE ADMINISTRATION

Washington, D.C. 20546